TUDelft

Delft University of Technology

Breakup and droplet formation of thin liquid jets in prilling applications
A perspective from theory, experiments and numerical simulations

Kamis, Y.E.

DOI

Publication date
2025

Document Version
Final published version

Citation (APA)

Important note
To cite this publication, please use the final published version (if applicable).
Please check the document version above.

BREAKUP AND DROPLET FORMATION OF THIN LIQUID JETS IN PRILLING APPLICATIONS

A PERSPECTIVE FROM THEORY, EXPERIMENTS AND NUMERICAL SIMULATIONS

BREAKUP AND DROPLET FORMATION OF THIN LIQUID JETS IN PRILLING APPLICATIONS

A PERSPECTIVE FROM THEORY, EXPERIMENTS AND NUMERICAL SIMULATIONS

Dissertation

for the purpose of obtaining the degree of doctor
at Delft University of Technology
by the authority of the Rector Magnificus, prof. dr. ir. T.H.J.J. van der Hagen,
chair of the Board for Doctorates
to be defended publicly on
Tuesday 4 February 2025 at 12:30 o'clock

by

Yavuz Emre KAMIS

This dissertation has been approved by the promotors.

Composition of the doctoral committee:

Rector Magnificus,	chairperson
Dr. ir. W.-P. Breugem,	Delft University of Technology, *promotor*
Dr. H. B. Eral,	Delft University of Technology, *promotor*

Independent members:

Prof. dr. ir. B. J. Boersma,	Delft University of Technology,
Prof. dr. D. Bonn,	University of Amsterdam,
Dr. ir. C. W. Visser,	University of Twente,
Dr. T. Gilet,	University of Liège,
Prof. dr. ir. J. T. Padding,	Delft University of Technology, *reserve member*

CONTENTS

SUMMARY

Prilling is a spray solidification process of producing spherical beads, or prills, typically for fertilizers like urea and ammonium nitrate. The process involves molten material passing through perforated rotating containers, forming spiraling jets and breaking up into droplets due to a Rayleigh-Plateau instability by surface tension. These droplets undergo heat exchange with a cooling air stream and turn into solid prills. However, controlling prill size and shape remains challenging due to complex fluid dynamics, thermal effects, and non-Newtonian material properties. This research focuses on understanding jet breakup under the influence of thermal effects and body forces related to gravity and rotation (centrifugal and Coriolis forces). The overarching goal is to optimize the prilling process for a desired narrow prill size distribution by predicting and controlling the jet breakup process. A fundamental and holistic approach was taken based on a combination of experiments, stability analysis and various types of numerical simulations.

The study begins by exploring the dynamics of a spiraling liquid jet emitted from a rotating orifice. Using experiments, linear stability analysis and a nonlinear slender-jet model, the influence of the body forces from rotation and gravity on jet thinning and breakup is quantified. Imposed mechanical vibrations within the nozzle modulate the jet conditions at nozzle exit, enabling control over the jet breakup length and droplet size. The findings reveal that spiraling jets behave similarly to straight jets under gravity, where the body forces influence the thinning rate of the base jet and local base jet conditions control the growth rate of unstable jet perturbations. This insight opens pathways for more precise control mechanisms in various jet-based industrial applications.

In pursuit of alternative control mechanisms, temperature modulation at the nozzle is investigated. Thermal excitation induces flow perturbations within the jet through Marangoni stresses related to the spatial variation in the temperature-dependent surface tension coefficient. The flow perturbations may subsequently also trigger a Rayleigh-Plateau instability through capillary stresses related to the spatial variation in jet curvature. A proposed 'thermal modulation strength number' quantifies the interplay of surface tension gradients and background random noise perturbations that is inherent to every setup. Numerical simulations demonstrate that stronger thermal modulation shortens the jet length and produces more uniform droplets, offering a promising alternative to mechanical vibration methods. This thermal control method presents a significant innovation in that it reduces the reliance on mechanical components, making the process more robust.

In jet breakup studies, it is often assumed that the jet radius at the nozzle exit equals the nozzle radius, but this oversimplifies the dynamics of jets with nonuniform velocity profiles at nozzle exit. Here we consider a long nozzle with a Poiseuille flow profile sufficiently far upstream of the nozzle exit. At nozzle exit, the jet velocity adjusts rapidly

due to inertial, viscous, and capillary stresses, related to the transition from a no-slip condition inside the nozzle to a free-slip condition at the jet/air interface. Using the Computational Fluid Dynamics (CFD) software OpenFOAM, 2D numerical simulations were conducted of the axisymmetric flow within the nozzle and laminar jet outside the nozzle. The simulations were in good agreement with experiments reported in literature. The results show that the viscous stresses near the nozzle exit cause jet expansion at low Reynolds numbers, while conservation of mass and momentum dictates that the jet must contract at high Reynolds numbers. The transition happens at $Re \approx 14.4$, where the Reynolds number is based on nozzle diameter and bulk velocity. For practical applications like prilling, a careful consideration of the upstream flow conditions and nozzle geometry is crucial, as they influence jet contraction, optimal perturbation frequencies, and the resultant droplet size distribution.

To bridge theory and practice, the developed slender-jet model is applied to industrial prilling scenarios with a melt flowing through a perforated container. The shape of the curved meniscus of the melt within the rotating container is estimated using analytical methods which also gives the pressure and velocity distribution along the perforated container wall. Despite simplifying assumptions such as neglecting upstream flow dynamics and inter-jet interactions, the model effectively estimates prill size distributions. Future work should incorporate effects of upstream turbulence, nozzle clogging, jet-airflow and jet-jet aerodynamic interactions for more accurate industrial-scale predictions. Enhancing the fidelity of the model through detailed CFD simulations could improve the prediction accuracy and reliability of the process.

Overall, this thesis advances understanding of jet breakup dynamics in prilling through theoretical, numerical, and experimental approaches. It highlights critical aspects such as the role of rotation, thermal modulation and nozzle design. While significant progress has been made, future research should explore alternative perturbation mechanisms, improve model robustness, and bridge the gap between laboratory experiments and industrial-scale processes. This work lays a foundation for innovative control strategies, enhancing the applicability of prilling to a broader range of materials and industrial processes. Beyond fertilizer production, the findings are applicable to various industries, including pharmaceuticals, inkjet printing, and spray cooling technologies. By refining jet stability and droplet formation mechanisms, these industries can benefit from enhanced precision and efficiency of their processes.

SAMENVATTING

Prillen is een sproei-solidificatieproces voor het produceren van bolvormige kralen, of prills, meestal voor meststoffen zoals ureum en ammoniumnitraat. Het proces omvat gesmolten materiaal dat door geperforeerde roterende containers stroomt, waarbij spiraalvormige stralen ontstaan die uiteenvallen in druppels door een Rayleigh-Plateau-instabiliteit veroorzaakt door oppervlaktespanning. Deze druppels ondergaan warmte-uitwisseling met een koelende luchtstroom en stollen tot vaste prills. Het beheersen van de prillgrootte en -vorm blijft echter een uitdaging vanwege complexe stromingsdynamica, thermische effecten en niet-Newtonse materiaaleigenschappen. Dit onderzoek richt zich op het begrijpen van straalbreuk onder invloed van thermische effecten en krachten gerelateerd aan zwaartekracht en rotatie (centrifugaal- en Corioliskrachten). Het overkoepelende doel is om het prillenproces te optimaliseren voor een gewenste smalle prillgrootteverdeling door het straalbreukproces te voorspellen en te beheersen. Een fundamentele en holistische aanpak werd gevolgd, gebaseerd op een combinatie van experimenten, stabiliteitsanalyse en verschillende soorten numerieke simulaties.

Het onderzoek begint met het verkennen van de dynamica van een spiraalvormige vloeistofstraal die uit een roterende opening wordt uitgespuwd. Door middel van experimenten, lineaire stabiliteitsanalyse en een niet-lineair slanke-straalmodel wordt de invloed van krachten door rotatie en zwaartekracht op het dunner worden en breken van de straal gekwantificeerd. Mechanische trillingen die in de nozzle worden opgewekt, moduleren de straalomstandigheden bij de nozzle-uitgang, waardoor controle over de straalbreuklengte en druppelgrootte mogelijk wordt. De bevindingen tonen aan dat spiraalvormige stralen zich vergelijkbaar gedragen met rechte stralen onder invloed van zwaartekracht, waarbij de krachten de dunnerwordingssnelheid van de basisstraal beïnvloeden en de lokale basisstraalomstandigheden de groeisnelheid van instabiele straalverstoringen beheersen. Dit inzicht opent nieuwe mogelijkheden voor meer precieze controlemechanismen in diverse straalgebaseerde industriële toepassingen.

In de zoektocht naar alternatieve controlemechanismen wordt temperatuurmodulatie bij de nozzle onderzocht. Thermische excitatie veroorzaakt stromingsverstoringen binnen de straal door Marangoni-spanningen, gerelateerd aan de ruimtelijke variatie in de temperatuurafhankelijke oppervlaktespanningscoëfficiënt. De stromingsverstoringen kunnen vervolgens ook een Rayleigh-Plateau-instabiliteit veroorzaken via capillaire spanningen, gerelateerd aan de ruimtelijke variatie in de straalcurvatuur. Een voorgesteld 'thermisch modulatie-sterktenummer' kwantificeert de wisselwerking tussen oppervlaktespanningsgradiënten en achtergrondruisverstoringen die inherent zijn aan elke opstelling. Numerieke simulaties tonen aan dat sterkere thermische modulatie de straallengte verkort en meer uniforme druppels produceert, wat een veelbelovend alternatief biedt voor mechanische trillingsmethoden. Deze thermische controlemethode vormt een belangrijke innovatie doordat ze de afhankelijkheid van mechanische componen-

ten vermindert, waardoor het proces robuuster wordt.

In studies over straalbreuk wordt vaak aangenomen dat de straalradius bij de nozzle-uitgang gelijk is aan de mondradius, maar dit vereenvoudigt de dynamica van stralen met niet-uniforme snelheidsprofielen bij de nozzle-uitgang. Hier beschouwen we een lange nozzle met een Poiseuille-stroomprofiel ver stroomopwaarts van de nozzle-uitgang. Bij de nozzle-uitgang past de straalsnelheid zich snel aan door traagheids-, viskeuze en capillaire spanningen, gerelateerd aan de overgang van een no-slip-conditie binnen de nozzle naar een free-slip-conditie aan het straal/lucht-grensvlak. Met behulp van de Computational Fluid Dynamics (CFD)-software OpenFOAM werden 2D-numerieke simulaties uitgevoerd van de as-symmetrische stroming binnen de nozzle en de laminaire straal buiten de nozzle. De simulaties kwamen goed overeen met experimenten die in de literatuur worden gerapporteerd. De resultaten tonen aan dat viskeuze spanningen nabij de nozzle-uitgang straaluitzetting veroorzaken bij lage Reynolds-getallen, terwijl behoud van massa en momentum dicteert dat de straal moet samentrekken bij hoge Reynolds-getallen. De overgang gebeurt bij $Re \approx 14,4$, waarbij het Reynolds-getal is gebaseerd op de monddiameter en de bulksnelheid. Voor praktische toepassingen zoals prillen is een zorgvuldige beschouwing van de stroomomstandigheden stroomopwaarts en de nozzle-geometrie cruciaal, omdat deze invloed hebben op straalcontractie, optimale verstoringsfrequenties en de resulterende druppelgrootteverdeling.

Om theorie en praktijk te overbruggen wordt het ontwikkelde slanke-straalmodel toegepast op industriële prillscenario's waarbij een smelt door een geperforeerde container stroomt. De vorm van de gekromde meniscus van de smelt binnen de roterende container wordt geschat met analytische methoden, die ook de druk- en snelheidsverdeling langs de geperforeerde containerwand geven. Ondanks vereenvoudigde aannames zoals het negeren van stroomopwaartse stromingsdynamica en interacties tussen stralen, schat het model effectief de prillgrootteverdeling in. Toekomstig werk moet de effecten van stroomopwaartse turbulentie, verstopping van de nozzle en aerodynamische interacties tussen straal-lucht en straal-straal integreren voor nauwkeurigere voorspellingen op industriële schaal. Het verbeteren van de nauwkeurigheid van het model door gedetailleerde CFD-simulaties kan de voorspellingsbetrouwbaarheid van het proces vergroten.

Al met al bevordert dit proefschrift het begrip van straalbreukdynamica bij het prillen door middel van theoretische, numerieke en experimentele benaderingen. Het benadrukt kritieke aspecten zoals de rol van rotatie, thermische modulatie en nozzle-ontwerp. Hoewel aanzienlijke vooruitgang is geboekt, zou toekomstig onderzoek alternatieve verstoringsmechanismen moeten verkennen, de modelrobuustheid moeten verbeteren en de kloof tussen laboratoriumexperimenten en industriële processen moeten overbruggen. Dit werk legt een basis voor innovatieve controlemechanismen, die de toepasbaarheid van prillen op een breder scala aan materialen en industriële processen verbeteren. Naast de productie van meststoffen zijn de bevindingen toepasbaar in diverse industrieën, waaronder de farmaceutische industrie, inkjetprinten en sproeikoelingstechnologieën. Door de stabiliteit van de straal en de druppelvormingsmechanismen te verfijnen, kunnen deze industrieën profiteren van verbeterde precisie en efficiëntie in hun processen.

1

INTRODUCTION

1.1. BACKGROUND

The United Nations predicts that the global population will increase to 9.7 billion by 2050 [1]. As the population grows, economic conditions are expected to improve as more people move to cities, leading to job creation. The population growth, however, is putting pressure on the limited natural resources, such as land and water, due to rapid urbanization and the growing demand for food. According to the Food and Agriculture Organization (FAO) of the United Nations, approximately 821 million people, or one out of every nine people globally, are undernourished [2].

One facet that is at the core of this problem is the production and usage of fertilizers. The use of fertilizers has become essential in agriculture as the nutrient capacity of soil decreases after each harvest. Fertilizers contain nutrients that are necessary for plant growth and are applied to the soil or the tissues of plants. The market for fertilizers is growing globally due to the increasing demand for food and the decreasing amount of arable land. This reduction in arable land is largely due to rapid urbanization and industrialization, which have also affected the quality and quantity of natural resources such as land, air, and water [3].

Sustainable farming practices are becoming increasingly popular, which is driving the growth of the fertilizer market in recent years. The use of synthetic fertilizers, which are derived from fossil fuels, has led to increased agricultural production on limited arable land worldwide. However, their adverse effects on soil productivity and environmental quality have led to a search for alternatives such as organic fertilizers [4].

The research for alternative fertilizers also require the methods of fertilizer production to be robust for producing high volumes of fertilizers irrespective of their composition. Conventionally, the most common method to produce standard fertilizers (e.g. urea and ammonium nitrate) is prilling. So it is important to understand the physics involved within the process to be able to better control the yield and optimize the design process to accommodate a variety of materials. In the following subsection, the process of prilling will be introduced and the underlying multiphysics problem will be formulated.

1.2. PRILLING

Prilling is a spray solidification process that is used for shaping large amounts of bulk solids into spherical beads of around a millimeter in diameter, or so-called "prills". It is done by bringing the material to a molten state, showering it through static or rotary shower heads and cooling the formed droplets back into solid state. Originally used for the production of lead shot [5], prilling today is mostly used for producing urea and ammonium nitrate fertilizers.

Fig. 1.1(*a*) highlights the different stages of the process. The melt is sprayed down through the "prilling tower", a tower in which heat-exchange occurs between air and molten droplets in order to rapidly cool the droplets and form the prills. Fig 1.1(*b*) shows a typical end-product of the prilling process – in this case NaOH prills.

The challenge of the prilling process is to have a uniform distribution of size and shape within the end-product. In fluid mechanics principles, the size of a droplet
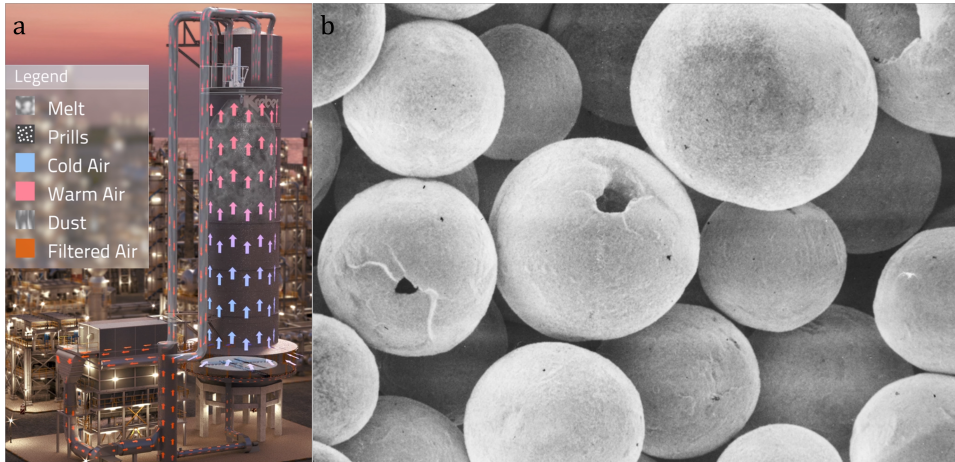
Figure 1.1: (a) Illustration of the prilling process. (b) NaOH prills 0.5-1.2mm [5].

is largely dictated by the hole size through which it is generated whereas the shape is expected to be spherical due to the minimization of free surface energy favoring the lowest area-to-volume ratio. In reality, however, the prilling process is much more complex and difficult to control, so the distribution of the size and shape is not adequately uniform; there may be large non-spherical prills due to poor cooling efficiency, or very small droplets that form "dust", which have to be filtered to prevent air pollution and dust explosion. Another major challenge in the prilling process is the applicability to a larger variety of materials. While some knowledge is developed for materials like urea and ammonium nitrate and the process is well-controlled, the principles of the process are not robust enough to apply to new materials.

To overcome these challenges, it is essential to obtain an in-depth understanding of the prilling process as a multiphysics problem. Fig. 1.2 shows which properties are important at which stage of the process. These material and operational properties will determine the timescale of physical events, such as droplet formation and heat/mass transfer. It is key to understand the interplay of these timescales and grouping these parameters into non-dimensional parameters so that the applicability of prilling is extended to a larger set of materials while retaining the control over the size and shape distribution.

In light of this introduction, we can formulate the underlying physical problem as a study of jet breakup and droplet formation in the presence of:

- Thermal effects such as temperature-dependent viscosity, surface tension;

- Non-straight trajectory due to forces from non-inertial frame of reference (e.g. centrifugal, Coriolis);

- Non-Newtonian effects.

After the droplets are formed, the physical problem can be formulated as the

1
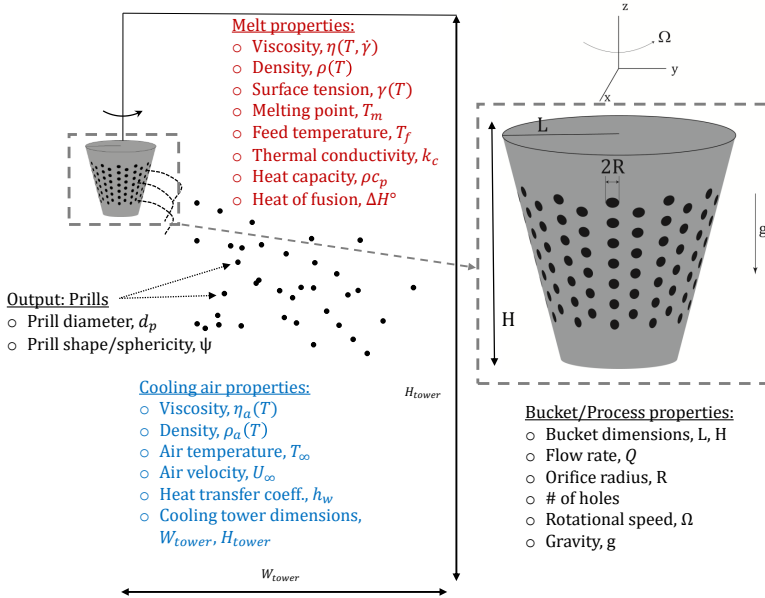
Figure 1.2: A schematic of the prilling process. The input parameters are categorized as the material (melt) properties, cooling air properties and parameters related to the operation, e.g., bucket geometry.

crystallization of a droplet that falls through a cooling medium (e.g., air) and loses heat by means of forced convection and generates heat during crystallization.

1.2.1. CONTROLLING THE FORMATION OF DROPLETS

Controlling droplet formation from liquid jets presents a critical challenge relevant to numerous applications across different scales. These range from serial femtosecond X-ray crystallography [6, 7], where jet lengths are typically measured in microns, to pharmaceutical production [8, 9], where lengths reach several millimeters, and to prilling [5], where jets can extend up to tens of centimeters. A controlled and predictable breakup process, however, is critical to all of these processes regardless of their scale. In the absence proper modulation, achieved by applying small-amplitude perturbations at specific frequencies, the resulting droplets are irregular and exhibit a broad size range. Among these applications, prilling stands out as particularly complex and less extensively studied.

1.2.2. FUNDAMENTALS OF JET BREAKUP: RAYLEIGH-PLATEAU INSTABILITY

The study of all processes involving jet breakup starts from the well-known Rayleigh-Plateau instability, which manifests itself as a competition of radii of curvatures on a cylindrical column of liquid.

It stems from the earlier works of Young and Laplace, who underline the existence of two radii of curvature in a column of liquid and its effect on the pressure inside the liquid:

$$\Delta p = \gamma \left(\frac{1}{R_1} + \frac{1}{R_2} \right) \qquad (1.1)$$

where γ is the surface tension coefficient in $\mathrm{N\,m^{-1}}$. Eqn. (1.1) formulates the pressure jump due to surface tension in between two mediums across the interface.

Fig. 1.3 indicates the two contributions to the curvature. The first contribution comes from the local radius of the jet, namely R_1 in Fig 1.3. If you consider a cylindrical column of liquid with radius R_0, the pressure difference across the interface would be $\Delta p = \gamma / R_0$ per Eqn. (1.1). When there are axisymmetric sinusoidal perturbations present, the contribution to the curvature from the local radius will be lower in the crest regions (i.e. lower pressure) and will be higher in the trough regions (i.e. higher

Figure 1.3: The perturbations affect the *mean* curvature which has two contributions

pressure). The second contribution arises from the shape of the sinusoidal disturbances on the jet radius along the axial direction, namely R_2 in Fig. 1.3. This contribution is negative in the trough regions and positive in the crest regions. The interplay of the 2 contributions depends on the wavelength of the perturbations; at some wavelengths, the 2 contributions exactly cancel each other and the jet is stabilized, where other wavelengths lead to instability and subsequent breakup. In what follows, we provide the analytical approach that determines which wavelengths would be unstable.

Plateau analyzed the problem from the energy point of view that a jet is unstable to any perturbation that reduces the surface area, thus postulating the role of surface tension in the instability [10]. Rayleigh extended this by conducting stability analysis on the linearized Euler equations [11], which start with equations of motion for an

incompressible fluid in a frame of reference moving with the jet speed, U_0:

$$\nabla \cdot \mathbf{v} = 0 \tag{1.2a}$$

$$\rho \left(\frac{\partial \mathbf{v}}{\partial t} + (\mathbf{v} \cdot \nabla) \mathbf{v} \right) = \nabla \cdot \sigma + \mathbf{f} \tag{1.2b}$$

where σ is the viscous stress tensor and $\mathbf{f}$ is a general body force acting on the fluid. In the simple case of a fluid with negligible viscosity and no body force, we have $\sigma = -p\mathbf{I}$ and $\mathbf{f} = 0$. So the combination of (1.2a) and (1.2b) will give $\nabla^2 p = 0$. The pressure is perturbed as $\delta p = \epsilon_0 e^{-i\omega t} F(r) cos(kz)$, where ϵ_0 is the initial, infinitesimally small perturbation amplitude, $F(r)$ is a non-dimensional function of the radial position r within the jet, ω is the complex frequency, and k is the wavenumber of the perturbation.

In the temporal stability analysis, by definition, where ω_r is the angular frequency and ω_i represents the exponential growth rate of the perturbation. From the linearized Euler equations, the following equation can be derived for $F(r)$:

$$\frac{\partial^2 F}{\partial r^2} + \frac{1}{r} \frac{\partial F}{\partial r} - k^2 F = 0$$

The solution is the zeroth order Kelvin function of the first kind $F(r) = I_0(kr)$ [12] which is bounded at $r = 0$. Using the Laplace pressure and the kinematic condition one arrives at the so called dispersion relation for ω^2 [11].

$$\omega^2 = -\frac{\gamma}{\rho R_0^3} (kR_0) \left[1 - (kR_0)^2 \right] \frac{I_1(kR_0)}{I_0(kR_0)} \tag{1.3}$$

where R_0 is the undisturbed jet radius. A perturbation is unstable when $\omega_i > 0$, i.e., when the right-hand side of Eq. 1.3 is negative. The dispersion relation thus indicates the existence of a cutoff wavelength for instability, that is, $\lambda > 2\pi R_0$ for a perturbation to be unstable. Indeed the fastest growing wavelength is about 9 times the initial radius of the jet. The characteristic timescale of the growth is also revealed in (1.3), that is the inertio-capillary timescale $t_c = \sqrt{\rho R_0^3/\gamma}$. This analysis has later been extended by Rayleigh to include the effect of an ambient inviscid fluid [13].

Early experiments agreed quite well with the linear stability analysis [14, 15]. The results verify the cutoff and fastest growing wavelengths, as shown in Fig. 1.4.

Lafrance included higher order terms in the perturbation analysis to estimate the formation of satellite droplets and found good agreement between theoretical analysis and experiments [16]. Chaudhary et al. consider the effect of the perturbation amplitude and correlate this to the break up time [17].

The influence of viscosity has also been analysed by Rayleigh in [13] for the case of Stokes flow. The dispersion relation takes then the form:

$$-i\omega = \frac{\gamma}{2R_0\eta} \frac{1 - (kR_0)^2}{1 + (kR_0)^2 \left[1 - (I_0(kR_0)/I_1(kR_0))^2 \right]} \tag{1.4}$$

Equation (1.4) also reveals the viscocapillary timescale $t_v = \eta R_0/\gamma$. The linear stability analysis is unified for viscous jet with finite inertia by Chandrasekhar in
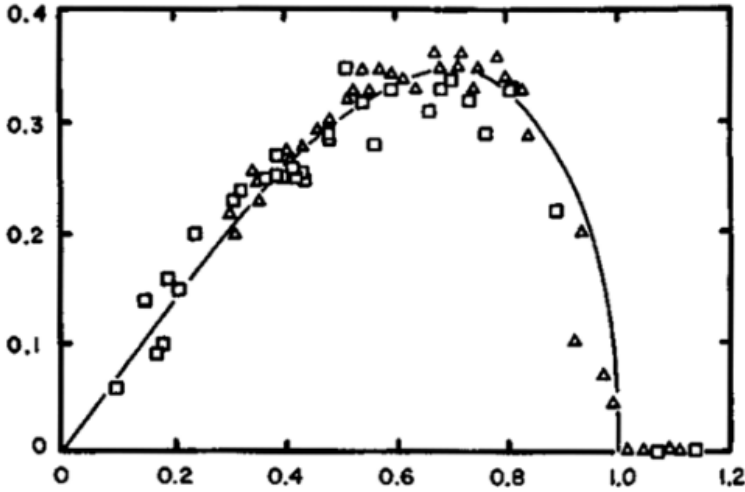
Figure 1.4: The solid line is the dispersion relation given in (1.3), the dimensionless growth rate $\omega_i/\sqrt{\rho R_0^3/\gamma}$ as a function of the dimensionless wavenumber kR_0 and the scattered data are from [14] and [15]

[18]. Viscosity slows down the growth of unstable waves and the fastest growth occurs at longer wavelengths with increasing viscosity.

At this point, it is interesting to re-consider the timescales involved in the case of a Newtonian liquid jet. As revealed in (1.3) and (1.4), one has the inertio-capillary and visco-capillary timescales given as

$$t_c = \sqrt{\frac{\rho R_0^3}{\gamma}} \qquad t_v = \frac{\eta R_0}{\gamma} \qquad (1.5)$$

respectively. In addition, one of course has the advective timescale in the case of a momentum driven jet $t_a = R_0/U_0$ where U_0 is the unperturbed jet speed. The comparison of these timescales give rise to several non-dimensional numbers and a regime map related to this. The ratio of the inertio-capillary timescale to the advective time gives the Weber number, which can also be interpreted as a characteristic ratio of dynamic pressure versus Laplace pressure variations during breakup.

$$We = \frac{t_c^2}{t_a^2} = \frac{\rho U^2 R_0}{\gamma} \qquad (1.6)$$

The effect of viscosity on capillary jet breakup is measured with the Ohnesorge number:

$$Oh = \frac{t_v}{t_c} = \frac{\eta}{\sqrt{\rho R_0 \gamma}} = \frac{\sqrt{We}}{Re} \qquad (1.7)$$

1

where $Re = \rho U_0 R_0 / \eta$ is the jet Reynolds number. In the case where gravitational stretching of a (vertical) jet is significant, one has another timescale involved, $t_g = \sqrt{R_0/g}$. The Bond number is the nondimensional number that measures the square of ratio of the inertio-capillary timescale to this inertio-gravitational timescale which can also be interpreted as the characteristic ratio of hydrostatic pressure to Laplace pressure variations during breakup:

$$Bo = \frac{\rho g R_0}{\gamma / R_0} = \frac{We}{Fr^2} \tag{1.8}$$

where $Fr = U_0 / \sqrt{gR_0}$ is the jet Froude number.

1.3. OBJECTIVES AND SCOPE OF THE RESEARCH

There has been some empirical know-how on the production of urea and ammonium nitrate fertilizers, which are the most common ones. But the systems are not robust enough when the fertilizers are enhanced with some polymers and/or minerals. So a physical understanding of jet breakup of complex fluids needs to be obtained in order to design systems that can accommodate different materials. **The overarching objective of this research** is to identify the dimensionless numbers that would describe the different physics within the process and investigate the different regimes with respect to these dimensionless numbers, with a focus on predicting and controlling the jet formation and breakup in the presence of thermal effects and rotation. This would allow scalability and better control of the formation of droplets/prills with the desired size in a prilling process.

In this Ph.D. study, the following **research questions** have been addressed:

1. **What physical mechanism dictates the breakup of a jet and formation of drops in the presence of jet rotation (i.e., a spiralling jet)? How can the breakup of spiralling jets be modelled? What is the effect of the frequency and amplitude of mechanical excitation of the jet on breakup? How can the size distribution of the drops be controlled?**

2. **Can thermal excitation be used to force breakup of a straight jet? What is the effect of the frequency and amplitude of thermal excitation of the jet on breakup?**

    As mentioned earlier, the size of the formed drops strongly depends on the initial (unperturbed) jet radius. This might not be equal to the nozzle radius from which the jet is emitted. Dependent on the geometry and flow conditions inside the nozzle, the jet may undergo a slight and rapid contraction over a distance comparable to the nozzle radius, related to a change from a no-slip wall condition inside the nozzle to a virtually free-slip condition at the jet/air interface outside the nozzle [19]. Our third research question is therefore:

3. **What physical mechanism is responsible for rapid jet contraction of a jet at nozzle exit? More specifically, what is the influence of viscous and capillary (surface tension) effects on jet contraction and on the transition from jet**

1

expansion at low jet Reynolds number to jet contraction at higher Reynolds numbers?

In industrial prilling processes, typically a tapered and perforated prilling bucket is used with a continuous feed of the melt towards the rotating bucket and jets emitted from the bucket from thousands of holes. This leads to the fourth and final research question:

4. **How can the results obtained for a single spiralling jet be used to predict the prill size distribution in an industrial prilling process?**

To address these questions, a combined theoretical, numerical and experimental approach has been undertaken. An in-house numerical model based on slender jet approximation [20] has been developed. This approximation is based on the disparity of the longitudinal and transverse length scales of the jets encountered typically in the prilling process. In addition, a lab setup has been designed and assembled to investigate the evolution of instabilities and formation of droplets from a spiralling jet. Using the findings from numerical and experimental approaches, a linear stability analysis has been conducted to understand the linear response of spiralling jets to disturbances at different frequencies.

1.4. OUTLINE OF THE THESIS

The thesis is organized as follows. In Chapter 2, we address research question 1 and investigate the effects of non-straight trajectory on jet breakup. A lab scale experimental setup has been built to form a jet emanating from a rotating orifice and high-speed images have been obtained to analyze the capillary waves on the jet. Also, an in-house numerical framework has been developed where the slender jet approximation is used and the results are compared against the images from the experiments. In Chapter 3, the research question 2 is addressed and the slender jet model is extended with energy balance and thermal effects on the jet instabilities are investigated. Also the concept of thermal modulation to control breakup is tested and discussed. In Chapter 4, the research question 3 is addressed and the contraction or expansion of Newtonian jets issued from round orifices is numerically analyzed and discussed. In Chapter 5, research question 4 is addressed, and framework is presented to use our findings for a single spiralling jet to predict the prill size distribution in an industrial prilling process.Finally in Chapter 6, the research questions are revisited with main conclusions and future research recommendations.

REFERENCES

[1] United Nations (2024). *World Population Prospects 2024: Summary of Results*. Tech. rep. https://population.un.org/wpp/Publications/Files/WPP2024_Summary_of_Results.pdf. New York: United Nations: UN/DESA/POP/TR/NO. 9., 2024.

[2] Knowledge Sourcing Intelligence LLP. *Worldwide Fertilizer Industry to 2025 - Key Drivers and Restraints*. https://www.prnewswire.com/news-releases/worldwide-fertilizer-industry-to-2025---key-drivers-and-restraints-301165654.html. 2020.

[3] Foreign Agricultural Service. *Impacts and Repercussions of Price Increases on the Global Fertilizer Market*. Tech. rep. U.S. Department of Agriculture, 2022.

[4] S. Tripathi, P. Srivastava, R. S. Devi, and R. Bhadouria. "Chapter 2 - Influence of synthetic fertilizers and pesticides on soil health and soil microbiology". In: *Agrochemicals Detection, Treatment and Remediation*. Ed. by M. N. V. Prasad. Butterworth-Heinemann, 2020, pp. 25–54. ISBN: 978-0-08-103017-2. DOI: https://doi.org/10.1016/B978-0-08-103017-2.00002-7.

[5] C. M. Van't Land. *Industrial Crystallization of Melts*. CRC Press, 2004.

[6] H. N. Chapman, P. Fromme, A. Barty, T. A. White, R. A. Kirian, A. Aquila, M. S. Hunter, J. Schulz, D. P. DePonte, U. Weierstall, *et al.* "Femtosecond X-ray protein nanocrystallography". In: *Nature* 470.7332 (2011), pp. 73–77.

[7] M. O. Wiedorn, S. Awel, A. J. Morgan, K. Ayyer, Y. Gevorkov, H. Fleckenstein, N. Roth, L. Adriano, R. Bean, K. R. Beyerlein, *et al.* "Rapid sample delivery for megahertz serial crystallography at X-ray FELs". In: *IUCrJ* 5.5 (2018), pp. 574–584.

[8] H. B. Eral, M. O'Mahony, R. Shaw, B. L. Trout, A. S. Myerson, and P. S. Doyle. "Composite hydrogels laden with crystalline active pharmaceutical ingredients of controlled size and loading". In: *Chemistry of Materials* 26.21 (2014), pp. 6213–6220.

[9] H. B. Eral, E. R. Safai, B. Keshavarz, J. J. Kim, J. Lee, and P. S. Doyle. "Governing principles of alginate microparticle synthesis with centrifugal forces". In: *Langmuir* 32.28 (2016), pp. 7198–7209.

[10] J. Plateau. *Statique expérimentale et théorique des liquides soumis aux seules forces moléculaires*. Vol. 2. Gauthier-Villars, 1873.

[11] L. Rayleigh. "On the capillary phenomena of jets". In: *Proc. R. Soc. London* 29.196-199 (1879), pp. 71–97.

1

[12] M. Abramowitz and I. Stegun. "Handbook of Mathematical Functions". In: 9th ed. Dover, 1970, p. 3.3.7.

[13] L. Rayleigh. "On the instability of cylinder fluid surfaces". In: *Philos. Mag* 34 (1892), pp. 145–54.

[14] R. J. Donnelly and W. Glaberson. "Experiments on the capillary instability of a liquid jet". In: *Proceedings of the Royal Society of London. Series A. Mathematical and Physical Sciences* 290.1423 (1966), pp. 547–556.

[15] E. Goedde and M. Yuen. "Experiments on liquid jet instability". In: *Journal of Fluid Mechanics* 40.3 (1970), pp. 495–511.

[16] P. Lafrance. "Nonlinear breakup of a laminar liquid jet". In: *The Physics of Fluids* 18.4 (1975), pp. 428–432.

[17] K. Chaudhary and T. Maxworthy. "The nonlinear capillary instability of a liquid jet. Part 2. Experiments on jet behaviour before droplet formation". In: *Journal of fluid mechanics* 96.2 (1980), pp. 275–286.

[18] S. Chandrasekhar. *Hydrodynamic and hydromagnetic stability*. Courier Corporation, 2013.

[19] J. Batchelor, J. Berry, and F. Horsfall. "Die swell in elastic and viscous fluids". In: *Polymer* 14.7 (1973), pp. 297–299.

[20] J. Eggers and T. F. Dupont. "Drop formation in a one-dimensional approximation of the Navier–Stokes equation". In: *Journal of Fluid Mechanics* 262 (1994), pp. 205–221.

2

CONTROLLING THE BREAKUP OF SPIRALLING JETS: RESULTS FROM EXPERIMENTS, NONLINEAR SIMULATIONS AND LINEAR STABILITY ANALYSIS

In this chapter, we experimentally and numerically study the dynamics of a liquid jet issued from a rotating orifice, whose breakup is regulated by a vibrating piezo element. The helical trajectory of the spiralling jet yields fictitious forces varying along the jet whose longitudinal projections stretch and thin the jet, affecting the growth of perturbations. We show that by quantifying these fictitious forces, one can estimate the jet intact length and size distribution of drops formed at jet breakup. The presence of the locally varying fictitious forces may render high-frequency perturbations, that would otherwise be stable in the abscence of stretching, unstable, as observed similarly in the case of straight jets stretching under gravity. The perturbation amplitude then dictates how strong the perturbation is coupled to the jet compared with random noise that is inherently present in any experimental set-up. In the present study we exploit the slenderness of the jet to separate the calculation of the base flow and the growth of perturbations. The fictitious forces calculated from the base flow trajectory are then used in a nonlinear slender-jet model, which treats the spiralling jet as a quasi-straight jet with locally varying body forces. We show both experimentally and numerically that jet breakup characteristics (e.g. intact

---

length and drop size distribution) can be controlled by finite-amplitude perturbations created by mechanically induced pressure modulations. Finally, we revisit the integrated net gain approach developed for straight jets under gravity and we provide simple analogous relations for spiralling jets.

2

2.1. INTRODUCTION

Liquid jets with non-straight trajectories appear in many industrial applications, including fibre spinning [2], centrifugal hydrogel synthesis [3] and homogenization [4], spinning disc atomization [5, 6] and prilling [7, 8]. In spinning disc atomization and prilling, the product yields are the droplets/prills formed under inertio-capillary breakup of a spiralling jet, mainly due to a Rayleigh-Plateau instability. To better control the breakup and drop formation process of a spiralling jet, one needs a thorough understanding of the jet flow along a helical trajectory, i.e., how an instability evolves downstream and leads to breakup, as well as experimental validation of the proposed theories and results. The rotating nature of the spiralling jet makes it rather challanging to design setups where the experimental conditions are precisely controlled. Wong et al. studied spiralling jets experimentally, where the jet was issued from an orifice on a rotating bucket that is drained by hydrostatic pressure due to gravity and rotation [9]. They discuss the combined effect of gravity and rotation on the exit velocity and provided observations on the breakup modes corresponding to different nondimensional numbers. In a follow-up study, Partridge et al. studied spiralling jets on a bigger setup and highlighted that for a larger setup it is harder to predict the breakup characteristics as mechanical vibrations and air resistance play a much bigger role [10]. In addition to experimental approaches, analytical models were also developed. Wallwork et al. studied spiralling jets extensively in the inviscid limit, providing temporal and spatial linear stability analyses along with it [11]. This was later extended to include viscous effects [12–14], non-Newtonian fluid behaviour [15, 16] and Marangoni effects from surfactants [17]. In an extensive mathematical study, Shikhmurzaev & Sisoev pointed out how *a priori* assumptions in the definition of the jet specific coordinate frame lead to an erroneous derivation of the base jet trajectory equations and they laid out a curvilinear local coordinate framework without any assumptions [18]. This approach was later applied by Li, Sisoev & Shikhmurzaev [19] and Noroozi et al. [20] to study the trajectory and the base flow of a spiralling jet.

Comparison of the predictions from linear stability analyses with experiments revealed their lack of ability to predict the jet behaviour at later stages of instability and the subsequent drop formation, stressing the necessity of a nonlinear modeling approach. However, full 3D simulations of the breakup of a spiralling jet would be computationally very expensive and is not feasible yet. Li et al. [19] have used an arbitrary Lagrangian-Eulerian based "end-code" where the prescribed base flow trajectory (and thus the locally varying body forces in a curvilinear system describing the jet) are used to simulate the nonlinear stages of the growth of perturbations. By exploiting the typically slender nature of the spiralling jets, the nonlinear growth can be accurately simulated with a 1D slender jet model [21] in which the spiralling jet is basically treated as a quasi-straight jet with locally varying body forces. The strength of the slender jet approach has been showcased in several studies on nozzle driven jets; Driessen et al. showed droplet regime control using multimode perturbations [22] and McIlroy & Harlen studied the effects of finite perturbation amplitude on breakup characteristics [23]. The method proved useful also in nonisothermal cases with the additional presence of thermo-capillary (Marangoni) effects [24, 25].

The case of a spiralling jet bears many analogies to a straight jets under a non-negligible gravity force, since the fictitious forces that dictate the trajectory of the jet have finite lon-

gitudinal projections that stretch the jet along the flow direction. It is well-known that the Rayleigh-Plateau instability is significantly altered by the presence of stretching [26]. In the context of gravity driven jets, the regimes are studied in both the viscous [27, 28] and the inviscid limit [29]. On the one hand, stretching tends to damp the perturbations when the timescale related to stretching is much faster than that of the inertio-capillary growth [30]. On the other hand, stretching tends also to enhance perturbations through thinning of the jet and the associated reduction of the inertio-capillary time scale along the jet.

Previous studies on the effect of stretching in gravity-driven and spiralling jets have mainly been on the linear stability analyses under infinitesimally small perturbations. A full overview on the process from initial perturbation till jet breakup and beyond, including further breakup or coalescence of detached drops, is missing. Here we present results from a comprehensive study on the breakup of spiralling jets based on experiments, non-linear slender-jet simulations, and linear stability analysis. Our prime interest is in accurate estimation of the breakup of a spiralling jet and resultant drop size distribution and to provide physical insights for practical applications of this complex problem.

In §2.2 we provide details on the experimental setup used. In §2.3 we present the non-linear slender-jet model, including details of the underlying mathematical framework and a derivation of the base flow equations. Results for the jet breakup from the experiments and the slender-jet model are discussed in §2.4. In the next section, we demonstrate the analogy between a spiralling jet in the presence of fictitious forces and a straight jet subject to gravity. This is used then in a linear stability analysis with an integrated gain approach [28, 29]. Furthermore, in analogy with a gravity-driven straight jet, we show the existence of similarity solutions. Finally, in §2.6 we draw the main conclusions.

2.2. EXPERIMENTAL SETUP

The CAD model and the schematic of the experimental setup are shown in figure 2.1. A fluid reservoir with a nearly constant pressure head delivers the fluid to the rotating nozzle via an intermediate chamber. A rotary swivel joint is used to connect the stationary fluid chamber to the rotating nozzle. The swivel joint is spun with a stepper motor through a timing belt at the desired speed. A circular plate connected to the piezo-actuator is embedded in the fluid chamber for a well controlled periodic perturbation of the nozzle exit velocity at a desired frequency. The jet is visualised with the help of a high-speed camera that is fixed in the lab frame of reference. The camera records at a frequency of 2500 frames per second to capture consecutive breakup events. The pixel size of the sensor is $11 \times 11 \ \mu m^2$ and the scale factor was found to be of 53 μm/px which corresponds to a magnification of 0.207. The exposure time of the camera is set to 75 μs which limits the blurring of the jet to around 1.6 px. Since the Rossby number is close to unity, the blurring due to streamwise motion and the rotation of the jet is similar. Completely eliminating blurring was not possible so a compromise was made between blurring and good contrast. The jet is illuminated from the back by a LED panel. The velocity of the jet is determined at an estimated accuracy of 2% from the drop in liquid

Experimental parameters	
Rotating arm, L	7.48 cm
Nozzle radius, R_0	400 µm
Nozzle exit velocity, U_0	1.85±0.2 m s^{-1}
Rotational speed, Ω	250 rpm (26.2 rad s^{-1})
Density, ρ	997 kg m^{-3}
Dynamic viscosity, η	0.9 mPa s
Surface tension, γ	72 mN m^{-1}
Piezoplate frequency	520-740 Hz
Piezoplate supply voltage	75-150 V
Piezoplate displacement	4.5-9 µm
Nondimensional parameters used in the simulations	
Jet slenderness, $\epsilon = R_0/L$	5.4×10^{-3}
Weber, $We = \rho U_0^2 R_0 / \gamma$	18.3
Ohnesorge, $Oh = \eta / \sqrt{\rho R_0 \gamma}$	6×10^{-3}
Reynolds, $Re = \rho U_0 L / \eta$	1.5×10^5
Rossby, $Rb = U_0 / (\Omega L)$	0.94
Froude, $Fr = U_0 / \sqrt{gL}$	2.13

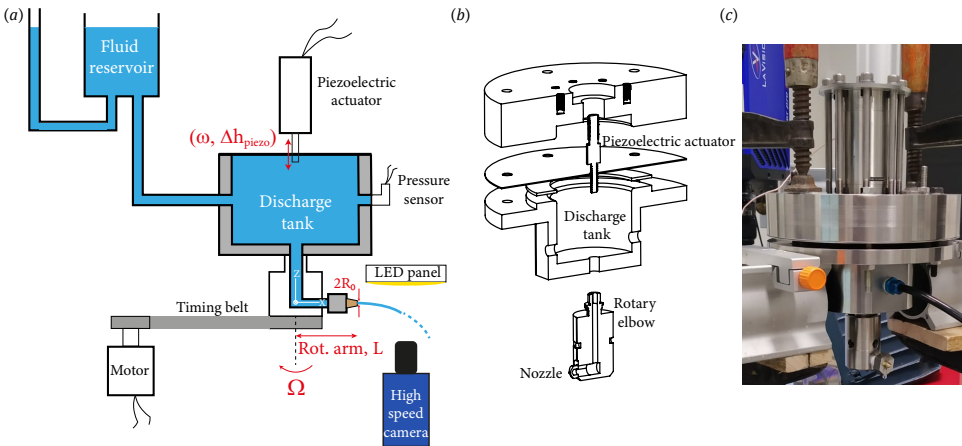Table 2.1: Experimental parameters and corresponding nondimensional numbers used in the simulations.

Figure 2.1: Experimental setup. (*a*) Schematic of the setup. (*b*) CAD drawing of the piezo actuator & plate, fluid discharge tank and the rotary elbow. (*c*) Photo of the parts given in (*b*).

level of the fluid reservoir. Properties of the working fluid are given in table 2.1.

2.3. COMPUTATIONAL MODEL

We performed a numerical study of the same flow geometry as considered in the experiments. The flow within the jet is decomposed into a stationary base state and perturbations that are imposed at the nozzle and evolve downstream along the jet. The jet trajectory and base flow are coupled with each other and hence must be solved simultaneously. Using the knowledge of the trajectory and on how the jet velocity evolves downstream, we can then consider the perturbations on the jet. In what follows, we first present the mathematical framework in which we derive the governing equations in a moving frame of reference and using curvilinear coordinates. Assuming a slender jet, we then derive the equations for the base flow and compute from this the fictitious forces acting on the flow along the jet trajectory. Finally, we derive the slender-jet model for the flow perturbations.

2.3.1. MATHEMATICAL FRAMEWORK

In a frame of reference co-rotating with the nozzle at an angular velocity $\Omega = (0,0,-\Omega)$, the non-dimensional Navier-Stokes equations for the Newtonian liquid flow in the jet read:

$$\nabla \cdot \mathbf{u} = 0, \tag{2.1a}$$

$$\frac{D\mathbf{u}}{Dt} = -\nabla p + \frac{1}{Re}\nabla \cdot (2\boldsymbol{D}) - \frac{1}{Rb^2}\Omega \times (\Omega \times \mathbf{d}) - \frac{2}{Rb}\Omega \times \mathbf{u} + \frac{1}{Fr^2}\mathbf{g}, \tag{2.1b}$$

where $\mathbf{g} = (0,0,-g)$ and $\boldsymbol{D} = \left(\nabla\mathbf{u} + \nabla\mathbf{u}^T\right)/2$ is the rate-of-strain tensor and $\mathbf{d}$ is the distance vector with respect to the rotating axis. The definitions and values of the nondimensional numbers are provided in table 2.1. The mathematical framework we use is
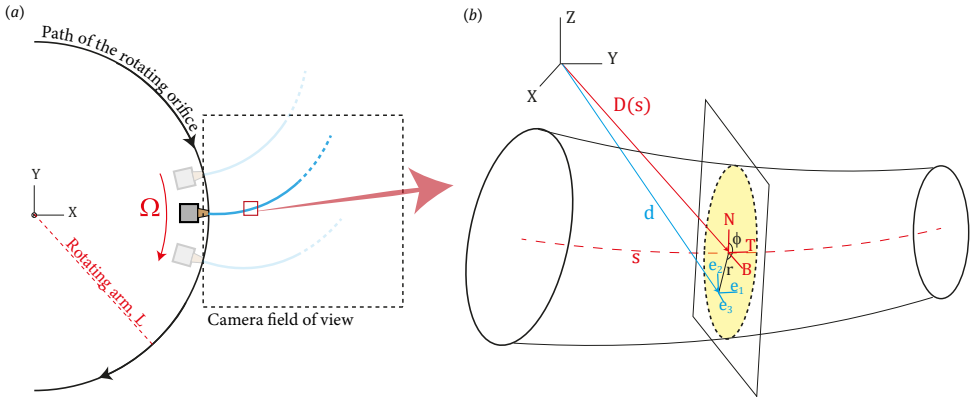

Figure 2.2: (*a*) Schematic of the top view of the setup. (*b*) Close-up view of a section in the jet showing the different coordinate frames.

very similar to what is described in detail in [18, 20], but briefly revisited here for completeness. Figure 2.2 shows a schematic of a curved jet. We start by describing a baseline

[18], that is a spline which goes along the jet and staying inside it, using Cartesian basis vectors on a frame rotating with Ω (see Figure 2.2a):

$$\mathbf{D}(s) = X(s)\hat{\mathbf{x}} + Y(s)\hat{\mathbf{y}} + Z(s)\hat{\mathbf{z}}, \tag{2.2}$$

where s is the arclength. From (2.2) the Frenet basis can be defined, i.e., a local orthogonal basis defined at every point on the baseline:

$$\mathbf{T}(s) \;=\; \frac{d\mathbf{D}}{ds} = X'(s)\hat{\mathbf{x}} + Y'(s)\hat{\mathbf{y}} + Z'(s)\hat{\mathbf{z}} \quad \left(X'^2 + Y'^2 + Z'^2 = 1\right), \tag{2.3a}$$

$$\mathbf{N}(s) \;=\; \frac{d\mathbf{T}}{ds}\left|\frac{d\mathbf{T}}{ds}\right|^{-1} = \frac{X''\hat{\mathbf{x}} + Y''\hat{\mathbf{y}} + Z''\hat{\mathbf{z}}}{\sqrt{X''^2 + Y''^2 + Z''^2}}, \tag{2.3b}$$

$$\mathbf{B}(s) \;=\; \mathbf{T} \times \mathbf{N}, \tag{2.3c}$$

where a prime denotes derivative with respect to s. The derivatives of the Frenet base vectors are related to each other by the Frenet formulas:

$$\frac{d}{ds}\left[\begin{array}{c} \mathbf{T} \\ \mathbf{N} \\ \mathbf{B} \end{array}\right] = \left[\begin{array}{ccc} 0 & \kappa & 0 \\ -\kappa & 0 & \tau \\ 0 & -\tau & 0 \end{array}\right]\left[\begin{array}{c} \mathbf{T} \\ \mathbf{N} \\ \mathbf{B} \end{array}\right]. \tag{2.4}$$

Here $\kappa(s)$ and $\tau(s)$ are, respectively, the local curvature and the local torsion of the baseline, given by:

$$\kappa(s) \;=\; \sqrt{X''^2 + Y''^2 + Z''^2}, \tag{2.5a}$$

$$\tau(s) \;=\; \frac{X'(Y''Z''' - Z''Y''') + Y'(Z''X''' - X''Z''') + Z'(X''Y''' - Y''X''')}{(Y'Z'' - Z'Y'')^2 + (Z'X'' - X'Z'')^2 + (X'Y'' - Y'X'')^2}. \tag{2.5b}$$

Let us now define the curvilinear coordinate variables, (s, r, ϕ), where s is again the arc length variable, and (r, ϕ) are the polar radius and angle, respectively, on the plane that is normal to the baseline at $\mathbf{D}(s)$. Notice from the definition of the Frenet basis (2.3) that this is also the plane where $\mathbf{N}(s)$ and $\mathbf{B}(s)$ lie. So we can define an arbitrary point in the jet with a position vector measured from the origin in the Cartesian and curvilinear coordinates as follows:

$$\mathbf{d}(x, y, z) \;=\; x\hat{\mathbf{x}} + y\hat{\mathbf{y}} + z\hat{\mathbf{z}}, \tag{2.6a}$$

$$\mathbf{d}(s, r, \phi) \;=\; \mathbf{D}(s) + r\cos\phi\mathbf{N}(s) + r\sin\phi\mathbf{B}(s). \tag{2.6b}$$

The free surface can be parametrically described as $r = R(s, \phi)$, with which the position vector to the free surface takes the form:

$$\mathbf{d}(s, R(s, \phi), \phi) = \mathbf{D}(s) + R(s, \phi)\cos\phi\mathbf{N}(s) + R(s, \phi)\sin\phi\mathbf{B}(s). \tag{2.7}$$

On the free surface one has the balance of stresses in normal and tangential direction:

$$\mathbf{n}\cdot\left(-p + \frac{1}{Re}2\boldsymbol{D}\right)\cdot\mathbf{n} \;=\; -\frac{1}{We}\kappa_{fs}, \tag{2.8a}$$

$$\mathbf{t_i}\cdot\left(-p + \frac{1}{Re}2\boldsymbol{D}\right)\cdot\mathbf{n} \;=\; 0, \quad i = s, \phi, \tag{2.8b}$$

where κ_{fs} is the curvature of the free surface. Here, the ambient phase is assumed to be dynamically inert and the effect of air drag is neglected.

We will use the notation $(s^1, s^2, s^3) = (s, r, \phi)$, to define the base vectors of the curvilinear coordinate frame as:

$$\mathbf{e}_i = \frac{\partial \mathbf{d}}{\partial s^i} \qquad (i = 1, 2, 3). \tag{2.9}$$

Using 2.9, we can now express curvilinear base vectors in terms of the Frenet frame as follows:

$$\begin{bmatrix} \mathbf{e}_1 \\ \mathbf{e}_2 \\ \mathbf{e}_3 \end{bmatrix} = \begin{bmatrix} 1 - r\kappa\cos\phi & -r\tau\sin\phi & r\tau\cos\phi \\ 0 & \cos\phi & \sin\phi \\ 0 & -r\sin\phi & r\cos\phi \end{bmatrix} \begin{bmatrix} \mathbf{T} \\ \mathbf{N} \\ \mathbf{B} \end{bmatrix}. \tag{2.10}$$

The metric of this basis, $\boldsymbol{g}$, defined as $g_{ij} = \mathbf{e_i} \cdot \mathbf{e_j}$, is given by:

$$\boldsymbol{g} = \begin{bmatrix} (1 - r\kappa\cos\phi)^2 + (r\tau)^2 & 0 & r^2\tau \\ 0 & 1 & 0 \\ r^2\tau & 0 & r^2 \end{bmatrix}. \tag{2.11}$$

Notice that the coordinate frame defined by (2.9) is not orthogonal as g_{13} and g_{31} are not zero in the presence of torsion or outside the baseline ($r \neq 0$). Another aspect of the curvilinear base is that two base vectors, namely $\mathbf{e}_1$ and $\mathbf{e}_3$, are not unit vectors since $g_{11} \neq 1$ and $g_{33} \neq 1$. As a consequence, there is a change in magnitude when a vector $\mathbf{v} = (v^1, v^2, v^3)$ is projected onto the curvilinear base. For instance, the projection of the velocity vector $\mathbf{u}$ on the curvilinear base is represented by: $v^1\mathbf{e}_1 + v^2\mathbf{e}_2 + v^3\mathbf{e}_3 = u_s\mathbf{e}_1/|\mathbf{e}_1| + u_r\mathbf{e}_2/|\mathbf{e}_2| + u_\phi\mathbf{e}_3/|\mathbf{e}_3|$ where u_s, u_r and u_ϕ are the physical components of the velocity using the normalized base vectors.

The inverse metric tensor (g^{ij}) is defined by $g^{ik}g_{kj} = \delta^i_j$, where δ^i_j is Kronecker delta, and is given by:

$$\boldsymbol{g}^{-1} = \frac{1}{\Delta} \begin{bmatrix} r^2 & 0 & -r^2\tau \\ 0 & \Delta & 0 \\ -r^2\tau & 0 & (1 - r\kappa\cos\phi)^2 + (r\tau)^2 \end{bmatrix}, \tag{2.12}$$

with $\Delta = \det(g_{ij}) = r^2 (r\kappa(s)\cos(\phi) - 1)^2$ the determinant of the metric tensor.

Using the metric and its inverse, we can express the gradient operator as follows [31]:

$$\nabla = g^{ij}\mathbf{e}_j \frac{\partial}{\partial s^i} = \left(\frac{1}{e_{1T}^2} \frac{\partial}{\partial s} - \frac{\tau}{e_{1T}^2} \frac{\partial}{\partial \phi} \right) \mathbf{e}_1 + \frac{\partial}{\partial r}\mathbf{e}_2 + \left(\frac{g_{11}}{r^2 e_{1T}^2} - \frac{\tau}{e_{1T}^2} \right) \mathbf{e}_3, \tag{2.13}$$

with $g_{11} = (1 - r\kappa\cos\phi)^2 + (r\tau)^2$ being the first element of the metric tensor given in (2.11) and $e_{1T} = 1 - r\kappa\cos\phi$ is the tangential component of the local base vector in s-direction, namely the first element of the transformation matrix given in (2.10).

Finally, the coefficients to connect the variations of the base state vectors (also known as the Christoffel symbols of the second kind Γ^k_{ij}, such that $\frac{\partial \mathbf{e}_i}{\partial s^j} = \Gamma^k_{ij}\mathbf{e}_k$) can be written as:

$$\Gamma^k_{ij} = \frac{g^{kl}}{2} \left(\frac{\partial g_{lj}}{\partial s^i} + \frac{\partial g_{li}}{\partial s^j} - \frac{\partial g_{ij}}{\partial s^l} \right). \tag{2.14}$$

The full expressions of each Christoffel symbol are provided in Appendix 2.C. From here onwards, it is the tedious book keeping to determine the terms in (2.1a) and (2.1b) in curvilinear coordinates. This was achieved by the help of the symbolic mathematics module SymPy [32]. Some of the terms in the conservation equations in general curvilinear coordinates are provided in Appendix 2.C.

To pave the way for the slender jet approximation, one needs to acknowledge the existence of two disparate length scales existing in the problem. These are namely the rotating arm, L, and the orifice radius, R_0. We scale s with L and r with R_0. The velocity at the orifice, U_0, is used for scaling the velocity in s-direction, so the advective timescale becomes $t_{adv} = L/U_0$. Finally, the pressure is scaled with ρU_0^2.

2.3.2. JET TRAJECTORY & BASE FLOW

To obtain the leading order steady state equations for the spiralling jet trajectory, one needs to consider the limit where the jet slenderness ϵ tends to zero, i.e. $R_0/L \to 0$. The steady state jet base flow equations, namely, the mass conservation, the T-N-B projections of the momentum conservation and the arc length condition have the following form:

$$\frac{d}{ds}\left(UR^2\right) = 0,$$
(2.15)

$$U\frac{dU}{ds} = -\frac{1}{We}\frac{d}{ds}\left(\frac{1}{R}\right) + \frac{3}{R^2 Re}\frac{d}{ds}\left(R^2\frac{dU}{ds}\right) \underbrace{- \frac{Z'}{Fr^2}}_{f_{gravity}} + \underbrace{\frac{XX' + YY'}{Rb^2}}_{f_{centrifugal}},$$
(2.16)

$$\left(U^2 - \frac{1}{RWe} - \frac{3}{Re}\frac{dU}{ds}\right)\left(X''^2 + Y''^2 + Z''^2\right) = \frac{XX'' + YY''}{Rb^2}$$
$$- \frac{2U\left(X'Y'' - Y'X''\right)}{Rb} - \frac{Z''}{Fr^2},$$
(2.17)

$$0 = \frac{X\left(Y'Z'' - Z'Y''\right) + Y\left(Z'X'' - X'Z''\right)}{Rb^2} - \frac{X'Y'' - Y'X''}{Fr^2} + \frac{2UZ''}{Rb},$$
(2.18)

$$X'^2 + Y'^2 + Z'^2 = 1.$$
(2.19)

These equations form a closed system for $X(s)$, $Y(s)$, $Z(s)$, the Cartesian coordinates of the baseline of the jet, and $R(s)$, $U(s)$, which express the local velocity and jet thickness. The factor 3 in front of the 2nd term on the right hand side of (2.16) is the Trouton number that represents the ratio of extensional to shear viscosity. It appears naturally in the asymptotic expansion of the governing equations. In the inviscid limit ($Re \gg 1$), which approximately hold for our experiments, equation (2.16) can be combined in a single integrand and readily integrated as:

$$U^2 + \frac{2U^{1/2}}{We\sqrt{C_1}} + \frac{2}{Fr^2}Z - \frac{1}{Rb^2}\left(X^2 + Y^2\right) + C_2 = 0,$$
(2.20)

where we used $UR^2 = C_1$ from (2.15), and C_1 and C_2 are integration constants. Note that viscous resistances to bending and twisting are also neglected in this case.

The rotation path of the orifice lies on the XY-plane, as shown in figure 2.2(a). We define $X(0) = 1$, $Y(0) = 0$, $Z(0) = 0$, $X'(0) = 1$, $Y'(0) = 0$ and finally $Z'(0)$ from (2.19), i.e., the jet is issued in the X-direction. The nozzle velocity U_0 and the radius R_0, which have been used for nondimensionalization, set the base flow boundary conditions as $U(0) = R(0) = 1$ and hence $C_1 = 1$. Combining all the prescribed boundary conditions in (2.20) yields $C_2 = 1/Rb^2 - 2/We - 1$.

We solve the system (2.15), (2.17)-(2.20), also known as the "string" equations, with the prescribed boundary conditions and the nondimensional numbers given in table 2.1 using a fourth order Runge-Kutta method. The results are summarized in figure 2.3. The base jet trajectory is in great agreement with the experiments, so it enables the quantification of the projections of the body forces along the trajectory, namely, the centrifugal force, $f_{centrifugal}(s)$, and gravity force, $f_{gravity}(s)$, whose expressions are given at the right hand side of (2.16). Figure 2.3 depicts the results from the base flow calculations. It is apparent that with the parameters in our experiment, the gravity force is about an order of magnitude smaller than the centrifugal force, which suggests that the torsion along the arc length and distance travelled by the jet in the Z direction are negligibly small, allowing to study the dynamics from 2D projections onto the XY-plane.
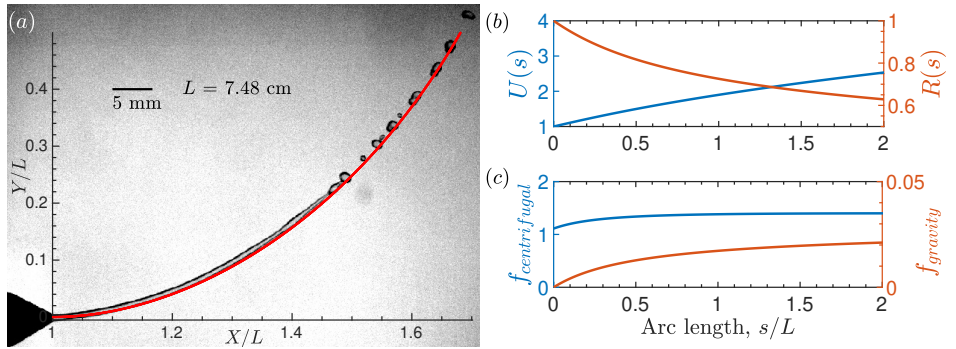
Figure 2.3: Results from the base flow computation. (a) Comparison of calculated jet trajectory (red line) with a snapshot from an unperturbed jet experiment. (b) The variation of the base state velocity, $U(s)$, and jet radius, $R(s)$, along the jet. (c) The variation of the body forces acting along the jet due to rotation $f_{centrifugal} = (XX' + YY')/Rb^2$ and gravity $f_{gravity} = -Z'/Fr^2$.

2.3.3. Nonlinear slender jet model

To be able to capture the dynamics close to breakup, e.g. the formation of main and satellite droplets, nonlinear simulations are necessary. Once the longitudinal projections of the centrifugal and the gravity forces are accounted for, one can approximate the nonlinear dynamics of the jet along the flow direction with an error of $O(\epsilon)$, provided that the full free surface curvature is accounted for [19]. In other words, the 3D spiralling trajectory of the jet can be represented as a quasi-straight jet with locally varying body forces. This also amounts to the implicit assumption that that the wavenumber of the

perturbations k (scales with R_0^{-1}) is much larger than the curvature κ and the torsion τ of the base jet trajectory (both scale with L^{-1}) which is valid in the limit $\epsilon \to 0$. To this end, we implemented a slender jet approximation, detailed in [21, 25], which yields the following unsteady 1D equations for the jet flow:

$$\frac{\partial A}{\partial t} + \frac{\partial}{\partial s}(uA) = 0, \tag{2.21a}$$

$$\frac{\partial(uA)}{\partial t} + \frac{\partial}{\partial s}\left(u^2 A\right) = \frac{\partial}{\partial s}\left[A\left(\frac{K}{We} + \frac{3\epsilon}{Re}\frac{\partial u}{\partial s}\right)\right] + A\left[\epsilon\left(f_{centrifugal} + f_{gravity}\right)\right], \tag{2.21b}$$

$$K = \frac{2}{\sqrt{4A + A_s^2}} + \frac{4AA_{ss} - 2A_s^2}{\left(4A + A_s^2\right)^{3/2}}, \tag{2.21c}$$

where $A = R^2$ is the normalized local jet cross-sectional area. Note that the full expression for the curvature is used (i.e., both radii of curvature instead of only the leading order one in the expansion). This is key to the success of the slender jet framework [33, 34].

Note the inclusion of the ϵ parameter in front of the centrifugal and gravity force in (2.21b) as they have been taken from (2.16) and are hence normalised with L instead of R_0. (2.21) form a closed system for the jet cross-sectional area $A(s, t)$ and jet velocity $u(s, t)$. The initial conditions are implemented as $A(s, 0) = R(s)^2$ and $u(s, 0) = U(s)$ from the base flow computations detailed in §2.3.2. At the nozzle, we input the velocity fluctuations as $u(0, t) = 1 + \varepsilon_v \cos(\omega t)$ on top of the Gaussian white noise which is mentioned in §2.4. A regularized capillary pressure is implemented to carry the simulations beyond the pinchoff point [35]. A finite difference scheme on a staggered grid is used for solving the system given in 2.21. The time integration is done explicitly by using a three-step Runge-Kutta scheme with an adaptive time stepping. Except for velocities, a central differencing scheme is used for evaluating the variables at their half step neighbors. For velocities a higher-order total variation diminishing (TVD) van Leer scheme is used. More details of the numerical method and validation can be found in [25].

Mechanical vibrations are naturally present in industrial applications of spiralling jets such as in prilling, where the typical size of the rotating perforated bucket is on the order of 50 cm. Even in small-scale laboratory experiments, one can never get fully rid of such vibrations, and they might have a significant effect on the jet breakup. The time series of such noisy perturbations are rather difficult to quantify, however, a good proxy is to represent the vibrations by white noise and to characterize the noise strength in terms of the natural (actuation-free) jet breakup length or breakup time [36].

To simulate the natural breakup in the slender jet framework, we add Gaussian white noise to the nozzle velocity as follows:

$$u(0, t) = 1 + \underbrace{\varepsilon_v \cos(\omega t)}_{\text{perturbation}} + \underbrace{W(\Delta t)}_{\text{white noise}}. \tag{2.22}$$

The white noise is generated using standard random number generators in matlab and its standard deviation scales as $S\Delta t$ where S is a strength parameter and Δt is the computational timestep. This ensures that the forcing due to the white noise is uncorrelated

with the timestep [25]. The strength parameter S is then calibrated using the observed experimental natural (i.e., $\varepsilon_v = 0$) breakup length. In the present study we subsequently used $S = 300$ in all simulations and the nondimensional timestep Δt is adjusted dynamically considering the stability restrictions based on the effects of advection, diffusion and surface tension [31, 37].

The comparison of the simulation and experiments for the parameters listed in table 2.1 and in the presence of only background noise, is summarized in table 2.2.

	Simulation	Experiment
Breakup length, L_b	98.0 ± 6.0	95.4 ± 7.8
Drop projected area, A_p	6.7 ± 3.8	8.3 ± 5.4

Table 2.2: Mean and standard deviation of the breakup properties of natural (actuation-free) breakup cases. The breakup length is expressed in terms of the nozzle radius R_0 and the drop projected area is represented in terms of R_0^2.

2.4. COMPARISON OF SIMULATIONS WITH EXPERIMENTS FOR JET BREAKUP

Simulations and experiments have been conducted for the parameter settings listed in table 1 and for three different actuation frequencies (ω). The strength of perturbations was varied by varying the velocity perturbation amplitude (ε_v) in the simulations and the oscillation amplitude of the piezo-actuator (Δh_{piezo}) in the experiments. The simulation results from the slender-jet model for the jet interface have been projected from the curvilinear to the Cartesian frame using 2.7. Figure 2.4(*a*) shows the comparison of a slender jet simulation and an experiment at $\omega = 0.7$ and in figure 2.4(*b*) we show the change in the mean intact length with respect to the perturbation amplitude at different frequencies. Note that in figure 2.4(*b*) we shifted the axes for Δh_{piezo} and ε_v as to give a best match between simulations and experiments. The simulations and experiments agree well in terms of trajectory and the jet shape. The presence of the background noise brings in a threshold for the finite amplitude perturbations to overcome the noise and control the breakup of the spiralling jet, which can be observed in figure 2.4(*b*). The errorbars show the standard deviation around the mean for the time series of the jet intact length, defined as the distance in s from the nozzle exit till the location at which pinch-off takes place. This indicates how much the perturbations are coupled to the system, namely, the less the intact length fluctuates, the more the finite amplitude perturbations are coupled to the jet, hence better control.

To make the comparisons between simulations and experiments conveniently, we show the spiralling jet in a space time plot in figure 2.5 (without actuation) and figure 2.6 (with actuation) by stitching consecutive time images together. This also allows to inspect the motion of the droplets after the pinchoff event, such as capillary oscillations and rotation. The time difference between instants is $\Delta t = 0.8$ ms, during which the orifice rotates $\pi/150$ radians. By comparing figures 2.5 and 2.6 it is clear that jet actuation helps in
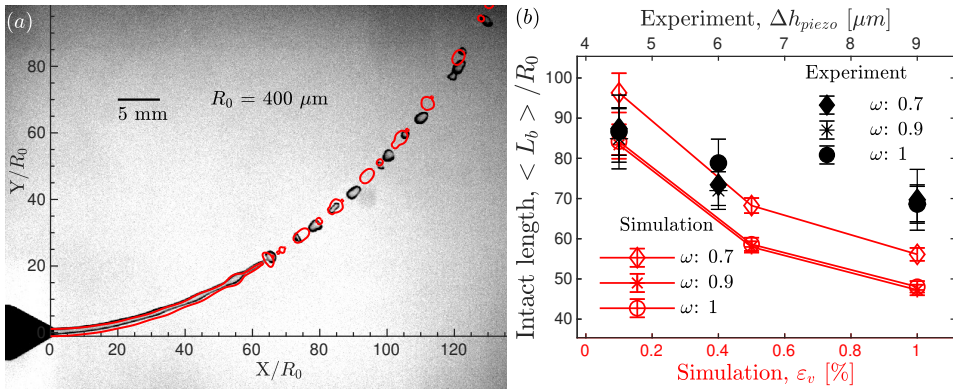
Figure 2.4: (*a*) Comparison of the jet interfaces obtained from simulation (shown in red) and from experiment at a perturbation frequency $\omega = 0.7$. The piezoplate displacement is $6\ \mu m$ and the velocity amplitude in the simulation is 0.5% (*b*) Mean and standard deviation of the jet intact length as function of piezoplate displacement in the experiments and velocity perturbation amplitude in the simulations.

achieving a regular jet breakup and reduces the fluctuation in the jet intact length. Also, the comparison of the drop size distributions in figures 2.5(*c*) and 2.6(*c*) reveal a narrower distribution around the mean projected drop area when the jet is actuated. Overall the agreement between the experiments and simulations is good. Figures 2.5 and 2.6 also allow for a qualitative comparison in terms of the late jet dynamics, formation of satellite drops and droplet motion after pinch off.

For the unperturbed jets, the intact length of the jet fluctuates at a higher standard deviation than their perturbed counterpart. The jets often emit filaments that are a few wavelengths long which fragments into droplets after separating from the main jet. Due to the thinning and stretching of the jet, the high-frequency perturbations which are initially stable and damped, may become unstable downstream. Therefore a larger window of wavelengths is involved in the instability process as compared to the Rayleigh window for straight jets in the absence of external forces.

In the presence of jet actuation, the jet intact length fluctuations are suppressed and the jet regularly emits a filament which breaks up either at the forward/downstream end or the rear/upstream end. For straight jets it is known that the location of the breakup within a single filament depends both on perturbation frequency and amplitude [36]. If the breakup occurs at the forward end, the satellite drop merges with the main drop that is following it, within a distance of a few wavelengths. Within a narrow window of amplitudes at a given frequency, the breakup location shifts from the downstream end to the rear end, which is the desired regime for applications such as continuous ink jet printing as the satellite drop merges with the leading main drop [23]. The main mechanism of merging is the momentum transfer during the finite time between the 2 successive pinchoff events, also known as the satellite interaction time [36]. In our simulations and experiments, the typical merging length relative to jet pinch-off in all cases
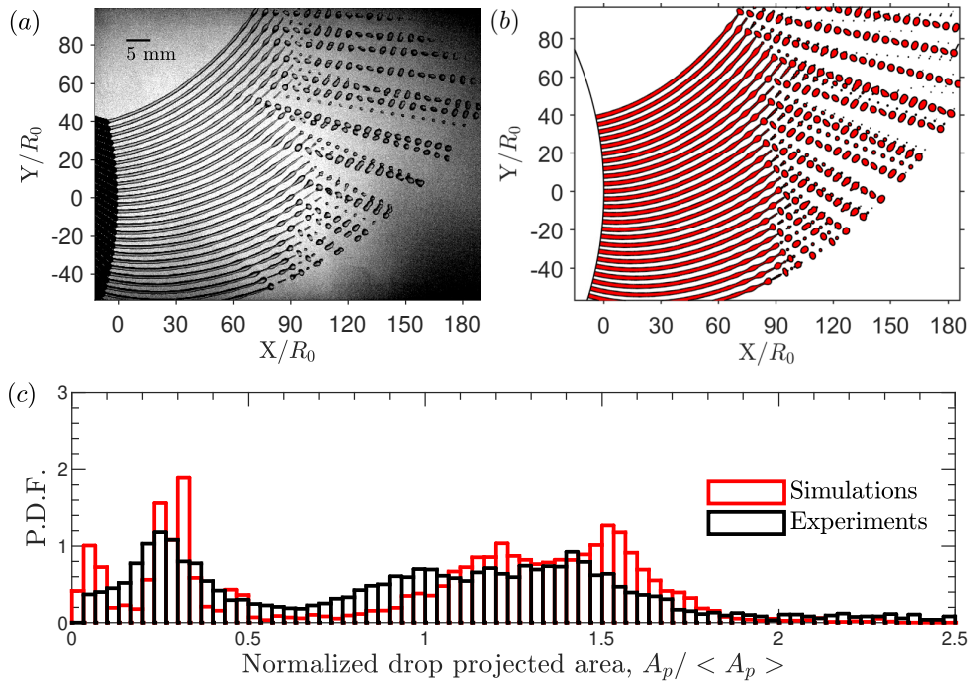
Figure 2.5: Comparison between experiment and simulation for the natural (actuation-free) breakup case. (*a*) Experiment. (*b*) Simulation. (*c*) Comparison of the drop projected area normalized by the mean.

is about 2-3 wavelengths. The proportion of the main and satellite droplet volumes are given in figure 2.7. The volumes are normalized with the jet volume over one perturbation wave length at nozzle exit, which is conserved under wave length stretching downstream due to mass conservation. At a given frequency, the perturbation amplitude determines where the droplets are formed, i.e., lower amplitudes result in droplets formed further downstream. The proportion of the volumes of the main and satellite droplets converge as they are formed further downstream. For a nozzle frequency of $\omega = 1.2$, which is initially outside of the Rayleigh window, one can see a larger variation in the drop volume and location. This is attributed to the fact that the unstable frequencies of the white noise gain enough to interfere with the imposed finite amplitude perturbation. Therefore the jet volume enclosed by the imposed perturbation wave length at nozzle exit becomes irrelevant and one can see the droplet volumes are exceeding the volume expected from the imposed perturbation.

The fact that the droplets stay in the base jet trajectory in the experiments (see figure 2.6) verifies that it is a good approximation to assume that the jet trajectory is steady in the rotating frame and to separate the calculation of the base flow and the drop formation. After the pinchoff, the droplets travel in a straight line with respect to the stationary
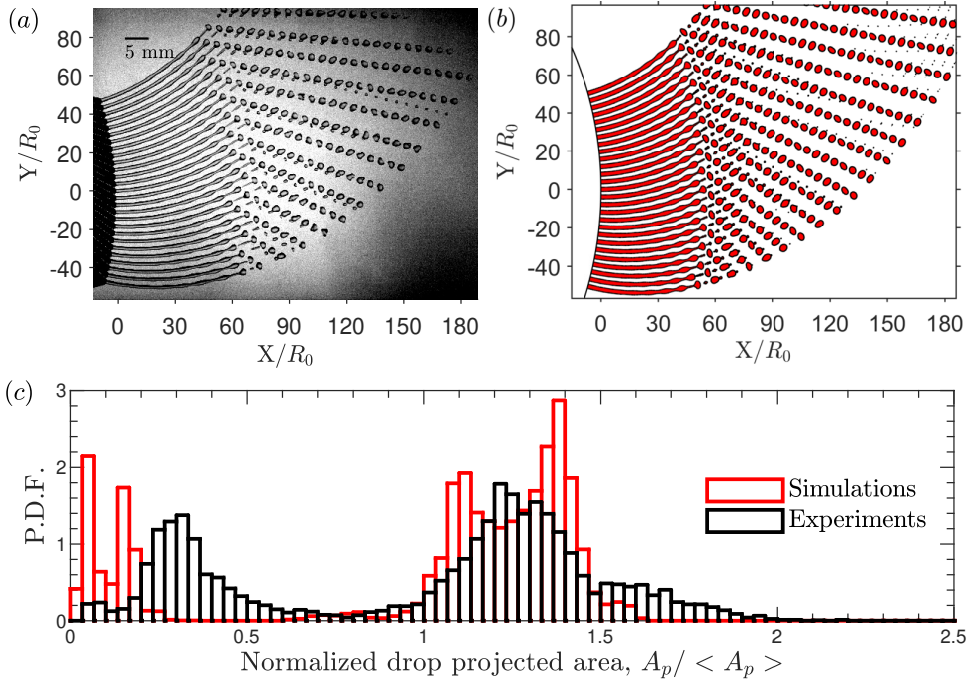
Figure 2.6: Comparison between experiment and simulation in the presence of actuation with $\omega = 0.9$. (*a*) Experiments with a piezoplate displacement of 6 μm. (*b*) Simulations with a velocity amplitude 0.5%. (*c*) Comparison of the drop projected area normalized by the mean.

frame, preserving their linear momentum.

The satellite interaction time leads to another phenomenon in the context of spiralling jets. With straight jets, the momentum transfer is always in the direction of the flow and the satellite drop is either sped up or slowed down depending on the location of the first pinchoff (forward or rear). When the spiralling jets are captured in stationary frame (figure 2.6), one can observe that the capillary oscillation of the droplets is superposed with a rotation around principal axis. The curved nature of the trajectory results in slight variation of the tangential and the normal vectors from the front-end to the rear-end of the droplets, which leads to a moment around the principal axis and breaks the symmetry of the detached drop around the tangential direction. The locality of the forces along the flow direction imposes a moment during the satellite interaction time, causing the drop oscillations to be 3D in nature.

As the perturbations grow and the amplitude becomes finite, the shape deformations of the jet are sufficiently large where the dynamics enter a nonlinear regime. The formation of the main and satellite droplets is a nonlinear phenomenon by nature. The evolution of the velocity perturbations deviates from its linear counterpart (i.e., normal
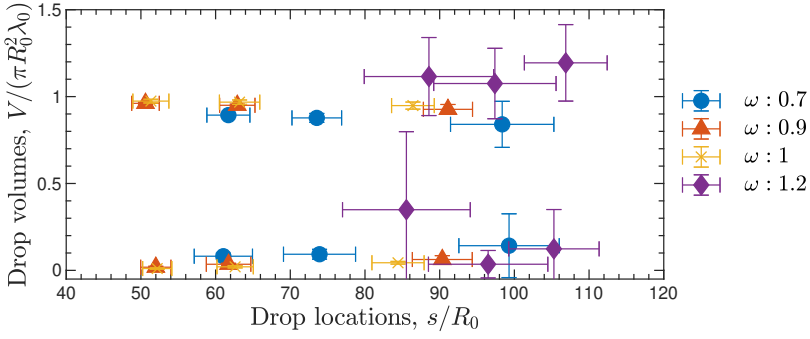
Figure 2.7: Volumes of the main and satellite droplets obtained from the simulations as a function of their location of first appearance. For each frequency three points are shown, corresponding to different perturbation amplitudes (drops are formed further downstream for smaller amplitudes).

mode), shown in figure 2.8 for $\omega = 0.9$, as the satellite droplets begin to form. It manifests itself as the fluctuations take the form of triangular waves starting from the sinusoidal. On the other hand the nonlinear growth rate is in agreement with the linear estimation until very close to the breakup, which is partly due to the fact that the studied case is close to the inviscid limit, where the time scale for axial momentum diffusion is large compared to the inertio-capillary timescale during the early stage of the growth. In other words, the jet is sufficiently deformed only very close to the breakup for viscosity to play a role.
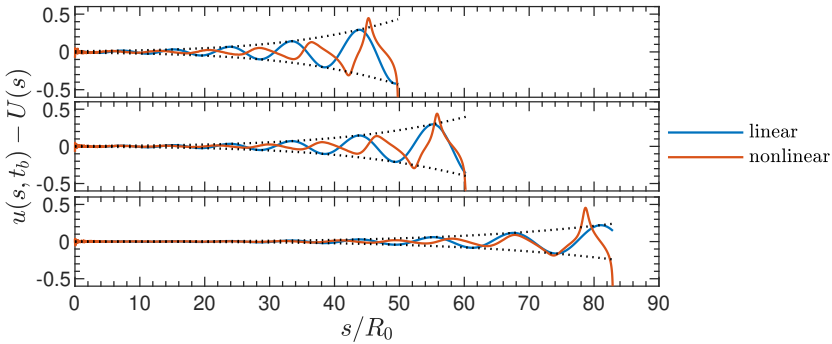

Figure 2.8: Comparison of the linear and nonlinear evolution of the velocity perturbations for $\omega = 0.9$ at different velocity perturbation amplitudes at the nozzle, with decreasing strength from top to the bottom. t_b refers to the instant of jet breakup. The dotted lines represent the envelope of the velocity perturbations computed from the linear model detailed in §2.5.

2.5. ANALOGY WITH GRAVITY-DRIVEN STRAIGHT JETS: APPROXIMATE BASE FLOW SOLUTIONS, LINEAR STABILITY & SELF-SIMILARITY

The agreement between the experiments and simulations demonstrates the validity of modelling spiralling jets as quasi-straight and slender jets with locally varying pseudo forces provided that epsilon is sufficiently small. These forces, and the variation thereof, can be computed from the base trajectory of the jet as discussed in §2.3.2. Once the base flow of the jet and the variation of the body forces have been accounted for, one can use these to study the stability of this flow to perturbations. In this section we will linearize the slender-jet model for a linear spatial stability analysis of the flow to infinitesimally small perturbations imposed at nozzle exit. We will show that this analysis provides insight in the dynamics underlying jet breakup and in the scaling behaviour for the spatial growth rate and jet breakup.

To study how perturbations evolve along the jet, one needs to pay attention to the disparate length scales present in this problem. In §2.3.2 where the base flow and the trajectory was calculated in the limit $\epsilon \to 0$, all lengths are expressed in terms of the rotating arm L and the base flow equations represent the jet as a "string" whose thickness is $O(\epsilon L)$. When we consider capillary waves along the jet, their wavelengths are of the same order as the jet radius so their growth should be expressed along $s/(\epsilon L)$, i.e., in units of jet radius instead of the rotating arm. Similarly, while the advective scale of the base flow is $t_{adv} = L/U_0$, the relevant advective time time for the perturbations is $R_0/U_0 = t_{adv}/\epsilon$. In what follows, we will express all the lengths in terms of the nozzle radius and the length of the rotating arm L will only appear in the expression of the body forces. Furthermore, we introduce an effective gravity $g_e \sim O(\Omega^2 L + g)$ that measures the combined effect of rotational and gravitational forces. Using this, we define the effective capillary length as $l_c = \sqrt{\gamma/\rho g_e}$ and an effective Bond number $Bo_e = (R_0/l_c)^2 = \rho g_e R_0^2/\gamma$. In terms of (We, Rb, Fr) given in table 2.1, the latter can be expressed as:

$$Bo_e(We, Fr, Rb) = We\left(\frac{\epsilon}{Rb^2} + \frac{\epsilon}{Fr^2}\right). \tag{2.23}$$

Using (2.23), one could follow the same line of gain analysis developed for straight jets in [29]. For the given experimental case with the nondimensional numbers presented in table 2.1, the variation of the body forces along the jet is minor, see figure 2.3(c). The centrifugal forces are very close to their nozzle value throughout the entire jet and gravitational forces, which would make the jet travel in the Z-direction and cause torsion, are an order of magnitude smaller than the centrifugal forces. In this case, the spiralling jet thus behaves like a gravity-driven straight jet with the gravitational acceleration replaced by the initial centrifugal acceleration at nozzle exit, namely, $U(dU/ds) = Bo_e/We$, as the viscous and curvature effects decay rapidly after the nozzle exit. One thus has:

$$U(s) = \sqrt{\frac{2Bo_e}{We}s + 1}, \tag{2.24a}$$

$$R(s) = \left(\frac{2Bo_e}{We}s + 1\right)^{-1/4}. \tag{2.24b}$$

A comparison between the "free-fall" solution (2.24) and the solution of the base flow equations (2.20) is given in figure 2.9.
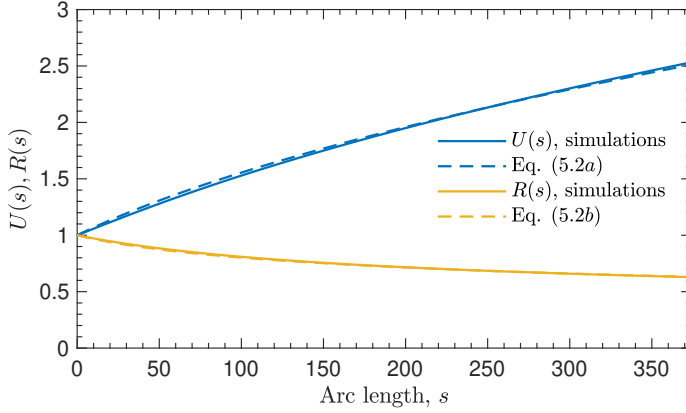

Figure 2.9: The comparison between the base flow solutions from (2.15), (2.17)-(2.20) and the approximate "free-fall" solutions given in (2.24).

This assumption can be made a priori if $We \gg Bo_e$ for We large enough to stay in the jetting regime [38]. The arc length s can be recast as a slowly varying dimension

$$\xi = \frac{s}{s_0} + 1, \qquad s_0 d\xi = ds, \tag{2.25}$$

for large s_0, where $s_0 = We/2Bo_e$ is the variation scale [29, 30], such that (2.24) becomes:

$$U(\xi) = \sqrt{\xi}, \tag{2.26a}$$
$$R(\xi) = \xi^{-1/4}, \tag{2.26b}$$

respectively.

We now consider perturbations to the base flow of the following form

$$(\tilde{u}, \tilde{R}) = (u(\xi), r(\xi)) e^{i\left(s_0 \int_1^\xi k(\xi') d\xi' - \omega t\right)}, \tag{2.27}$$

where $k = k_r + ik_i$ is the complex wave number, $k_r = 2\pi/\lambda$ is the real wave number with λ the perturbation wavelength (normalised with R_0), $-k_i$ is the spatial growth rate and ω is the real perturbation frequency imposed at the nozzle. Plugging $U + \tilde{u}$ and $R + \tilde{R}$ into (2.21a)-(2.21c) and considering the terms linear in $(\tilde{u}, \tilde{R})$ up to $O(1/s_0)$ yields:

$$(kU - \omega) r(\xi) + \frac{kR}{2} u(\xi) = O\left(\frac{1}{s_0}\right), \tag{2.28a}$$

$$\left(kU - \omega - \frac{3ik^2}{Re}\right) u(\xi) + \frac{k}{R^2 We} \left(k^2 R^2 - 1\right) r(\xi) = O\left(\frac{1}{s_0}\right), \tag{2.28b}$$

which is analogous to (2.16) in [29]. This approach is also known as the WKBJ method [39], a perturbation method using expansions over the small parameter $1/s_0$ in this case. This approach is well utilized and tested in [28, 29]. The variations of the amplitudes $(u(\xi), r(\xi))$ and the base states only show up at higher orders, which means for large s_0 (i.e., $We \gg Bo_e$), the length scale of base flow variations are small compared to the perturbation wavelength. The dispersion relation is found form the non-trivial solution of equations 2.28:

$$\frac{k^2}{2RWe}\left(k^2 R^2 - 1\right) - (kU - \omega)^2 + \frac{3ik^2}{Re}(kU - \omega) = 0. \tag{2.29}$$

This equation governs the convective instability of a jet to infinitesimally small perturbations at the nozzle exit at a given frequency ω. Note that the dispersion relation (2.29) is identical to the one for a straight jet in the absence of body forces, except that here U and R are the local values instead of the nozzle values.
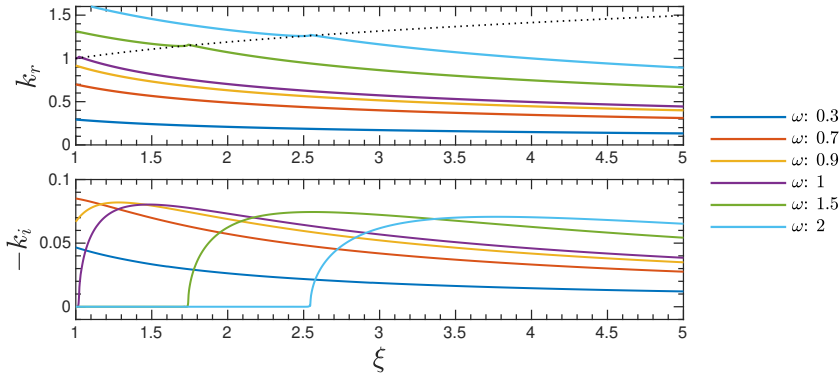
Figure 2.10: The local wavenumber ($k_r R_0$) and spatial growth rate ($-k_i R_0$) along the jet. the dotted line indicates the upper boundary of the local Rayleigh window of unstable perturbations.

The solution to the dispersion relation given in (2.29) is shown in figure 2.10. The local wavenumber, k_r, is the real part of the solution to the complex equation and it is decreasing from its nozzle value due to the thinning of the jet, also known as wavelength stretching [30]. Based on the nozzle values, the frequency that has the maximum growth rate at the nozzle is $\omega_{ini} \approx 0.718$. But as the body forces stretch the perturbed filaments, their growth rate also changes locally which leads to different gains along the jet, shown in figure 2.11(a). So a net-gain approach is preferable to study the most unstable frequencies [28, 29]. The local gain along the jet is then expressed as follows:

$$G(\xi) = e^{S(\xi)}, \qquad S(\xi) = s_0 \int_1^\xi -k_i(\xi')d\xi', \tag{2.30}$$

where $s_0 = We/2Bo_e \sim 0.5|dU/ds|_0^{-1} / (R_0/U_0)$ can be interpreted as the ratio of the initial stretching time to the initial advective time.

Figure 2.11: (*a*) Integrated gain for different frequencies of perturbation at the nozzle. The dashed vertical line indicates the location $\xi = 2.35$ which corresponds to the location of the mean jet intact length obtained from the experiments in the absence of imposed perturbations, also given in table 2.2. (*b*) The location to reach the gain necessary for breakup vs the frequency of perturbation at the nozzle
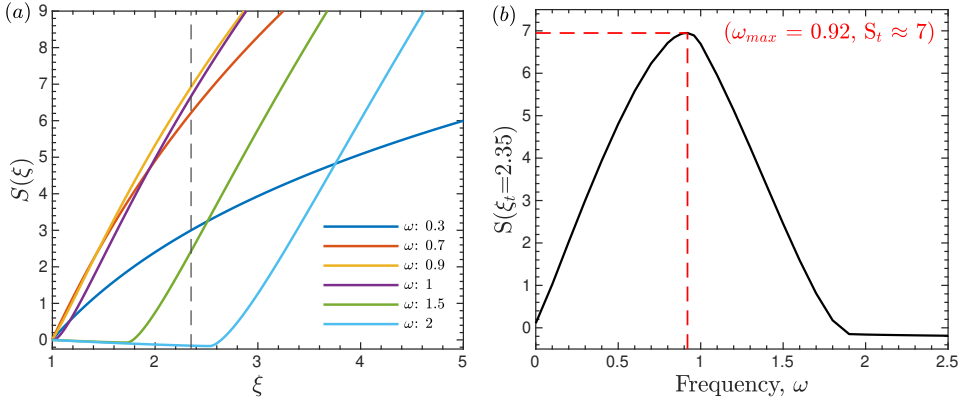
Figure 2.11(*a*) shows the gain along the jet at different frequencies and for infinitesimal amplitude, based on equation 2.30. The disturbances start to gain only when their local wavelength enters the Rayleigh window, which is indicated by the dotted line in figure 2.10. Quantification of the infinitesimal disturbances is a difficult practice both experimentally and numerically. When the gain reaches a sufficiently high value, which is assumed to be $G \approx e^7$ in [29], the transition to breakup occurs. The location of the transition ξ_t for different values of threshold gain is given in figure 2.11(*b*). For our experimental case with the parameters given in table 2.1, the assumed transition gain of $S_t \approx 7$ agrees well with the average natural breakup length for the unperturbed case of our experiments that is around 95 times the radius of the jet, see table 2.2. For the choice of $S_t \approx 7$, the frequency that gains the fastest is around $\omega \approx 0.9$.

Furthermore, self-similarity can be deduced from the dispersion relation. We will first decompose the solution of the complex equation (2.29) as follows:

$$k_r R(\xi) \quad = \quad \frac{\omega R}{U} = \omega \xi^{-3/4}, \qquad\qquad\qquad\qquad\qquad (2.31a)$$

$$-k_i R(\xi) \quad = \quad q\left(k_r R, Oh\right) We_l^{-1/2} = q\left(\omega \xi^{-3/4}, Oh\right) We^{-1/2} \xi^{-3/8}, \qquad (2.31b)$$

where q is a non-dimensional function of the local wavenumber, the perturbation frequency and the Ohnesorge number, and $We_l = We \xi^{3/4}$ is the local Weber number obtained by using the base flow solutions (2.26). Looking into the convective behaviour of the perturbations of $\omega > 1$, one can see that the initial wavelength of these perturbations are shorter than the lower boundary of the Rayleigh window (i.e. $k_r(\xi)R \leq 1$ as shown with dashed curve in figure 2.10), so these perturbations do not gain (or even damped

with higher viscosity) until the wavelength is stretched enough to enter the Rayleigh window. This motivates to do another rescaling on the flow direction, ξ, as:

$$\theta = \xi\omega^{-4/3}, \tag{2.32}$$

such that $k_r R(\theta) = \theta$ and instabilities grow for $\theta > 1$. From here, we can express (2.31) explicitly in terms of θ using the base flow solutions (2.26):

$$k_r\omega^{-1/3} = \theta^{-1/2}, \tag{2.33a}$$

$$-k_i\omega^{1/6}We^{1/2} = q\left(\theta^{-3/4}, Oh\right)\theta^{-1/8} = p(\theta, Oh), \tag{2.33b}$$

where k_r and k_i are now scaled with parameters defined at nozzle exit. Using these rescaled solutions, we can collapse the curves given in figure 2.10 onto a single curve. We can also write the integral for the gain $S(\xi)$ given in (2.30) in terms of an integral over the similarity variable θ using (2.33b):

$$S(\theta) = \frac{s_0\omega^{7/6}}{\sqrt{We}}\int_1^\theta p(\theta', Oh)d\theta'. \tag{2.34}$$
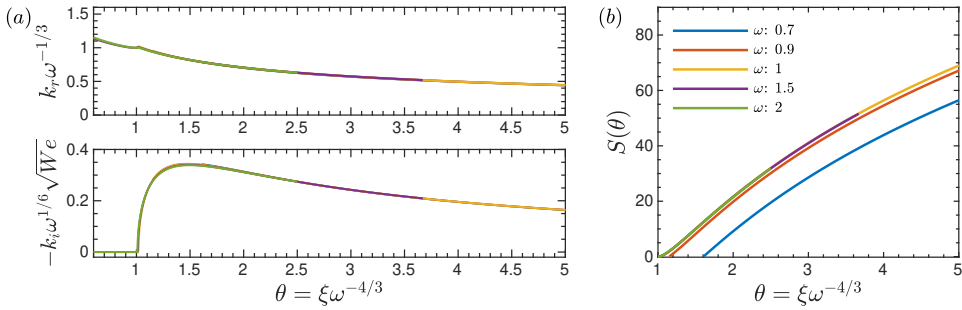
Figure 2.12: (*a*) Rescaled curves of the solution to the dispersion relation given in (2.29). (*b*) The gain associated with the rescaled curve

For a threshold gain of $S_t \approx 7$, we can then deduce the rescaled threshold distance for jet breakup, θ_t, numerically from (2.34). This is shown in figure 2.13(*a*). In figure 2.13(*b*), the threshold distance, $\xi_t = \theta_t\omega^{4/3}$, and the wavelength at breakup calculated as $\lambda(\xi_t) = \frac{2\pi}{\omega}\xi_t^{1/2}$ are shown. The prefactor $s_0/\sqrt{We} \sim 0.5|dU/ds|_0^{-1}/\sqrt{\rho R_0^3/\gamma}$ in (2.34) can be interpreted as the ratio of the initial stretching time to the initial inertio-capillary time.

As non-linear effects present in the experiments are a priori excluded from the linear stability analysis, a direct quantitative comparison between the linear stability predictions and the experiments or the nonlinear slender jet model would be flawed. Nevertheless, we made a quantitative comparison of the linear and non-linear predictions for the evolution of the perturbations for the nondimensional numbers given in table 2.1. To that end, we performed a small study where we compare the results from linear stability analysis with the nonlinear slender jet model for 2 different perturbation amplitudes and a range of frequencies.
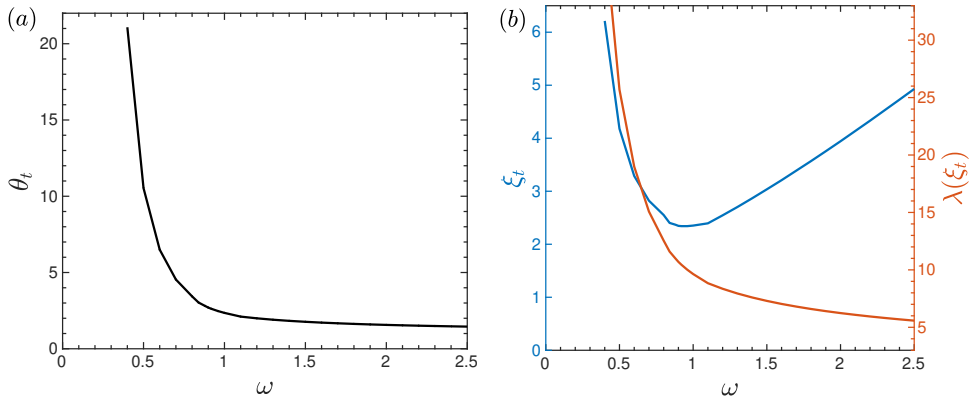
Figure 2.13: (*a*) The rescaled distance for transition to breakup, θ_t, based on (2.34) as a function of frequency. (*b*) Transition distance, ξ_t, based on (2.30) and the wavelength at the transition distance as a function of frequency calculated as $\lambda = 2\pi / k_r(\xi_t)$.
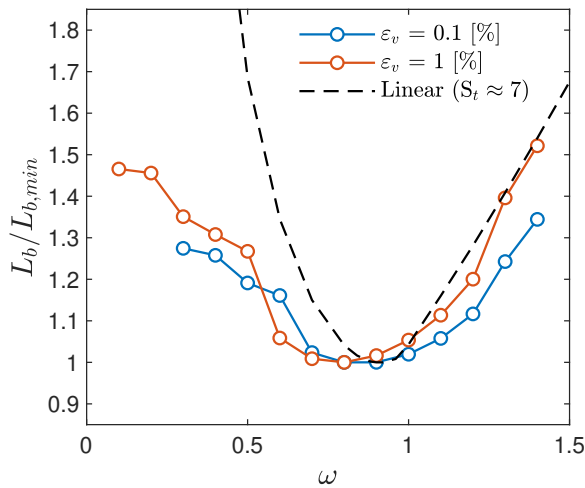
Figure 2.14: Comparison of the breakup length from linear stability theory and from nonlinear simulations for 2 different velocity fluctuation amplitudes, ε_v, as a function of the imposed perturbation frequency. To ease the comparison, the breakup length has been normalised with the minimum breakup length at the most unstable frequency. Values for $L_{b,min}$ are $91R_0$ from the linear stability, and $90.6R_0$ and $52.7R_0$ from the nonlinear simulations for $\varepsilon_v = 0.1\%$ and $\varepsilon_v = 1\%$, respectively.

Results for the jet breakup length are given in figure 2.14 where the breakup length L_b is normalized by the minimum breakup length, $L_{b,min}$. One can see that although

the value of the most unstable wavelength do agree between the linear and nonlinear predictions, the behaviour at other wavelengths differ significantly. At high frequencies (i.e. short wavelengths) and $\varepsilon_v = 1\%$, the nonlinear prediction for the jet breakup length does follow the $\omega^{4/3}$ scaling, though slightly underestimating the breakup length. However at low frequencies (i.e., long wavelengths) there is a significant overestimation of the breakup length by the linear analysis, as for $\omega \to 0$ the perturbation wavelengths become eventually large enough to be comparable to the streamwise variation scale of the base flow. To correct for this, it would be necessary to include higher order terms in 2.28, starting with terms up to $O(1/s_0^2)$ and increasing the order for smaller ω. In our study, the focus is on the frequencies that are in the vicinity of the most unstable frequencies, corresponding to the larger frequencies and smaller perturbation wavelengths for which the local plane-wave approximation underlying (2.28) is valid.

2.6. CONCLUSION

We studied the breakup of a spiralling jet using experiments, simulations based on a slender-jet model and a spatial linear stability analysis. The good agreement between the experiments and simulations validates our ansatz that the spiralling jets can be approximated as quasi-straight jets with locally varying body forces given that the cross-sectional scale of the jet (on the order of jet radius, R_0) is much smaller than the longitudinal scale at which the base flow varies (on the order of L). The locally varying body forces are the longitudinal projections of the centrifugal and gravity forces along the jet. For the given set of nondimensional parameters studied in our experiments, these longitudinal projections can be approximated by a constant effective gravity, and the base flow solution can be treated as a freely falling jet by defining an effective Bond number. The effect of the wavelength stretching manifests itself as a reduction in the inertio-capillary time scale along the jet due to thinning by the action of the effective gravity (i.e. the longitudinal projections of the centrifugal and gravity forces). Self-similar solutions for the convective linear stability have also been derived, from which a simple approximation can be derived for the jet breakup length. Despite the number of assumptions needed to proceed with this simplified approach, they are valid and relevant in many processes, such as prilling of fertilizers, where the working liquids (e.g. molten urea) have low viscosities.

APPENDIX

2.A. RELATIVE EFFECTS OF THE WHITE NOISE AND HARMONIC COMPONENTS OF VELOCITY PERTURBATION

In this appendix, we assess the effect of varying the strength of the imposed white-noise perturbations at nozzle exit on jet breakup. In figure 2.A.1, the Fourier transforms of the nozzle exit velocity are given. One can see that for amplitudes greater than 0.1%, the harmonic component is the main perturbation mechanism. The other frequency components imposed by the white noise would influence the time series of the instantaneous jet intact length.
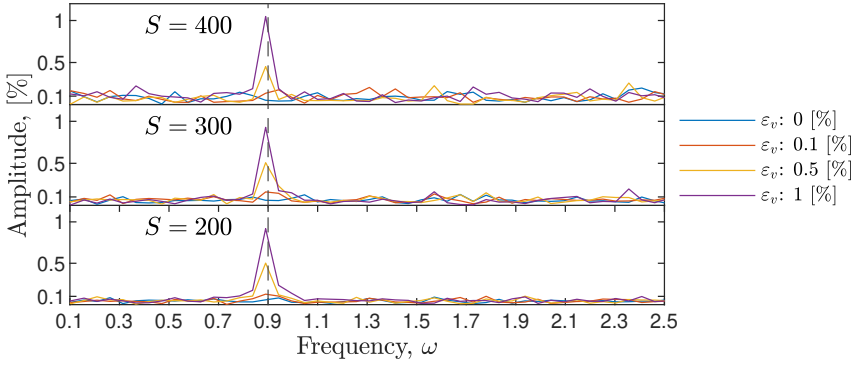
Figure 2.A.1: Frequency spectrum of the nozzle velocity $u(0, t)$ with respect to different amplitudes for the harmonic component and the noise component. The frequency of the harmonic component is $\omega = 0.9$.

Figure 2.A.2 shows the mean jet intact length with respect to the amplitude of the imposed harmonic component at different levels of white noise intensity. In the absence of the harmonic component, one can see that the fluctuations of the intact length are much stronger. This is partly due to the fact that there is a wider window of unstable wavelengths because of the streamwise component of the body force. The wavelengths that are initially not long enough and thus stable will eventually get stretched and fall into the instability window. When the amplitude of the harmonic component is weak, the frequencies within the white noise have more time to be stretched and interfere with the instability. When the amplitude of the harmonic component is strong, harmonic perturbation will dominate the dynamics, which can also be seen by narrowing of the errorbars at high amplitudes in figure 2.A.2.

2.B. OBTAINING $p(\theta)$

We use the fact that the convective growth rate can be expressed in terms of temporal growth rate given that we are above the critical wavenumber.

$$k_i(\xi) = \frac{\omega_{i,temp}(\xi)}{t_{IC}(\xi)U(\xi)} \tag{2.B.1}$$

The temporal growth rate can be deduced from the classical Rayleigh-Plateau instability as:

$$\omega_{i,temp}(\xi) = \frac{k}{\sqrt{2}}\sqrt{1 - k^2 + \frac{9Oh^2k^2}{2}} - \frac{3Ohk^2}{2} \tag{2.B.2}$$

where k is the local real wavenumber. The local values of k, Oh, t_{IC} and U are as
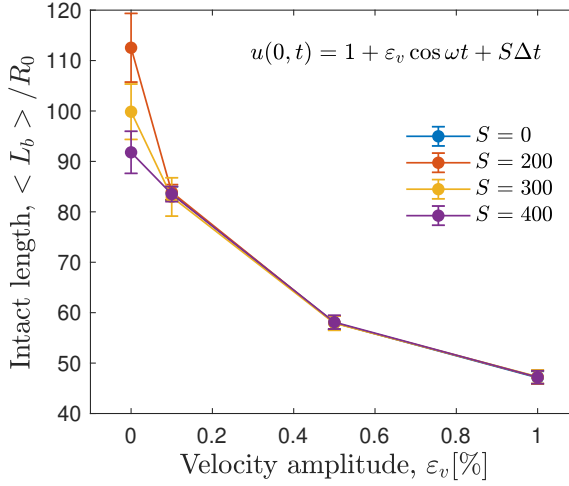
Figure 2.A.2: Variation of the jet intact length with respect to different strengths of harmonic and the white noise components. Here, the frequency of the harmonic component is $\omega = 0.9$ and Δt is the adaptive computational time step. The errorbars are one standard deviation of the intact length.

follows:

$$k(\xi) = \omega\xi^{-3/4}, \tag{2.B.3a}$$

$$Oh_l(\xi) = Oh\xi^{1/8}, \tag{2.B.3b}$$

$$t_{IC}(\xi) = \sqrt{We}\xi^{-3/8}, \tag{2.B.3c}$$

$$U(\xi) = \xi^{-1/2}. \tag{2.B.3d}$$

When we substitute these into (2.B.2) and use (2.B.1) to evaluate $k_i(\xi)$, we end up with:

$$k_i(\xi) = \frac{\omega}{\sqrt{2We}}\xi^{-7/8}\left(\sqrt{1 - \omega^2\xi^{-3/2} + \frac{9Oh^2\omega^2}{2}\xi^{-5/4}} - \frac{3Oh\omega}{\sqrt{2}}\xi^{-5/8}\right). \tag{2.B.4}$$

Using the transformations given in (2.32) and (2.33b), we finally obtain $p(\theta)$ explicitly as:

$$p(\theta) = \sqrt{\frac{1 - \theta^{-3/2}}{2} + \frac{9Oh^2\omega^{1/3}}{4}\theta^{-5/4}} - \frac{3Oh\omega^{1/6}}{2}\theta^{-5/8}. \tag{2.B.5}$$

When $p(\theta)$ can be explicitly integrated, (2.34) would then give an explicit equation to solve for θ_t:

$$S_t = \frac{s_0\omega^{7/6}}{\sqrt{We}}\left[P(\theta_t) - P(1)\right], \tag{2.B.6}$$

where $S_t \approx 7$ and $P(\theta) = \int p(\theta)d\theta$.

2.C. CHRISTOFFEL SYMBOLS, EXPRESSIONS IN LOCAL AND FRENET FRAMES

Here we provide the intermediate expressions to define the local coordinate system and the terms in the governing equations.

Using 2.9, one can represent the local base vectors in terms of the Frenet frame as follows:

$$
\begin{bmatrix} \mathbf{T} \\ \mathbf{N} \\ \mathbf{B} \end{bmatrix} = \begin{bmatrix} \frac{1}{1-r\kappa\cos\phi} & 0 & \frac{-\tau}{1-r\kappa\cos\phi} \\ 0 & \cos\phi & -\frac{\sin\phi}{r} \\ 0 & \sin\phi & \frac{\cos\phi}{r} \end{bmatrix} \begin{bmatrix} \mathbf{e}_1 \\ \mathbf{e}_2 \\ \mathbf{e}_3 \end{bmatrix}. \tag{2.C.1}
$$

As mentioned in §2.3.1 and seen in (2.11), the local base vectors are not necessarily unit. The magnitudes of the local base vectors should be used in order to express the physical velocity $\mathbf{u} = (u_s, u_r, u_\phi)$ vector from the contravariant vector $\mathbf{v} = (v^1, v^2, v^3)$ as follows:

$$
u_s = v^1 |\mathbf{e}_1| = v^1 \sqrt{(1 - r\kappa\cos\phi)^2 + (r\tau)^2}, \qquad u_r = v^2 |\mathbf{e}_2| = v^2, \qquad u_\phi = v^3 |\mathbf{e}_3| = v^3 r. \tag{2.C.2}
$$

The Christoffel symbols of the second kind, whose compact form is given in (2.14), can be written explicitly as follows:

$$
\left.
\begin{aligned}
&\Gamma_{11}^1 = \frac{r}{1 - r\kappa\cos\phi}\left(\kappa\tau\sin\phi - \cos\phi\frac{d\kappa}{ds}\right), \\
&\Gamma_{11}^2 = (1 - r\kappa\cos\phi)\kappa\cos\phi - r\tau^2, \\
&\Gamma_{11}^3 = \frac{r\tau}{1 - r\kappa\cos\phi}\left(\cos\phi\frac{d\kappa}{ds} - \kappa\tau\sin\phi\right) - (1 - r\kappa\cos\phi)\frac{\kappa\sin\phi}{r} + \frac{d\tau}{ds}, \\
&\Gamma_{22}^1 = \Gamma_{22}^2 = \Gamma_{22}^3 = 0, \qquad \Gamma_{23}^1 = \Gamma_{32}^1 = 0, \qquad \Gamma_{23}^2 = \Gamma_{32}^2 = 0, \\
&\Gamma_{33}^1 = \Gamma_{33}^3 = 0, \quad \Gamma_{33}^2 = -r, \qquad \Gamma_{23}^3 = \Gamma_{32}^3 = \frac{1}{r}, \\
&\Gamma_{12}^1 = \Gamma_{21}^1 = -\frac{\kappa\cos\phi}{1 - r\kappa\cos\phi}, \qquad \Gamma_{13}^1 = \Gamma_{31}^1 = \frac{r\kappa\sin\phi}{1 - r\kappa\cos\phi}, \\
&\Gamma_{12}^2 = \Gamma_{21}^2 = 0, \qquad \Gamma_{13}^2 = \Gamma_{31}^2 = -r\tau, \\
&\Gamma_{12}^3 = \Gamma_{21}^3 = \frac{\kappa\tau\cos\phi}{1 - r\kappa\cos\phi} + \frac{\tau}{r}, \qquad \Gamma_{13}^3 = \Gamma_{31}^3 = -\frac{r\kappa\tau\sin\phi}{1 - r\kappa\cos\phi}.
\end{aligned}
\right\} \tag{2.C.3}
$$

The covariant terms in the conservation equations can be written in the general coor-

dinates as follows:

$$\frac{D\mathbf{v}}{Dt} = \left(\frac{\partial v^i}{\partial t} + v^j\left(\frac{\partial v^i}{\partial s^j} + v^k \Gamma^i_{jk}\right)\right)\mathbf{e}_i, \tag{2.C.4a}$$

$$-\nabla p = g^{ij}\frac{\partial p}{\partial s^j}\mathbf{e}_i, \tag{2.C.4b}$$

$$(2\boldsymbol{D})^{ij} = g^{kj}\left(\frac{\partial v^i}{\partial s^k} + \Gamma^i_{kl}v^l\right) + g^{ki}\left(\frac{\partial v^j}{\partial s^k} + \Gamma^j_{kl}v^l\right), \tag{2.C.4c}$$

$$\frac{1}{Re}\nabla\cdot(2\boldsymbol{D}) = \frac{1}{Re}\left(\frac{1}{\sqrt{\Delta}}\frac{\partial}{\partial s^j}\left(\sqrt{\Delta}(2\boldsymbol{D})^{ij}\right) + \Gamma^i_{jk}(2\boldsymbol{D})^{ij}\right)\mathbf{e}_i. \tag{2.C.4d}$$

One can then use the metric tensor (and its inverse) and the Christoffel symbols listed in (2.11), (2.12) and (2.C.3) to compute the terms given above in (2.C.4a-2.C.4d). To compute the projections in the Frenet frame one can use the transformation given in (2.C.1).

2.D. BENCHMARK FOR THE SLENDER JET SIMULATION

We validate our slender jet model that includes the longitudinal projections of the computed body forces with the results of the arbitrary Lagrangian-Eulerian simulation presented in [19]. Their approach considers a boundary (a free parameter) between linear-nonlinear evolution of the perturbation and this boundary is validated by convergence of the breakup length over different choices of the linear-nonlinear boundary. Here we compare the case where this boundary is directly set at the nozzle exit, corresponding to Figure 3 in [19].
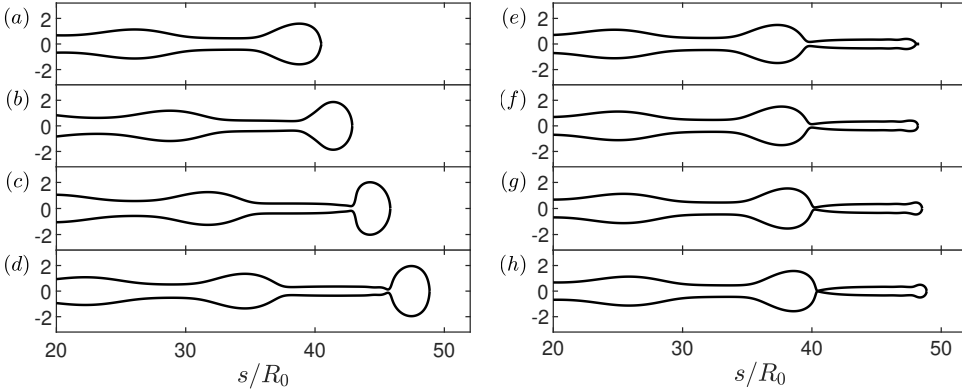
Figure 2.D.1: Jet shapes from our slender jet model for the parameters $We = 10$, $Fr = 5$, $Rb = 1$, $Re = 50$ and $\epsilon = 0.0172$, for one droplet generation cycle. $(a-d)$ correspond to $t = 0, 1.9, 3.9, 5.8$. $(e-h)$ correspond to $t = 7.6, 7.9, 8.1, 8.5$, where t is measured from the beginning of the cycle. The frequency and the amplitude of the radius perturbation are $\omega = 0.736$ and $\varepsilon_R = 0.04$. The results are in agreement the results of [19], Figure 3.

The pinch-off location of the main drop in both our simulations and in [19] is 46-48 times the radius of the jet and the period of the drop generation cycle is 8.5 in units of R_0/U_0, which corresponds to the period of the nozzle excitation $2\pi/\omega$.

2

REFERENCES

[1] Y. E. Kamis, S. Prakash, W.-P. Breugem, and H. B. Eral. "Controlling the breakup of spiralling jets: results from experiments, nonlinear simulations and linear stability analysis". In: *Journal of Fluid Mechanics* 956 (2023), A24.

[2] P. Mellado, H. A. McIlwee, M. R. Badrossamay, J. A. Goss, L. Mahadevan, and K. Kit Parker. "A simple model for nanofiber formation by rotary jet-spinning". In: *Applied Physics Letters* 99.20 (2011), p. 203107.

[3] H. B. Eral, E. R. Safai, B. Keshavarz, J. J. Kim, J. Lee, and P. S. Doyle. "Governing principles of alginate microparticle synthesis with centrifugal forces". In: *Langmuir* 32.28 (2016), pp. 7198–7209.

[4] K. Singh, A. Gupta, A.-J. Buchner, F. Ibis, J. W. Pronk, D. Tam, and H. B. Eral. "Analysis of centrifugal homogenization and its applications for emulsification & mechanical cell lysis". In: *Journal of Colloid and Interface Science* 547 (2019), pp. 127–135. ISSN: 0021-9797. DOI: https://doi.org/10.1016/j.jcis.2019.03.036. URL: https://www.sciencedirect.com/science/article/pii/S0021979719303261.

[5] Y. Li, G. M. Sisoev, and Y. D. Shikhmurzaev. "Spinning disk atomization: Theory of the ligament regime". In: *Physics of Fluids* 30.9 (2018), p. 092101.

[6] B. Keshavarz, E. C. Houze, J. R. Moore, M. R. Koerner, and G. H. McKinley. "Rotary atomization of Newtonian and viscoelastic liquids". In: *Physical Review Fluids* 5.3 (2020), p. 033601.

[7] S. P. Decent, A. C. King, and I. M. Wallwork. "Free jets spun from a prilling tower". In: *Journal of Engineering Mathematics* 42.3 (2002), pp. 265–282.

[8] S. N. Saleh, S. M. Ahmed, D. Al-mosuli, and S. Barghi. "Basic design methodology for a prilling tower". In: *The Canadian Journal of Chemical Engineering* 93.8 (2015), pp. 1403–1409.

[9] D. C. Y. Wong, M. J. H. Simmons, S. P. Decent, E. I. Părău, and A. C. King. "Break-up dynamics and drop size distributions created from spiralling liquid jets". In: *International Journal of Multiphase Flow* 30.5 (2004), pp. 499–520.

[10] L. Partridge, D. C. Y. Wong, M. J. H. Simmons, E. I. Părău, and S. P. Decent. "Experimental and theoretical description of the break-up of curved liquid jets in the prilling process". In: *Chemical Engineering Research and Design* 83.11 (2005), pp. 1267–1275.

[11] I. M. Wallwork, S. P. Decent, A. C. King, and R. M. S. M. Schulkes. "The trajectory and stability of a spiralling liquid jet. Part 1. Inviscid theory". In: *Journal of Fluid Mechanics* 459 (2002), pp. 43–65. DOI: 10.1017/S0022112002008108.

[12] E. I. Părău, S. P. Decent, M. J. H. Simmons, D. C. Y. Wong, and A. C. King. "Nonlinear viscous liquid jets from a rotating orifice". In: *Journal of Engineering Mathematics* 57.2 (2007), pp. 159–179.

[13] N. Marheineke and R. Wegener. "Asymptotic model for the dynamics of curved viscous fibres with surface tension". In: *Journal of Fluid Mechanics* 622 (2009), pp. 345–369.

[14] S. P. Decent, A. C. King, M. J. H. Simmons, E. I. Părău, I. M. Wallwork, C. J. Gurney, and J. Uddin. "The trajectory and stability of a spiralling liquid jet: Viscous theory". In: *Applied Mathematical Modelling* 33.12 (2009), pp. 4283–4302.

[15] J. Uddin, S. P. Decent, and M. J. H. Simmons. "The Instability of Shear Thinning and Shear Thickening Spiralling Liquid Jets: Linear Theory". In: *Journal of Fluids Engineering* 128.5 (Mar. 2006), pp. 968–975. ISSN: 0098-2202. DOI: 10.1115/1.2238876. URL: https://doi.org/10.1115/1.2238876.

[16] A. M. Alsharif, J. Uddin, and M. F. Afzaal. "Instability of viscoelastic curved liquid jets". In: *Applied Mathematical Modelling* 39.14 (2015), pp. 3924–3938.

[17] A. M. Alsharif and J. Uddin. "Instability of viscoelastic curved liquid jets with surfactants". In: *Journal of Non-Newtonian Fluid Mechanics* 216 (2015), pp. 1–12.

[18] Y. D. Shikhmurzaev and G. M. Sisoev. "Spiralling liquid jets: verifiable mathematical framework, trajectories and peristaltic waves". In: *Journal of Fluid Mechanics* 819 (2017), pp. 352–400.

[19] Y. Li, G. M. Sisoev, and Y. D. Shikhmurzaev. "On the breakup of spiralling liquid jets". In: *Journal of Fluid Mechanics* 862 (2019), pp. 364–384.

[20] S. Noroozi, W. Arne, R. G. Larson, and S. M. Taghavi. "A comprehensive mathematical model for nanofibre formation in centrifugal spinning methods". In: *Journal of Fluid Mechanics* 892 (2020).

[21] J. Eggers and T. F. Dupont. "Drop formation in a one-dimensional approximation of the Navier–Stokes equation". In: *Journal of Fluid Mechanics* 262 (1994), pp. 205–221.

[22] T. Driessen, P. Sleutel, F. Dijksman, R. Jeurissen, and D. Lohse. "Control of jet breakup by a superposition of two Rayleigh–Plateau-unstable modes". In: *Journal of Fluid Mechanics* 749 (2014), pp. 275–296.

[23] C. McIlroy and O. G. Harlen. "Effects of drive amplitude on continuous jet breakup". In: *Physics of Fluids* 31.6 (2019), p. 064104.

[24] D. S. Pillai, P. Narayanan, S. Pushpavanam, T. Sundararajan, A. Jasmin Sudha, and P. Chellapandi. "A nonlinear analysis of the effect of heat transfer on capillary jet instability". In: *Physics of Fluids* 24.12 (2012), p. 124106.

[25] Y. E. Kamis, H. B. Eral, and W.-P. Breugem. "Active control of jet breakup and droplet formation using temperature modulation". In: *Physical Review Fluids* 6.10 (2021), p. 103903.

[26] S. Tomotika. "Breaking up of a drop of viscous liquid immersed in another viscous fluid which is extending at a uniform rate". In: *Proceedings of the Royal Society of London. Series A-Mathematical and Physical Sciences* 153.879 (1936), pp. 302–318.

[27]   U. S. Sauter and H. W. Buggisch. "Stability of initially slow viscous jets driven by gravity". In: *Journal of Fluid Mechanics* 533 (2005), pp. 237–257.

[28]   A. Javadi, J. Eggers, D. Bonn, M. Habibi, and N. M. Ribe. "Delayed capillary breakup of falling viscous jets". In: *Physical Review Letters* 110.14 (2013), p. 144501.

[29]   S. Le Dizès and E. Villermaux. "Capillary jet breakup by noise amplification". In: *Journal of Fluid Mechanics* 810 (2017), pp. 281–306.

[30]   J. Eggers and E. Villermaux. "Physics of liquid jets". In: *Reports on Progress in Physics* 71.3 (2008), p. 036601.

[31]   P. Wesseling. *Principles of computational fluid dynamics*. Springer Science & Business Media, 2009.

[32]   A. Meurer, C. P. Smith, M. Paprocki, O. Čertík, S. B. Kirpichev, M. Rocklin, A. Kumar, S. Ivanov, J. K. Moore, S. Singh, T. Rathnayake, S. Vig, B. E. Granger, R. P. Muller, F. Bonazzi, H. Gupta, S. Vats, F. Johansson, F. Pedregosa, M. J. Curry, A. R. Terrel, Š. Roučka, A. Saboo, I. Fernando, S. Kulal, R. Cimrman, and A. Scopatz. "SymPy: symbolic computing in Python". In: *PeerJ Computer Science* 3 (Jan. 2017), e103. ISSN: 2376-5992. DOI: 10.7717/peerj-cs.103. URL: https://doi.org/10.7717/peerj-cs.103.

[33]   V. Entov and A. Yarin. "Influence of elastic stresses on the capillary breakup of jets of dilute polymer solutions". In: *Fluid Dynamics* 19.1 (1984), pp. 21–29.

[34]   B. Ambravaneswaran, E. D. Wilkes, and O. A. Basaran. "Drop formation from a capillary tube: Comparison of one-dimensional and two-dimensional analyses and occurrence of satellite drops". In: *Physics of Fluids* 14.8 (2002), pp. 2606–2621.

[35]   T. Driessen and R. Jeurissen. "A regularised one-dimensional drop formation and coalescence model using a total variation diminishing (TVD) scheme on a single Eulerian grid". In: *International Journal of Computational Fluid dynamics* 25.6 (2011), pp. 333–343.

[36]   W. T. Pimbley and H. C. Lee. "Satellite droplet formation in a liquid jet". In: *IBM Journal of Research and Development* 21.1 (1977), pp. 21–30.

[37]   J. U. Brackbill, D. B. Kothe, and C. Zemach. "A continuum method for modeling surface tension". In: *Journal of Computational Physics* 100.2 (1992), pp. 335–354.

[38]   C. Clanet and J. C. Lasheras. "Transition from dripping to jetting". In: *Journal of Fluid Mechanics* 383 (1999), pp. 307–326.

[39]   C. M. Bender and S. A. Orszag. *Advanced mathematical methods for scientists and engineers*. McGraw-Hill, 1978.

2

3

ACTIVE CONTROL OF JET BREAKUP AND DROPLET FORMATION USING TEMPERATURE MODULATION

We demonstrated the significance of a mechanism to induce Rayleigh-Plateau instability to control jet breakup. This could be by means of mechanical vibrations at a given frequency and amplitude, that would modulate the pressure and the velocity at the nozzle. For a large scale process such as prilling, however, it is worthwhile to investigate other means of perturbations. In this chapter, we numerically investigate the control of jet breakup using temperature modulation at the nozzle with a specified frequency and amplitude. Our results show that temperature modulation does lead to instability through capillary and Marangoni stresses, providing control of the droplet formation in terms of intact length and resultant drop size distribution, which is otherwise irregular due to inevitable presence of background noise. For understanding the mechanisms underpinning the breakup of a thermally modulated jet in the presence of noise, it is useful to decompose the surface tension forces into a contribution from curvature-gradient forces and a contribution from surface tension-gradient forces, associated with axial variations in the jet curvature and the temperature-dependent surface tension coefficient, respectively. We show that in the limit of slow axial heat diffusion and slow cooling to the ambient, as considered here, the breakup of a thermally modulated jet is governed by the ratio of the surface tension-gradient force to the imposed random perturbation force at nozzle exit. This so-called 'thermal modulation strength number' depends on the amplitude and frequency of the thermal modulation, the sensitivity of the surface tension coefficient to variations in temperature, the Weber number and the strength of the Gaussian white noise added to the nozzle exit velocity. We show that the thermal modulation strength number governs the shift in breakup characteristics from forward to rear pinch-off for increasing modulation

strength as well as the nature of the instability. When thermal modulation is weak, the surface tension gradient forces act only as a trigger and curvature-gradient forces soon take over and grow exponentially downstream the jet due to inertio-capillary growth. When thermal modulation is strong, the surface tension gradient forces not only act as a trigger, but remain significant till breakup. The thermal modulation strength number is thus useful to the design of thermal modulation in practical applications as a possible alternative to often used mechanical excitation mechanisms to control jet breakup.

3

3.1. INTRODUCTION

Controlling the formation of droplets from liquid jets is a fundamental challenge whose relevance spans applications at a wide variety of scales, from serial femtosecond X-ray crystallography[2, 3] where typical jet lengths are on the order of microns, to production of pharmaceuticals[4, 5] where it reaches a few tens of millimeters, and to prilling[6] where the jet lengths typically reach a few tens of centimeters. In all of these applications, understanding and controlling the breakup is essential. The resulting drop size distribution should be predictable, narrow and monodisperse. If not modulated, it is irregular with a wide distribution. Among aforementioned applications, control of droplet formation in prilling is particularly challenging and underexplored. Prilling, a commonly used method for production of fertilizers and polymers, is an industrial scale process involving break-up of molten polymeric jets and the crystallization of the droplets formed thereafter. From a fluid mechanics and rheology point of view, the challenge in prilling is to control the drop formation of a slender jet with rotational body forces, non-Newtonian effects and heat transfer.

The study of all processes involving jet breakup starts from the well-known Rayleigh-Plateau instability, which manifests itself as a competition of radii of curvatures on a cylindrical column of liquid. Rayleigh considered the temporal linear stability of an infinite jet in the inviscid limit [7, 8]. This was extended by Chandrasekhar by considering the viscous effects [9]. They showed that viscosity slows down the growth and increases the wavelength at which the growth is fastest. In a lab frame of reference, however, the instability grows in space as it is convected downstream. Keller et al. [10] have performed a spatial analysis, and showed that the spatial growth can be approximated by the temporal growth of disturbances on a single thread provided that the jet speed is sufficiently high, i.e. the downstream motion of a thread has to be much faster than the typical time of capillary growth so the jet can be regarded as infinite. Leib et al.[11] later extended this analysis by accounting for the viscous effects. These studies are from the standpoint of linear stability, where the effects of finite amplitude disturbances cannot be captured. The non-linear slender jet model[12–14], based on a Taylor expansion of the radial variable in the governing jet equations, provides a computationally efficient alternative to the linear stability analysis and can be used to cover the whole instability process till breakup. These studies concern a filament in a frame of reference moving with the jet velocity and track the nonlinear evolution using the 1D slender jet model. Eggers [12] and Papageorgiou [15, 16] considered the 1D slender jet model close to the breakup and came up with scaling relations to describe the thinning process analytically and showed that the pinchoff process is self-similar. Wilkes et al [17] implemented a 2D FEM algorithm to study the formation of droplets from a tube and in a follow-up study, Ambravaneswaran et al.[18] discuss the comparison between 1D and 2D models. The main limitation of the 1D model is the inability to capture the overturning of the interface profile very close to the pinchoff when the viscosity is low. However, concerning the balance of inertial, viscous and capillary forces, 1D slender jet model does an excellent job in capturing the nonlinear growth of disturbances in a computationally cheap manner.

When we think of methods to provide a periodic disturbance to a stream, the most commonly encountered methods in the literature are mechanical perturbations, which

either perturb the upstream pressure [19] or the orifice of the jet using concentric piezo elements [20, 21]. These mechanical perturbations manifest themselves as changes in the local curvature, thus changes in the local Laplace pressure, which leads to instabilities while being advected downstream. A possible alternative to mechanical excitation of the jet is advocated here, which is through thermal modulation of the temperature-dependent surface tension coefficient. Next to perturbations in the capillary stress (Laplace pressure) this also results in in an additional stress compared to mechanical excitation: the Marangoni stress related to axial variations in the temperature-dependent surface tension coefficient [22].

The growth of infinitesimal perturbations on nonisothermal jets with thermocapillarity has been studied both analytically and numerically. Xu&Davis[23], performed a linear stability analysis on an infinitely long liquid cylinder subject to a linear temperature gradient. They found that in the limit of high thermal diffusivity and high heat transfer to the ambient, the disturbances vanish and the jet remains stable. Kuhlmann et al.[24] studied the temporal stability of a liquid bridge bounded by disks at different temperatures and derived marginal stability curves for the critical temperature gradient that would lead to instability. Mashayek et al.[25], considered nonlinear effects on a nonisothermal thread. Considering a spatially periodic ambient temperature, they identify the critical Biot number at which flows due to capillary pressure and Marangoni stresses cancel out exactly and a stable jet is obtained (i.e. marginal stability). They also study thermal disturbances on the jet surface both with and without surface disturbances. When only thermal disturbances are considered, they report a Marangoni instability and did not observe thermal-capillary instability. Gao et al.[26], studied the effect of imposed surface tension modulation on a non-Newtonian jet with a Carreau-Yasuda model using slender jet formulation. Their study does not include the energy conservation, so the relaxation time of the variations of surface tension cannot be captured. Pillai et al.[27] were the first to come up with the nonisothermal slender jet equations. They studied velocity modulations on a slender jet with temperature-dependent surface tension and viscosity, and subject to cooling. Faidley et al.[28], carried out the first experiments to test the idea of thermal modulation at the nozzle. They reported agreement with Rayleigh's dispersion relation for an isothermal jet. However, at very high and low wavenumbers the background noise dominated over the colored perturbations since the growth rate at both limits are very low. The idea of using thermally induced perturbations to control jet breakup drew attention in studies of continuous ink jet printing as well [29]. Heating elements at the inlet have also been studied and utilized for alternative purposes as well. Chwalek et al.[30] used asymmetric heating at the nozzle inlet as a method to deflect microjets. Suryo et al.[31] numerically studied a pendant drop and demonstrated that dripping can occur even in the absence of gravity by means of a line heater located at the inlet.

Nonisothermal jet breakup bears many analogies with surfactant-laden jet breakup. The presence of Marangoni stress in this case is due to the variation of surfactant concentration on the jet interface that gives rise to gradients in the surface tension coefficient. Ambravaneswaran et al. [32] extended the 1D slender jet equations in the presence of soluble surfactants to consider the effect of Marangoni stress on the evolution of instabilities. Kamat et al. [33] showed that the presence of surfactants may give rise

to formation of a sequence of microthreads close to the pinchoff which is not seen in surfactant-free threads. Wee et al. [34] considered a viscous thread in the presence of surfactants and derived a scaling relation that would make it possible to measure the surface viscosity of a surfactant-laden drop by using the temporal evolution of the neck thickness.

An analysis of the spatial development and non-linear breakup of a temperature-modulated jet has not been reported yet in literature. To this purpose we have employed the slender-jet model in the present study. Our objective is to gain insight in the underlying physical mechanisms responsible for the initiation and breakup of a straight and Newtonian jet that is thermally modulated at nozzle exit. We developed a 1D model within the framework of a slender-jet approximation and studied the nonlinear spatial instabilities due to the thermal modulation. The selected parameter space is motivated by typical conditions in prilling applications. We studied the effects of the thermal modulation characteristics (frequency and amplitude) as well as the thermal sensitivity of the surface tension coefficient on breakup and the droplet size distribution.

3
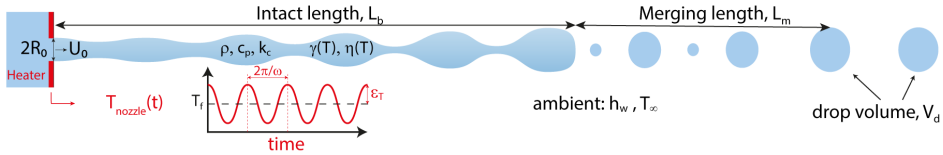
Figure 3.1: Illustration of the temperature-controlled jet breakup where the temperature at the nozzle, T_{nozzle}, is modulated to perturb the capillary stress, $\gamma(T)\kappa$ and the Marangoni stress, $\nabla_s \gamma$.

3.2. Mathematical Background

The mass conservation, Cauchy momentum and energy equations for the case described in Figure 3.1 are as follows:

$$\nabla \cdot \mathbf{v} = 0 \tag{3.1a}$$

$$\rho \left(\frac{\partial \mathbf{v}}{\partial t} + (\mathbf{v} \cdot \nabla)\mathbf{v} \right) = \nabla \cdot \sigma \tag{3.1b}$$

$$\rho c_p \left(\frac{\partial T}{\partial t} + (\mathbf{v} \cdot \nabla) T \right) = k_c \nabla^2 T \tag{3.1c}$$

where the total stress tensor for a Newtonian fluid is defined as $\sigma = -p\mathbf{I} + 2\eta(T)\mathbf{D}$ and $2\mathbf{D} = \nabla\mathbf{v} + (\nabla\mathbf{v})^T$. Here, ρ, c_p and k_c represent the density, specific heat capacity and the thermal conductivity of the liquid, respectively.

On the free surface one has the continuity of normal and tangential stresses, i.e. the dynamic boundary condition:

$$\sigma \cdot \mathbf{n} = -\gamma(T)\kappa\mathbf{n} + \nabla_s \gamma(T) \tag{3.2}$$

where **n** is the outward unit normal, $\nabla_s = (\boldsymbol{I} - \mathbf{nn}) \cdot \nabla$ is the surface gradient operator and $\kappa = \nabla_s \cdot \mathbf{n}$ is the curvature of the free surface, respectively. The constitutive relations for temperature-dependent surface tension and viscosity are approximated as:

$$\gamma(T) = \gamma_0 - \beta(T - T_m) \tag{3.3a}$$

$$\eta(T) = \eta_0 \exp(-\alpha(T - T_m)) \tag{3.3b}$$

where β [N m^{-1} K^{-1}] is the first order temperature dependency of surface tension (i.e. $d\gamma/dT = -\beta$) and α [K^{-1}] is a positive constant representing how rapidly viscosity changes with temperature.

In addition to the dynamic boundary condition, one has the kinematic boundary condition of the jet interface at $r = R(z, t)$ moving with the local radial velocity:

$$\frac{\partial R}{\partial t} + v \frac{\partial R}{\partial z} = u|_{r=R(z,t)} \tag{3.4}$$

And finally, one has the heat transfer at the interface, given by:

$$-k_c \mathbf{n} \cdot \nabla T = h_w (T - T_\infty) \tag{3.5}$$

where h_w is the heat transfer coefficient between the liquid jet and the ambient which is at a temperature of T_∞.

Here we adopt the slender jet approximation for an axisymmetric jet [13], in which it is assumed that the radial variations are much weaker than axial variations in the velocity, pressure and temperature. This forms the basis for a Taylor series expansion of the flow variables in r:

$$\begin{aligned}
v(z, r, t) &= v_0(z, t) + v_2(z, t) r^2 + \dots, \\
u(z, r, t) &= -\frac{1}{2} v_0'(z, t) r - \frac{1}{4} v_2'(z, t) r^3 - \dots, \\
p(z, r, t) &= p_0(z, t) + p_2(z, t) r^2 + \dots, \\
T(z, r, t) &= T_0(z, t) + T_2(z, t) r^2 + \dots,
\end{aligned} \tag{3.6}$$

where primes denote $\partial/\partial z$. Inserting (3.6) in (3.1)-(3.5), and keeping only the terms that are leading order in r will yield the non-isothermal slender jet equations

$$\frac{\partial R^2}{\partial t} + (vR^2)' = 0 \tag{3.7a}$$

$$\rho \left(\frac{\partial v}{\partial t} + v v' \right) = -(\gamma(T)\kappa)' + \frac{\partial \gamma}{\partial T} T' \frac{2}{R} + 3\eta(T) \frac{(v'R^2)'}{R^2} + 3 \frac{\partial \eta}{\partial T} T' v' \tag{3.7b}$$

$$\rho c_p \left(\frac{\partial T}{\partial t} + v T' \right) = k_c \left(T'' + \frac{2T'R'}{R} - \frac{2h_w(T - T_\infty)}{k_c R} \right) \tag{3.7c}$$

where κ is the curvature given by:

$$\kappa = \frac{1}{\sqrt{1 + R'^2}} \left(\frac{1}{R} - \frac{R''}{1 + R'^2} \right) \tag{3.8}$$

Some details of the derivation regarding the interface conditions are discussed in Appendix 3.A.

The problem at hand is a multiphysics problem where capillary, thermocapillary, inertial, convective and diffusive (both for momentum and energy) events take place simultaneously. So it is convenient to list the relevant timescales that results from the balance of these events before nondimensionalization:

$$t_{IC} = \sqrt{\frac{\rho R_0^3}{\gamma_0}} = \text{Inertio-capillary time scale}$$

$$t_{ITC} = \sqrt{\frac{\rho R_0^3}{\beta \Delta T}} = \text{Inertio-thermocapillary time scale}$$

$$t_{VC} = \frac{\eta_0 R_0}{\gamma_0} = \text{Visco-capillary time scale}$$

$$t_A = \frac{R_0}{U_0} = \text{Advection time scale} \tag{3.9}$$

$$t_{TVC} = \frac{\alpha \Delta T \eta_0 R_0}{\gamma_0} = \text{Thermo-visco-capillary timescale}$$

$$t_{TD} = \frac{R_0^2 \rho c_p}{k_c} = \text{Thermal diffusive time scale}$$

$$t_{TC} = \frac{\rho c_p R_0}{h_w} = \text{Thermal cooling time scale}$$

These seven timescales will yield six nondimensional numbers, namely:

$$We = \frac{t_{IC}^2}{t_A^2}, \quad Ca = \frac{t_{VC}}{t_A}, \quad Pe = \frac{t_{TD}}{t_A}$$

$$Bi = \frac{t_{TD}}{t_{TC}}, \quad \Pi_\gamma = \frac{t_{IC}^2}{t_{ITC}^2}, \quad \Pi_\eta = \frac{t_{TVC}}{t_{VC}} \tag{3.10}$$

To make the system nondimensional, all spatial variables are expressed in units of R_0, all velocities in units of U_0, so nondimensional time is expressed in units of advection time $t_A = R_0/U_0$. The characteristic stress is given by capillary stress, γ_0/R_0, and the nondimensional temperature is expressed as:

$$\Theta(z, t) = \frac{T(z, t) - T_m}{\Delta T} \tag{3.11}$$

with $\Delta T = T_f - T_m$, where T_m is the melting point of the molten jet and T_f is the feed temperature of the jet. Hence, $\Theta = 0$ at the melting point, $\Theta = 1$ at the feed temperature, which is also the inlet temperature and finally $\Theta = \Theta_\infty < 0$ for the ambient temperature. Using these characteristics and with the definitions of the nondimensional numbers given in (3.10), the nondimensional set of governing equations are as follows:

$$\frac{\partial R^2}{\partial t} + \frac{\partial v R^2}{\partial z} = 0 \tag{3.12a}$$

$$\frac{\partial \nu R^2}{\partial t} + \frac{\partial \nu^2 R^2}{\partial z} = \frac{1}{We}\frac{\partial}{\partial z}\left(R^2(\tau_\gamma + \tau_\eta)\right) - \frac{\Pi_\gamma 2R}{We}\left(1 - \frac{1}{\sqrt{1+R'^2}}\right)\frac{\partial \Theta}{\partial z} \qquad (3.12b)$$

$$\frac{\partial R^2\Theta}{\partial t} + \frac{\partial(\nu R^2\Theta)}{\partial z} = \frac{1}{Pe}\frac{\partial}{\partial z}\left(R^2\frac{\partial \Theta}{\partial z}\right) - \frac{2BiR}{Pe}(\Theta - \Theta_\infty) \qquad (3.12c)$$

where τ_γ and τ_η are the capillary and viscous stresses integrated over the cross-sectional area, given by:

$$\tau_\gamma = \gamma(\Theta)K \quad \tau_\eta = 3Ca\eta(\Theta)\frac{\partial \nu}{\partial z}$$

$$K = \frac{1}{\sqrt{1+R'^2}}\left(\frac{1}{R} + \frac{R''}{1+R'^2}\right)$$

Finally, the nondimensional form of the temperature dependent material properties become:

$$\gamma(\Theta) = 1 - \Pi_\gamma\Theta \qquad (3.13a)$$

$$\eta(\Theta) = \exp\left(-\alpha\Delta T\Theta\right) \qquad (3.13b)$$

The resulting system of 1D unsteady equations (3.12) and (3.13) are solved for the conserved variables R^2, νR^2 and ΘR^2. We use a finite-difference scheme on a staggered grid where the jet cross section and the temperatures are stored in cell centers, and the velocities are stored on cell faces, as shown in Fig. 3.2. The jet domain spans $z \in [0, L]$ where
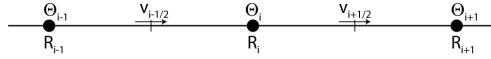

Figure 3.2: A schematic of the staggered grid

$L = 300R_0$, with the following initial and boundary conditions:

$$R^2(0, t) = 1 \qquad \nu R^2(0, t) = 1 + W(t)$$
$$\Theta R^2(0, t) = 1 + \varepsilon_T \sin\omega t \qquad (3.14)$$
$$R^2(z, 0) = \nu R^2(z, 0) = \Theta R^2(z, 0) = 1$$

where $W(t)$ is a Gaussian white noise term added on the jet velocity, which is described in Sec.3.3.1. ε_T and ω represent the amplitude and the frequency of the temperature modulation at the inlet. On the downstream end of the domain, convective open boundary condition is used[35]. The time integration is done explicitly by a 3-step Runge-Kutta scheme with adaptive time stepping. Except for velocities, a central differencing scheme is used for evaluating the variables at their half step neighbors, but for velocities a higher order total variation diminishing (TVD) van Leer scheme is used [36]. The singularity at pinch-off is regularised in a similar fashion described in [37], so that the drop formation and merging phenomena can also be accounted for. In this scheme, a sufficiently small (on the order of the grid size) cutoff radius, R_c, is selected beyond which the jet does not thin further. Its effects vanish with smaller grid size. Grid independence studies were carried out and we validated that the regularization does not affect the breakup

time nor the dynamics of the droplets that are formed. In figures that show the jet shape (Figures 3.4 and 3.7), only the parts where $R > R_c$ are shown to avoid confusion with the beads-on-a-string structure seen in viscoelastic liquids [38].

In Appendix 3.B, we briefly discuss some benchmark studies using our code with respect to 1D and 2D-axisymmetric cases from the literature.

3.3. Results and Discussion

3.3.1. Natural breakup of a nonisothermal jet under cooling

The fate of an uncontrolled jet is an challenging topic on its own and has been addressed experimentally and theoretically[39–41]. In their recent work, Ganan-Calvo et al.[40] propose a universal scaling law from a time-averaged energy balance of the steady flow of an isothermal jet and the perturbations thereon, and use experiments and simulations to determine the universal fitting constants. In the framework of the slender jet approximation, an isothermal jet will remain stable (provided that external body forces are negligible and $We > We_c$) if no perturbation is numerically imposed. So to set the reference case of an uncontrolled jet, we consider a jet with a Gaussian white noise added on top of the nozzle exit velocity, as shown in Fig.3.3, with a standard deviation of $A\Delta t$ where A is a free parameter to set the strength of the noise. So the forcing (per unit volume) by the random velocity fluctuation at the nozzle scales as $\rho(\partial v/\partial t)_{noz} \sim \rho U_0^2 A/R_0$ in dimensional units. This way of implementing the random noise makes sure that the forcing that results from the random fluctuations are uncorrelated with the time discretizations as desired. The strength parameter A is adjusted such that the intact length is in agreement with the experimental scaling law for the natural breakup of Newtonian jets[40] and fixed at a value of $A = 40$ in all of the simulations.
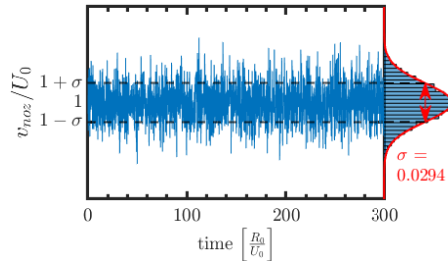
Figure 3.3: Random velocity fluctuations imposed at the nozzle, the standard deviation σ scales with $A\Delta t$ where Δt is the adaptive time step and A is a free constant that adjusts the strength of the fluctuation

In the presence of ambient cooling, the stationary profiles of temperature and the radius of the jet will also be nonuniform. If the cooling rate is strong enough, the Marangoni stresses due to the base state temperature profile will significantly accelerate the jet and lead to breakup (even without background noise), analogous to gravity driven jets[42].

In the absence of the temperature modulation at the inlet, the jet is only perturbed by the white noise, that is, the random velocity fluctuations at the inlet. This means the

perturbation has a spectrum of frequencies without a dominant amplitude at any frequency, so the breakup will consist of various frequencies superposed onto each other. The result is an irregular variation of the jet intact length, which is the distance from the inlet to the point of the first breakup. Figure 3.4 shows the variation of the intact length over time for a jet that is only perturbed by the white noise (from here on referred to as the reference case).

3.3.2. TEMPERATURE MODULATION AT THE INLET

The metrics of the control of jet breakup and droplet formation can be described in two facets: 1) Controlling the intact length, hence controlling where the droplet formation takes place and 2) controlling the mean and the spread of the drop size distribution. The choices of the nondimensional numbers in our simulations are motivated by typical conditions for a molten urea jet in a prilling process [6, 43], which are listed in Table 3.1. Based on this we fixed 5 of the 6 nondimensional numbers given in (3.10): $We = 50$,

Table 3.1: Fluid properties for molten urea[43] and the operating conditions for a typical prilling process[6] used in the simulations

Fluid properties, Urea @ 135 °C	
Melting point	$T_m \approx 133\,°\text{C}$
Density	$\rho \approx 1247\,\text{kg}\,\text{m}^{-3}$
Dynamic viscosity	$\eta_0 \approx 3\,\text{mPa}\,\text{s}$
Surface tension	$\gamma_0 \approx 66\,\text{mN}\,\text{m}^{-1}$
Specific heat capacity	$c_p \approx 2.25\,\text{kJ}\,\text{kg}^{-1}\,\text{K}^{-1}$
Thermal conductivity	$k_c \approx 1.2\,\text{W}\,\text{m}^{-1}\,\text{K}^{-1}$
Thermal sensitivity of viscosity	$\alpha \approx 0.02\,\text{K}^{-1}$
Typical process conditions	
Orifice radius	$R_0 \approx 700\,\mu\text{m}$
Jet velocity	$U_0 \approx 1\,\text{m}\,\text{s}^{-1}$
Feed temperature	$T_f \approx 145\,°\text{C}$
Ambient temperature	$T_\infty > 25\,°\text{C}$
Heat transfer coefficient	$h_w \approx 0.86\,\text{W}\,\text{m}^{-2}\,\text{K}^{-1}$

$Ca = 0.21$, $Pe = 1320$, $Bi = 0.5$ and $\Pi_\eta = 0.1$ as well as $\Theta_\infty = -4$ in all of our simulations. We varied Π_γ, i.e. the nondimensional form of the temperature sensitivity of the surface tension coefficient, between $\Pi_\gamma \in [0.005, 0.5]$ (with a typical value of 0.5 for urea). Furthermore, we also studied $\varepsilon_T \in [0.005, 0.5]$ as modulation amplitude and $\omega \in [0.1, 1.2]$ as modulation frequency, respectively.

Figure 3.4 lays out an overall comparison between the reference case which has no temperature modulation and a modulated case with $\varepsilon_T = 0.05$, $\omega = 0.7$ and $\Pi_\gamma = 0.05$. It shows that when a temperature modulation is introduced on top of the noise, the time series for the intact length changes significantly, where the intact length is defined as the length measured from nozzle exit over which the jet remains intact (see Fig. 3.1).
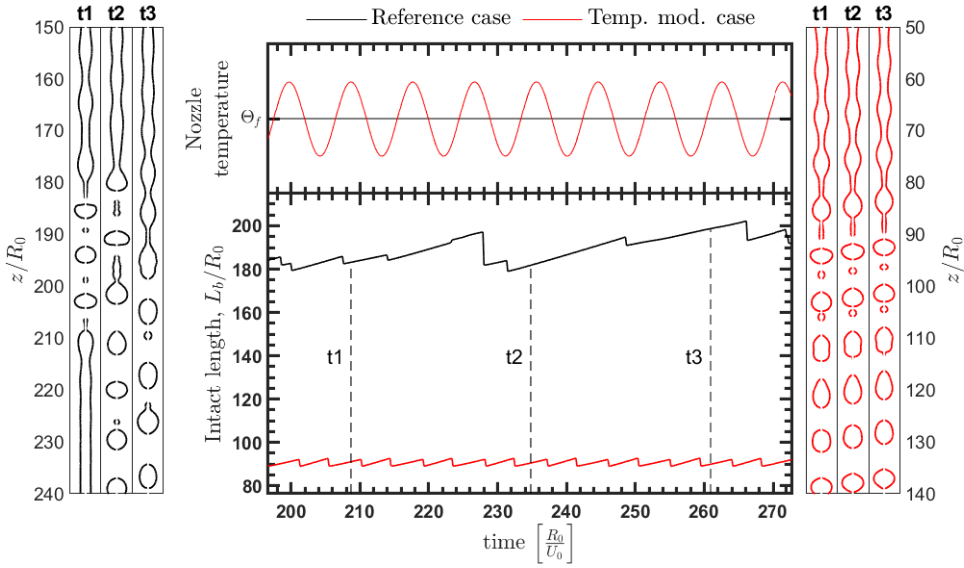
Figure 3.4: A comparison of the isothermal reference case (black) and a temperature modulated case (red) for $\varepsilon_T = 0.05$, $\Pi_\gamma = 0.05$ and $\omega = 0.7$. Parts of the jet where $R < R_c$ are not shown to avoid confusion with the beads-on-a-string structure seen in viscoelastic liquids.

The mean intact length gets shorter and the irregularity due to the noise is suppressed, thanks to the finite amplitude perturbation that is imposed. The variance of the intact length of the temperature modulated jet shows more of a periodic trend. When we look at the shape of the jet at several instants, they show recurrence, hence better control in terms of predictability of the location of the generated droplet stream.

Table 3.2: Average drop volumes with respect to the frequency of perturbation at the inlet. The model parameters are $\varepsilon_T = 0.05$ and $\Pi_\gamma = 0.05$.

Average drop volumes, normalized by R_0^3		
Frequency at the inlet ω	Avg. drop volume $< V_d >$	Volume of a single thread $\pi R_0^2 \lambda \approx \pi R_0^2 U_0 \frac{2\pi}{\omega}$
0.1	29.05	197.4
0.7	27.57	28.20
0.9	21.01	21.93
1.2	17.23	16.45

Figure 3.5 shows how the intact length changes with respect to the modulation frequencies. The results are in agreement with the presented results of nonlinear temporal
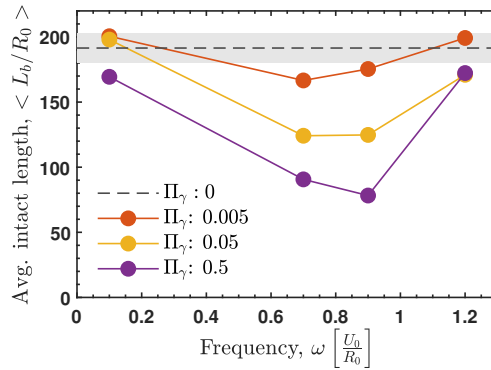
Figure 3.5: The intact length as a function of modulation frequency and Π_γ, the temperature modulation amplitude is fixed at $\varepsilon_T = 0.05$. The gray shaded region covers one standard deviation above and below the mean intact length for the reference case (i.e. $\Pi_\gamma = 0$)

analysis of a nonisothermal thread[25], since the Weber number in the simulations here is above the critical Weber number[10, 11]. The frequency at which the fastest growth takes place (i.e. shortest L_b) increases slightly with increasing Π_γ.
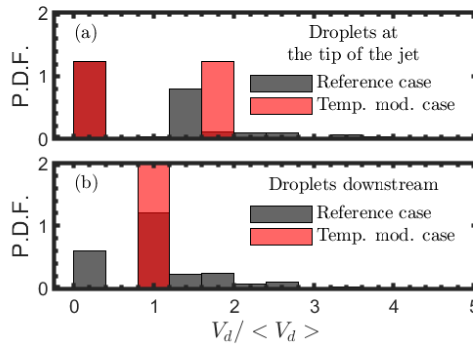
Figure 3.6: Comparison of the drop size distributions of the isothermal reference case and temperature modulated case shown in Fig. 3.4. (a) at the tip of the intact jet, $z = L_b$, and (b) downstream, $z = 280R_0$. The parameters for the perturbed case are $\varepsilon_T = 0.5$, $\omega = 0.7$ and $\Pi_\gamma = 0.05$.

A more quantitative comparison of the drops generated from the two cases can be obtained from Fig. 3.6. Each of the sharp drop in the intact length seen in Fig.3.4 represents a droplet that is generated at the tip of the jet. For the temperature modulated case, the size distribution of the droplets generated at the tip of the stream is bimodal, namely there is a periodic generation of a main droplet followed by a satellite droplet whose volume ratio is governed by the perturbation frequency. The satellite and the main drops merge after a certain distance downstream from the point where they are generated, as

shown in Fig. 3.4. Whether the satellite drops merge with the main drop that precedes or succeeds it depends on the location of the pinch-off within a single filament[44, 45]. The changes in the average drop sizes with respect to the frequency of modulation at the inlet is given in Table 3.2. Note that thermal modulation is not sufficiently strong to control jet breakup at the lowest frequency ($\omega = 0.1$), which is also evident from Fig. 3.5; the modulation is overwhelmed here by the presence of noise.
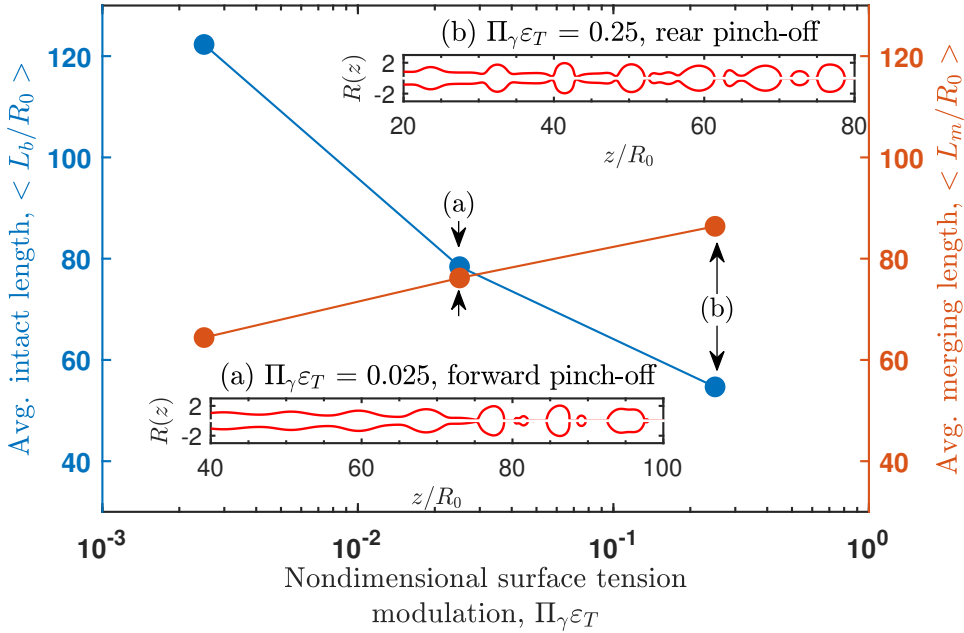
Figure 3.7: Average intact and merging lengths of the jet with respect to the modulation on the surface tension coefficient for $\omega = 0.7$. Insets show the two cases where the pinch-off characteristic shifts from a) forward pinch-off to b) rear pinch-off.

For isothermal jets, the shift in the pinch-off character is dependant on the amplitude of the modulation where the rear pinch-off only occurs in a narrow window of amplitudes[45]. In the case studied here, the modulation comes from a superposition of temperature modulation and random velocity fluctuations at nozzle exit. The temperature modulation is coupled to the liquid through the nondimensional number, Π_γ, which measures the sensitivity of surface tension to changes in temperature. Fig. 3.7 shows the variation of the time-averaged intact length and merging length of the jet. The merging length is defined from the tip of the jet where $z = L_b$ to the point where uniform droplets are formed ($z = L_b + L_m$) as shown in Fig. 3.1. As expected, for stronger modulations on the surface tension coefficient (i.e. higher $\Pi_\gamma \varepsilon_T$), the average intact length decays. The pinch-off character also shifts from forward to rear pinching.

For gaining physical understanding, it is useful to identify the important forces and how they scale. The case studied here is motivated by a typical process, where $Pe = 1320$

and $Bi = 0.5$ are fixed parameters. The large Pe and small Bi suggest that diffusion of heat within the jet and loss of heat to the ambient are negligible (though they are included in the computations). So the problem can be narrowed down to the competition of forcing due to background noise, $f_{bg} \sim \rho \, (\partial v / \partial z)_{noz} \sim \rho U_0^2 A / R_0$ and forcing due to temperature modulation, $f_{tm} \sim (1/R_0) \left(\partial \gamma / \partial z \right)_{noz} \sim \Pi_\gamma \varepsilon_T \omega \gamma_0 / R_0^2$. Their ratio can be written as a non-dimensional 'thermal modulation strength number', $\mathcal{M}$, defined as

$$\mathcal{M} = \frac{f_{tm}}{f_{bg}} \sim \frac{\Pi_\gamma \varepsilon_T}{We} \frac{\omega}{A} \tag{3.15}$$

This also explains the discrepancy between the average drop volume and the volume of a single thread for the low frequency in Table 3.2. Except for $\omega = 0.1$, the frequency of temperature modulation dictates the average drop volumes but in the case $\omega = 0.1$, the instability due to temperature modulation grows slower than that of background noise and the average drop size is dictated by the random background noise, which is closer to the value that is obtained at the fastest growing frequency.

The modulation in temperature yields 2 disturbance mechanisms that are out of phase with each other. The first one is due to the local change in surface tension coefficient, which manifests itself as an axial variation in the capillary pressure. Cold regions correspond to a higher surface tension coefficient and hence a higher capillary pressure at similar curvature, which thus tends to drive the flow from cold to hot regions. The second one originates from the gradient of surface tension coefficient along the jet, which gives rise to Marangoni stresses that drive the flow from regions of low to high surface tension coefficient, i.e. from hot to cold regions. The surface tension forces in the flow, f_{st}, can be grouped as follows

$$f_{st} = \underbrace{-\gamma \frac{\partial \kappa}{\partial z}}_{\substack{\text{curvature} \\ \text{gradient}}} + \underbrace{(\frac{2}{R} - \kappa) \frac{\partial \gamma}{\partial z}}_{\substack{\text{surface tension} \\ \text{gradient}}} \tag{3.16}$$

If there is no surface perturbation initially, the gradient of the curvature is zero and the forcing comes only from the terms related to the gradient of the surface tension coefficient (second term on the RHS of Eq. (3.16)). The magnitude of the force is higher for higher $\Pi_\gamma \varepsilon_T \omega$ (see Eq. (3.15)), which is the amplitude of the stress perturbations, given in Fig.3.8. This is the reason for the shift in pinch-off character shown in Fig.3.7, namely, even though the amplitudes of temperature modulation at the nozzle are identical for both cases, the amplitudes of the corresponding stress perturbations are an order of magnitude different due to the different Π_γ values.

This stress variation with a magnitude of $\Pi_\gamma \varepsilon_T \omega$ leads to surface variations later downstream, then a combination of capillary and Marangoni stresses act on the jet. In the cases where heat diffusion is also significant (i.e. low Peclet number), for instance with liquid metal jets, the temperature will tend to unify along the jet and the gradient of the surface tension coefficient would disappear, making the curvature effects the only driving force for the instability. The case studied here is at a high Peclet number, so the disturbances due to temperature gradient remain finite. Their significance with respect to the capillary growth depends on the value of $\Pi_\gamma \varepsilon_T$ (for fixed We, A and ω). From Fig.
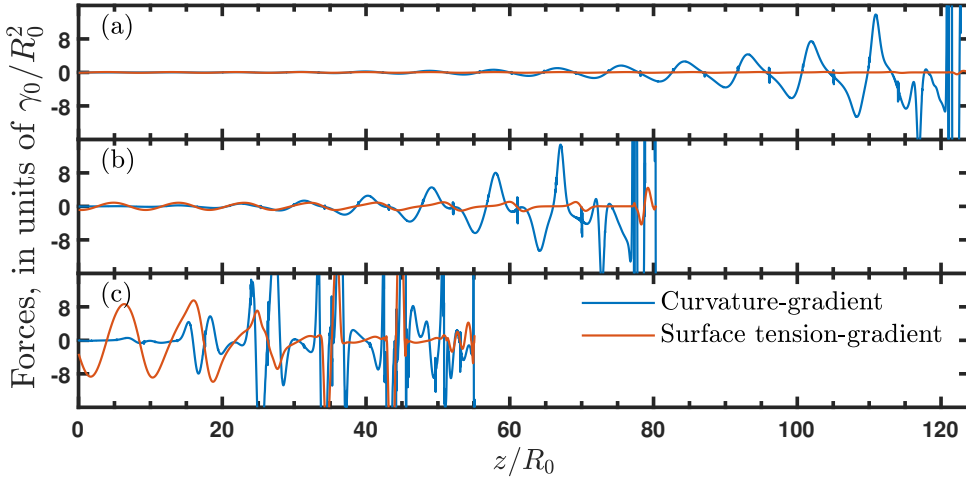
Figure 3.8: Growth of the stress perturbations for different surface tension sensitivities, (a) $\Pi_\gamma \varepsilon_T = 0.0025$ (b) $\Pi_\gamma \varepsilon_T = 0.025$ (c) $\Pi_\gamma \varepsilon_T = 0.25$. The modulation frequency, ω is fixed at 0.7

3.8, one can identify three different regimes. When $\Pi_\gamma \varepsilon_T$ is low (in Fig. 3.8a), the background noise is in charge of the instability that leads to breakup and the amplitude of the curvature-gradient forces grows exponentially. With a moderate value of $\Pi_\gamma \varepsilon_T$ (in Fig. 3.8b) the temperature modulation acts as a finite amplitude disturbance to initiate the capillary breakup, in other words it triggers the capillary breakup of the jet with a shorter intact length. The curvature forces start to grow close to the nozzle with a phase difference with respect to the surface tension gradient forces, then take over the process and grow exponentially. And finally at high values of $\Pi_\gamma \varepsilon_T$ (in Fig.3.8c) the surface tension-gradient forces are hindering the exponential growth of curvature forces and remain on the same order of magnitude until the breakup, which is even shorter due to the higher amplitude of forcing at the nozzle.

3.4. CONCLUSION

We numerically demonstrate that modulating the inlet temperature of straight jets can be used for controlling the breakup and formation of the droplets. The temperature modulation manifests itself as local perturbations in thermally-induced capillary and Marangoni stresses. For deeper physical understanding we proposed to decompose the surface tension forces into a contribution from curvature-gradient and surface tension gradient forces. The ratio of the surface-tension-gradient force to the imposed random perturbation force at nozzle exit can be expressed by the so-called thermal modulation strength number, $\mathcal{M}$. This number depends on the amplitude and frequency of the thermal modulation and the sensitivity of surface tension to variations in temperature on the one hand, and the Weber number and noise amplitude in the nozzle exit velocity on the other hand, as expressed by Equation 3.15. Larger values of the thermal mod-

ulation strength number provide a better control, shorter intact lengths and more uniform droplet streams. Correspondingly, with increasing modulation strength, the role of thermal modulation shifts from being only a trigger for exponential growth of curvature-gradient forces to the case where both curvature-gradient and surface tension gradient forces are dominant until pinch-off. The thermal modulation strength number is thus a useful criterion to the design of thermal modulation for controlled jet breakup in practice, in particular for determining the minimal required thermal modulation strength for generating a uniform droplet stream. Natural extensions of the present work are case studies of thermal modulation in the presence of non-negligible axial heat conduction and/or cooling to the ambient.

APPENDIX

3.A. A NOTE ON THE DERIVATION OF THE SLENDER-JET MODEL IN THE PRESENCE OF MARANGONI STRESSES AND AMBIENT COOLING

Considering an axisymmetric jet, Equations (3.1b) and (3.1c) for the axial momentum balance and energy balance, respectively, read:

$$\rho\left(\frac{\partial v}{\partial t} + u\frac{\partial v}{\partial r} + v\frac{\partial v}{\partial z}\right) = -\frac{\partial p}{\partial z} + \frac{1}{r}\frac{\partial}{\partial r}\left(r\eta(T)\frac{\partial v}{\partial r}\right) + \frac{\partial}{\partial z}\left(\eta(T)\frac{\partial v}{\partial z}\right) \tag{3.A.1a}$$

$$\rho c_p\left(\frac{\partial T}{\partial t} + u\frac{\partial T}{\partial r} + v\frac{\partial T}{\partial z}\right) = k_c\left(\frac{\partial^2 T}{\partial r^2} + \frac{1}{r}\frac{\partial T}{\partial r} + \frac{\partial^2 T}{\partial z^2}\right) \tag{3.A.1b}$$

At the jet free surface $r = R(z, t)$, the outward normal and tangential unit vectors are given respectively by

$$\mathbf{n} = \frac{1}{\sqrt{1+R'^2}}\begin{bmatrix} 1 \\ 0 \\ -R' \end{bmatrix} \qquad\qquad \mathbf{t} = \frac{1}{\sqrt{1+R'^2}}\begin{bmatrix} R' \\ 0 \\ 1 \end{bmatrix}$$

where $R' = \partial R/\partial z$. The dynamic and thermal interface conditions, Eqs. (3.2) and (3.5) respectively, can then be written as:

$$p - \frac{2\eta(T)}{1+R'^2}\left[\frac{\partial u}{\partial r} - \left(\frac{\partial u}{\partial z} + \frac{\partial v}{\partial r}\right)R' + \frac{\partial v}{\partial z}R'^2\right] = \gamma(T)\kappa \tag{3.A.2a}$$

$$\frac{\eta(T)}{\sqrt{1+R'^2}}\left[2\left(\frac{\partial u}{\partial r} - \frac{\partial v}{\partial z}\right)R' + \left(\frac{\partial v}{\partial r} + \frac{\partial u}{\partial z}\right)(1-R'^2)\right] = \frac{d\gamma}{dT}\left[R'\frac{\partial T}{\partial r} + \frac{\partial T}{\partial z}\right] \tag{3.A.2b}$$

$$-\frac{k_c}{\sqrt{1+R'^2}}\left(\frac{\partial T}{\partial r} - R'\frac{\partial T}{\partial z}\right) = h_w\left(T - T_\infty\right) \tag{3.A.2c}$$

Inserting the radial expansions given by Eq. (3.6) into Eqs. (3.A.1) yields up to $O(r^2)$:

$$\rho\left(\frac{\partial v_0}{\partial t} + v_0 v_0'\right) = -p_0' + \eta(T)\left(4v_2 + v_0''\right) + 2\frac{d\eta}{dT}T_0' v_0' + O(r^2) \tag{3.A.3a}$$

$$\rho c_p\left(\frac{\partial T_0}{\partial t} + v_0 T_0'\right) = k_c\left(4T_2 + T_0''\right) + O(r^2) \tag{3.A.3b}$$

Note that the next lowest order in Eqs. (3.A.1) is $O(r^2)$, therefore Eqs. (3.A.3) also capture the full equations at $O(r)$. In line with the procedure detailed in [13], the interface conditions (3.A.2) can be used to eliminate the variables p_0, v_2 and T_2.

The normal stress condition (3.A.2a) will yield up to $O(r^2)$

$$p_0 + \eta(T)v_0' = \gamma(T)\kappa + O(r^2) \tag{3.A.4}$$

which can be used to eliminate p_0 in Eq. (3.A.3a).

When it comes to eliminating v_2 and T_2, there appears a peculiarity with the left and right hand sides being at seemingly different orders. The referee correctly underlines this peculiarity for the heat transfer condition at the interface, given in Eq. (3.A.2c), but the same is also apparent in the tangential stress balance given in Eq. (3.A.2b), and its justification is either overlooked or not explicitly provided in the works related to surfactant-laden breakup by Ambravaneswaran, Wee, Basaran and others[32, 34, 46, 47]. Up to $O(r^2)$ the tangential stress balance reduces to

$$\underbrace{\eta(T)\left(-3v_0'R' - \frac{1}{2}v_0''R + 2v_2R\right)}_{O(r)} = \frac{d\gamma}{dT}T_0' + O(r^2) \tag{3.A.5}$$

In the absence of a mechanism that induces a Marangoni stress (e.g. tangential temperature or surfactant gradients), the right hand side of (3.A.5) will vanish and an expression for v_2 is obtained without any inconsistencies with the order of terms. In the presence of Marangoni stresses, however, we require that $\partial\gamma/\partial z$ matches with the left hand side of $O(r)$ for consistency and hence $\partial\gamma/\partial z$ (thus $d\gamma/dT$) should be sufficiently small. So if one proceeds with solving (3.A.5) for v_2 one will arrive at

$$v_2 = \frac{1}{2\eta(T)R}\frac{d\gamma}{dT}\frac{\partial T}{\partial z} + \frac{3}{2}v_0'\frac{R'}{R} + \frac{v_0''}{4} \tag{3.A.6}$$

This is precisely the expression used in [32, 34, 46, 47] to close the 1D system as well as the works by Furlani where they considered surface tension modulation at the inlet [48, 49]. Note that in [48, 49] the surface tension gradient is fixed, so there is no additional balance equation for the surfactant concentration or thermal energy.

Looking at the physical side, this approach implicitly assumes that the tangential stress difference at the interface caused by the Marangoni stress is not too large. In cases where the Marangoni stress is not small, then the slender jet approach would not be useful as the viscous boundary layer within jet due to the high tangential stress could not be captured [50].

Along similar lines, one could justify the same choice in the heat transfer boundary condition. Up to $O(r^2)$ the heat transfer boundary condition at the interface reduces to:

$$\underbrace{-k_c\left(2T_2R - R'T_0'\right)}_{O(r)} = h_w\left(T_0 - T_\infty\right) + O(r^2) \tag{3.A.7}$$

If we proceed with solving for T_2, we get

$$T_2 = -\frac{h_w\left(T_0 - T_\infty\right)}{2k_cR} + \frac{T_0R'}{2R} \tag{3.A.8}$$

This expression is also obtained and used in the studies by Pillai et al [27], Furlani [29] and several others concerning nonisothermal melt spinning processes [51, 52]. This time, the physical explanation is related to the thermal boundary layer, namely, if the cooling to the ambient is too large ($Bi \gg 1$), then a thermal boundary layer would arise within the jet and the slender jet approach would be unable to capture the radial variation of the temperature near the jet edge.

3.B. VALIDATION OF THE NUMERICAL MODEL

In this section we provide some comparison against full 2D-axisymmetric simulations in the field of nozzle-driven jet breakup and the breakup of periodic filaments in a moving frame of reference.

In their recent study, McIlroy et al. [45] discussed the effect of the amplitude of velocity disturbances on the breakup characteristic of an isothermal jet. They observed a narrow window of amplitudes for which the filaments breakup on the upstream end rather than the downstream end (i.e. inverted pinching). This phenomenon is also discussed in our present paper with respect to the amplitude of the thermal perturbation (see Section 3.3.2). A comparison with a full 2D-axisymmetric solution for certain cases is also provided in [45], so we chose this work as a relevant benchmark case to test our code. Figure 3.B.1 shows our results for the case described in Section C of [45]. Results are in very good agreement with the 1D and 2D-axisymmetric results presented in [45]. The shift in the breakup characteristic from inverted pinching to downstream pinching is captured with our code as well.
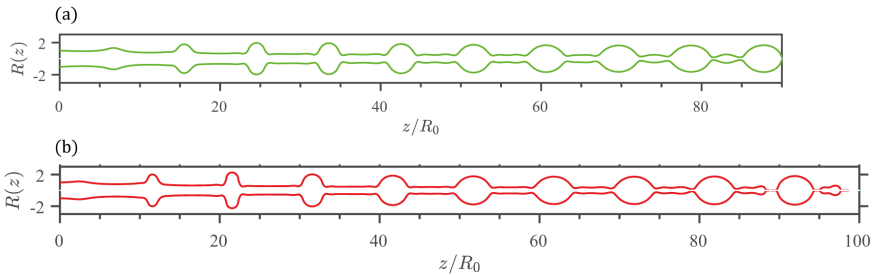
Figure 3.B.1: Free surface profiles from our 1D model with the regularization scheme. Our results are in near perfect agreement with the 1D and 2D-axisymmetric simulations shown in Fig. 11 of McIlroy et al. [45] . The model parameters are $We = 338$, $Oh = 0.122$, $kR_0 = 0.7$. The amplitude of velocity perturbations are (a) $\varepsilon_v = 0.1$ and (b) $\varepsilon_v = 0.15$. Shift from inverted pinching back to downstream pinching is reproduced with our code as well.

In addition to this, we provide a comparison with respect to another full-axisymmetric simulation from the literature by Mashayek et al. [25] where they consider nonisothermal breakup of liquid jets. Specifically, we ran a few simulations for the case described in §3.1 of [25] and tabulate the results in Table 3.B.1. While for low Biot number the agreement is excellent, for the high Biot numbers there is a discrepancy, which is due to

the same reasons mentioned in Appendix 3.A. Nevertheless, we were able to observe the shift from capillary breakup to thermocapillary breakup discussed in [25] (that happens around $Bi \approx 1.37$ according to their results) in between our cases, namely $Bi = 0.1$ to $Bi = 10$. The resultant filament shapes for the two Biot numbers are shown in Fig. 3.B.2.

Table 3.B.1: Tabulated comparison of the case described in §3.1 of [25]

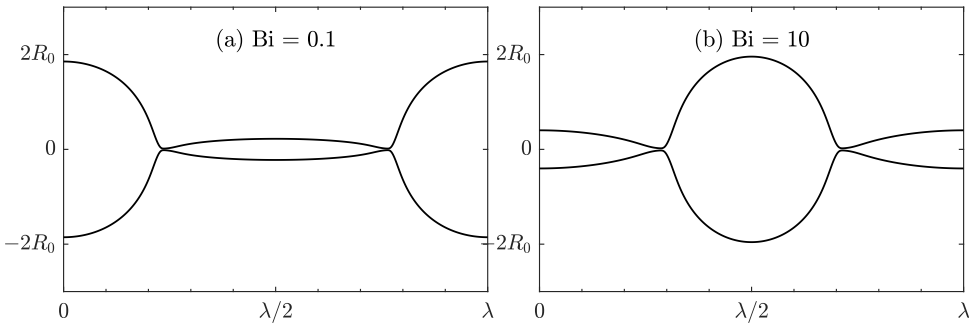|	$Bi = 0.1$		$Bi = 10$	
	Mashayek et al.	Our code	Mashayek et al.	Our code
Breakup time, t_b	26.82	26.23	23.99	29.05
Main drop radius	1.878	1.878	1.862	1.856
Satellite drop radius	0.474	0.473	0.656	0.694

Figure 3.B.2: Filament shapes from the case described in §3.1 of [25].

REFERENCES

[1] Y. E. Kamis, H. B. Eral, and W.-P. Breugem. "Active control of jet breakup and droplet formation using temperature modulation". In: *Physical Review Fluids* 6.10 (2021), p. 103903.

[2] H. N. Chapman, P. Fromme, A. Barty, T. A. White, R. A. Kirian, A. Aquila, M. S. Hunter, J. Schulz, D. P. DePonte, U. Weierstall, *et al.* "Femtosecond X-ray protein nanocrystallography". In: *Nature* 470.7332 (2011), pp. 73–77.

[3] M. O. Wiedorn, S. Awel, A. J. Morgan, K. Ayyer, Y. Gevorkov, H. Fleckenstein, N. Roth, L. Adriano, R. Bean, K. R. Beyerlein, *et al.* "Rapid sample delivery for megahertz serial crystallography at X-ray FELs". In: *IUCrJ* 5.5 (2018), pp. 574–584.

[4] H. B. Eral, M. O'Mahony, R. Shaw, B. L. Trout, A. S. Myerson, and P. S. Doyle. "Composite hydrogels laden with crystalline active pharmaceutical ingredients of controlled size and loading". In: *Chemistry of Materials* 26.21 (2014), pp. 6213–6220.

[5] H. B. Eral, E. R. Safai, B. Keshavarz, J. J. Kim, J. Lee, and P. S. Doyle. "Governing principles of alginate microparticle synthesis with centrifugal forces". In: *Langmuir* 32.28 (2016), pp. 7198–7209.

[6] C. M. Van't Land. *Industrial Crystallization of Melts*. CRC Press, 2004.

[7] L. Rayleigh. "On the capillary phenomena of jets". In: *Proc. R. Soc. London* 29.196-199 (1879), pp. 71–97.

[8] L. Rayleigh. "On the instability of cylinder fluid surfaces". In: *Philos. Mag* 34 (1892), pp. 145–54.

[9] S. Chandrasekhar. *Hydrodynamic and hydromagnetic stability*. Courier Corporation, 2013.

[10] J. B. Keller, S. I. Rubinow, and Y. O. Tu. "Spatial instability of a jet". In: *The Physics of Fluids* 16.12 (1973), pp. 2052–2055.

[11] S. J. Leib and M. E. Goldstein. "Convective and absolute instability of a viscous liquid jet". In: *The Physics of fluids* 29.4 (1986), pp. 952–954.

[12] J. Eggers. "Universal pinching of 3D axisymmetric free-surface flow". In: *Phys. Rev. Lett.* 71.21 (1993), p. 3458.

[13] J. Eggers and T. F. Dupont. "Drop formation in a one-dimensional approximation of the Navier–Stokes equation". In: *Journal of Fluid Mechanics* 262 (1994), pp. 205–221.

[14] J. Eggers. "Nonlinear dynamics and breakup of free-surface flows". In: *Reviews of modern physics* 69.3 (1997), p. 865.

[15]   D. T. Papageorgiou. "On the breakup of viscous liquid threads". In: *Physics of Fluids* 7.7 (1995), pp. 1529–1544.

[16]   D. T. Papageorgiou. "Analytical description of the breakup of liquid jets". In: *Journal of Fluid Mechanics* 301 (1995), pp. 109–132.

[17]   E. D. Wilkes, S. D. Phillips, and O. A. Basaran. "Computational and experimental analysis of dynamics of drop formation". In: *Physics of Fluids* 11.12 (1999), pp. 3577–3598.

[18]   B. Ambravaneswaran, E. D. Wilkes, and O. A. Basaran. "Drop formation from a capillary tube: Comparison of one-dimensional and two-dimensional analyses and occurrence of satellite drops". In: *Physics of Fluids* 14.8 (2002), pp. 2606–2621.

[19]   F. J. García, H. González, J. R. Castrejón-Pita, and A. A. Castrejón-Pita. "The breakup length of harmonically stimulated capillary jets". In: *Applied Physics Letters* 105.9 (2014), p. 094104.

[20]   T. Driessen, P. Sleutel, F. Dijksman, R. Jeurissen, and D. Lohse. "Control of jet breakup by a superposition of two Rayleigh–Plateau-unstable modes". In: *Journal of Fluid Mechanics* 749 (2014), pp. 275–296.

[21]   B. Keshavarz, V. Sharma, E. C. Houze, M. R. Koerner, J. R. Moore, P. M. Cotts, P. Threlfall-Holmes, and G. H. McKinley. "Studying the effects of elongational properties on atomization of weakly viscoelastic solutions using Rayleigh Ohnesorge Jetting Extensional Rheometry (ROJER)". In: *Journal of Non-Newtonian Fluid Mechanics* 222 (2015), pp. 171–189.

[22]   O. A. Basaran, H. Gao, and P. P. Bhat. "Nonstandard inkjets". In: *Annual Review of Fluid Mechanics* 45 (2013), pp. 85–113.

[23]   J.-J. Xu and S. H. Davis. "Instability of capillary jets with thermocapillarity". In: *Journal of Fluid Mechanics* 161 (1985), pp. 1–25.

[24]   H. Kuhlmann and H. J. Rath. "Hydrodynamic instabilities in cylindrical thermocapillary liquid bridges". In: *Journal of Fluid Mechanics* 247 (1993), pp. 247–274.

[25]   F. Mashayek and N. Ashgriz. "Nonlinear instability of liquid jets with thermocapillarity". In: *Journal of Fluid Mechanics* 283 (1995), pp. 97–123.

[26]   Z. Gao and K. Ng. "Thermal modulation and breakup of liquid jets". In: *International Journal for Numerical Methods in Fluids* 70.3 (2012), pp. 326–341.

[27]   D. S. Pillai, P. Narayanan, S. Pushpavanam, T. Sundararajan, A. Jasmin Sudha, and P. Chellapandi. "A nonlinear analysis of the effect of heat transfer on capillary jet instability". In: *Physics of Fluids* 24.12 (2012), p. 124106.

[28]   R. W. Faidley and R. L. Panton. "Measurement of liquid jet instability induced by surface tension variations". In: *Experimental Thermal and Fluid Science* 3.4 (1990), pp. 383–387.

[29]   E. P. Furlani, B. G. Price, G. Hawkins, and A. G. Lopez. "Thermally induced Marangoni instability of liquid microjets with application to continuous inkjet printing". In: *Proceedings NSTI Nanotechnology Conference.* 2006.

[30] J. M. Chwalek, D. P. Trauernicht, C. N. Delametter, R. Sharma, D. L. Jeanmaire, C. N. Anagnostopoulos, G. A. Hawkins, B. Ambravaneswaran, J. C. Panditaratne, and O. A. Basaran. "A new method for deflecting liquid microjets". In: *Physics of Fluids* 14.6 (2002), pp. L37–L40.

[31] R. Suryo and O. A. Basaran. "Dripping of a liquid from a tube in the absence of gravity". In: *Phys. Rev. Lett.* 96.3 (2006), p. 034504.

[32] B. Ambravaneswaran and O. A. Basaran. "Effects of insoluble surfactants on the nonlinear deformation and breakup of stretching liquid bridges". In: *Physics of Fluids* 11.5 (1999), pp. 997–1015.

[33] P. M. Kamat, B. W. Wagoner, S. S. Thete, and O. A. Basaran. "Role of Marangoni stress during breakup of surfactant-covered liquid threads: Reduced rates of thinning and microthread cascades". In: *Phys. Rev. Fluids* 3 (4 Apr. 2018), p. 043602. DOI: 10.1103/PhysRevFluids.3.043602. URL: https://link.aps.org/doi/10.1103/PhysRevFluids.3.043602.

[34] H. Wee, B. W. Wagoner, P. M. Kamat, and O. A. Basaran. "Effects of Surface Viscosity on Breakup of Viscous Threads". In: *Phys. Rev. Lett.* 124 (20 May 2020), p. 204501. DOI: 10.1103/PhysRevLett.124.204501. URL: https://link.aps.org/doi/10.1103/PhysRevLett.124.204501.

[35] I. Orlanski. "A simple boundary condition for unbounded hyperbolic flows". In: *Journal of Computational Physics* 21.3 (1976), pp. 251–269.

[36] B. Van Leer. "Towards the ultimate conservative difference scheme. II. Monotonicity and conservation combined in a second-order scheme". In: *Journal of Computational Physics* 14.4 (1974), pp. 361–370.

[37] T. Driessen and R. Jeurissen. "A regularised one-dimensional drop formation and coalescence model using a total variation diminishing (TVD) scheme on a single Eulerian grid". In: *International Journal of Computational Fluid dynamics* 25.6 (2011), pp. 333–343.

[38] C. Clasen, J. Eggers, M. A. Fontelos, J. Li, and G. H. McKinley. "The beads-on-string structure of viscoelastic threads". In: *Journal of Fluid Mechanics* 556 (2006), pp. 283–308.

[39] A. Umemura. "Self-destabilising loop of a low-speed water jet emanating from an orifice in microgravity". In: *Journal of Fluid Mechanics* 797 (2016), pp. 146–180.

[40] A. M. Ganán-Calvo, H. N. Chapman, M. Heymann, M. O. Wiedorn, J. Knoska, Y. Du, B. Ganan-Riesco, M. A. Herrada, J. M. López-Herrera, F. Cruz-Mazo, *et al.* "The natural breakup length of a steady capillary jet". In: *arXiv preprint arXiv:1908.10841* (2019).

[41] S. Le Dizès and E. Villermaux. "Capillary jet breakup by noise amplification". In: *Journal of Fluid Mechanics* 810 (2017), pp. 281–306.

[42] U. S. Sauter and H. W. Buggisch. "Stability of initially slow viscous jets driven by gravity". In: *Journal of Fluid Mechanics* 533 (2005), pp. 237–257.

[43] J. Meessen and H. Petersen. *Urea, Uhlmann's Encyclopedia of Industrial Chemistry*. 2010.

3

[44] W. T. Pimbley and H. C. Lee. "Satellite droplet formation in a liquid jet". In: *IBM Journal of Research and Development* 21.1 (1977), pp. 21–30.

[45] C. McIlroy and O. G. Harlen. "Effects of drive amplitude on continuous jet breakup". In: *Physics of Fluids* 31.6 (2019), p. 064104.

[46] Y.-C. Liao, E. I. Franses, and O. A. Basaran. "Deformation and breakup of a stretching liquid bridge covered with an insoluble surfactant monolayer". In: *Physics of Fluids* 18.2 (2006), p. 022101.

[47] H. Wee, B. W. Wagoner, V. Garg, P. M. Kamat, and O. A. Basaran. "Pinch-off of a surfactant-covered jet". In: *Journal of Fluid Mechanics* 908 (2021).

[48] E. P. Furlani. "Temporal instability of viscous liquid microjets with spatially varying surface tension". In: *Journal of Physics A: Mathematical and General* 38.1 (2004), p. 263.

[49] E. P. Furlani and M. S. Hanchak. "Nonlinear analysis of the deformation and breakup of viscous microjets using the method of lines". In: *International Journal for Numerical Methods in Fluids* 65.5 (2011), pp. 563–577.

[50] A. Martínez-Calvo, J. Rivero-Rodríguez, B. Scheid, and A. Sevilla. "Natural breakup and satellite formation regimes of surfactant-laden liquid threads". In: *Journal of Fluid Mechanics* 883 (2020).

[51] K. Gupta and P. Chokshi. "Stability analysis of non-isothermal fibre spinning of polymeric solutions". In: *Journal of Fluid Mechanics* 851 (2018), pp. 573–605. DOI: 10.1017/jfm.2018.504.

[52] D. Deshawar and P. Chokshi. "Stability analysis of a thinning electrified jet under nonisothermal conditions". In: *Physical Review E* 103.2 (2021), p. 023107.

4

CONTRACTION BEHAVIOUR OF NEWTONIAN LIQUID JETS ISSUED FROM A CIRCULAR NOZZLE

In the studies of jet breakup in the preceding chapters, it was implicitly assumed that the undisturbed jet radius at nozzle exit is equal to the nozzle radius. However, jets with a nonuniform velocity profile leaving round orifices undergo complex dynamics that make them expand or contract rapidly over a distance of a few nozzle radii till the velocity reaches a uniform plug flow profile. This has implications for jet breakup as the base jet radius sets the length scale of the capillary stresses responsible for breakup. In this chapter, we study the complex interplay of inertial, viscous and capillary stresses responsible for the rapid adjustment of the Newtonian base jet at nozzle exit, related to the change in the no-slip condition for the flow inside the nozzle to a free-slip condition at the jet/air interface outside the nozzle.

4.1. INTRODUCTION

The shape of the interface of a liquid emanating from a circular orifice into ambient air has been a benchmark problem for decades that reveals fundamental insights about the rheological behaviour of the working liquid. The radius of the jet that emanates from such orifice evolves spatially downstream in a non-monotonic manner, caused by the interplay between inertia, viscous forces, surface tension and body forces such as gravity. In the cases where the flow is in the direction of a dominant body force (e.g., gravity), the interface can be estimated using a "free-fall" approach that satisfies mass conservation, since viscous and surface tension effects decay rapidly downstream compared to the spatial variation scale of the flow due to gravitational effects [1]. The jets are then subject to thinning starting immediately after the nozzle, until the local inertio-capillary timescale is sufficiently small for surface tension forces to cause the breakup of the jet.

When the body forces are negligible compared to other forces such as inertial, viscous and capillary forces, the prediction of the shape of the liquid-air interface becomes an intricate problem that concerns the interplay of these forces. Depending on the flow conditions and the rheological properties of the working liquid, the jet may expand or contract after leaving the nozzle. Furthermore, the jet interface may contain an inflection point, meaning that an initially contracting jet may end up in a radius that is larger than the orifice far downstream. One factor that becomes increasingly important with more complex rheology is the flow history upstream the nozzle. One of the well-known phenomena in this regard is the die-swell observed in viscoelastic liquids, where normal stress differences would then cause the swelling of the jet after the nozzle exit [2].

Although the normal stress differences inherently vanish for Newtonian jets, it is known that the Newtonian jets do also expand at low Reynolds numbers, while they contract at high Reynolds numbers as sketched in Fig. 4.1 [3–5]. Provided that the nozzle is sufficiently long and the flow is in the laminar regime, the flow sufficiently far upstream of the nozzle exit takes a parabolic profile corresponding to Poiseuille flow. The rapid adjustment of the jet when leaving the nozzle, relates to a change in the no-slip condition for the flow inside the nozzle to a free-slip condition at the jet/air interface outside the nozzle. The aim of the present study is to unravel the underlying physical mechanisms for the rapid jet adjustment of a Newtonian jet with an initially parabolic profile far upstream of the nozzle exit, with a particular focus on the transition from expanding to contracting jets at increasing Reynolds number. We have conducted a CFD study using OpenFoam and analysed the jet adjustment by means of an integral streamwise momentum balance for the flow inside the nozzle and the jet.

The prime motivation for the present study is related to jet breakup such as in prilling applications [6]. In modelling jet breakup and formation of drops it is often assumed that the initial jet radius is equal to the nozzle radius and that the initial velocity distribution of a non-agitated jet is uniform. This is generally not completely true in real applications, dependent on the flow conditions upstream of the nozzle (including possible clogging effects), the properties of the working fluid (density, viscosity), and the nozzle geometry (such as the shape of the nozzle entrance and the size and length of the nozzle). Furthermore, while viscous effects might be negligible inside the jet because of the typically high Reynolds number, this will generally not be true for the flow inside the nozzle from which the jet emanates. For high Reynolds number jet flows of a Newtonian

fluid with an initially parabolic velocity profile, Harmon [3] predicted a rapid contraction of the jet by approximately 13.4%. When jet breakup is forced under a given harmonic perturbation by the capillary-inertial Rayleigh-Plateau instability, this would imply also the formation of drops with a smaller radius by the same percentage as compared to a jet that does not undergo any significant jet contraction or expansion [7]. This is a significant effect and underlines the importance to better understand and model the rapid jet adjustment at nozzle exit in order to improve predictions of, e.g., prill size distribution in prilling applications [6].

The remainder of the chapter is structured as follows. In Section 4.2 a polynomial equation is derived for the jet contraction ratio using an integral mass and momentum balance. The numerical method and computational setup are explained in Section 4.3. The results from the numerical simulations are presented and discussed in Section 4.4. Finally, the main conclusions and a closing discussion are given in Section 4.5
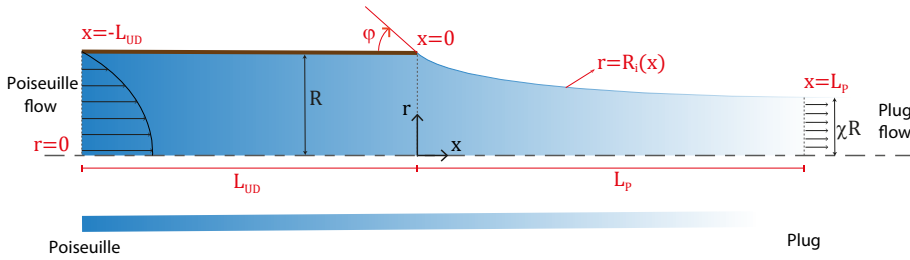

Figure 4.1: Schematic of the problem. L_{UD} is the distance over which the Poiseuille profile is altered by upstream diffusion. L_P is the distance measured from the nozzle where the flow becomes uniform, i.e., plug flow.

4.2. DERIVATION OF POLYNOMIAL EQUATION FOR JET CONTRACTION RATIO

The set of equations for an incompressible liquid at steady state are as follows:

$$\nabla \cdot \mathbf{u} = 0, \tag{4.1a}$$

$$\rho \nabla \cdot \mathbf{u}\mathbf{u} = -\nabla p + \nabla \cdot \tau + \rho \mathbf{g}, \tag{4.1b}$$

where $\tau = \mu \left[\nabla \mathbf{u} + \nabla \mathbf{u}^T \right]$ is the deviatoric stress tensor for a Newtonian fluid and μ is the dynamic viscosity. We consider a flow which has a fully developed Poiseuille profile beyond a distance L_{UD} upstream of the nozzle and plug flow beyond a distance L_P downstream of the nozzle. In the region $x < -L_{UD}$ the steady unidirectional velocity field is described by the Hagen-Poiseuille equation for a Newtonian fluid and the parabolic velocity profile in the tube is given by:

$$u(r) = -\frac{dp}{dx} \frac{R^2}{4\mu} \left(1 - \frac{r^2}{R^2} \right), \tag{4.2}$$

where $-dp/dx$ is the streamwise pressure gradient that drives the flow and R is the tube radius. The bulk velocity U_b within the tube is half the maximum velocity at the center-line:

$$U_b = \frac{u(0)}{2} = -\frac{dp}{dx}\frac{R^2}{8\mu}. \tag{4.3}$$

The integral mass and momentum fluxes across the plane $x = -L_{UD}$ are given by, respectively:

$$\dot{m}_{UD} = \int_0^R \rho u(r)2\pi r dr = \rho\pi R^2 U_b, \tag{4.4a}$$

$$\dot{M}_{UD} = \int_0^R \rho u(r)^2 2\pi r dr = \rho\frac{4\pi}{3}R^2 U_b^2. \tag{4.4b}$$

From $x = L_P$ onwards, the flow is assumed to retain plug flow characteristics with a jet velocity U_j, provided that the stretching due to gravity is negligible. The mass and momentum fluxes sufficiently far downstream then become:

$$\dot{m}_p = \int_0^{\chi R} \rho U_j 2\pi r dr = \rho\pi\left(\chi R\right)^2 U_j, \tag{4.5a}$$

$$\dot{M}_p = \int_0^{\chi R} \rho U_j^2 2\pi r dr = \rho\pi\left(\chi R\right)^2 U_j^2. \tag{4.5b}$$

Mass conservation dictates that the mass fluxes given by Eq. (4.4a) and Eq. (4.5a) must be equal to each other, yielding $U_b = \chi^2 U_j$. Likewise, in the inertia-dominated regime (i.e., when gravity, viscous and capillary forces are negligible), the momentum fluxes given by Eqs. (4.4b) and (4.5b) must be equal, which implies that $\chi = \sqrt{3}/2 \approx 0.866$ [3] and thus a jet contraction of approximately 13.4%.

Between these planes ($x \in [-L_{UD}, L_P]$) the flow is altered by the combination of inertia, viscous diffusion and surface tension. The integral momentum balance upstream of the nozzle exit plane is obtained from integrating Eq.(4.1b) over the region $x \in [-L_{UD}, 0]$:

$$\dot{M}_0 - \dot{M}_{UD} = \rho g\pi R^2 L_{UD} - \int_0^R \left(p|_{x=0} - p|_{x=-L_{UD}}\right)2\pi r dr + \int_{-L_{UD}}^0 \tau_{xr}2\pi R dx|_{r=R}, \tag{4.6}$$

where we used that for a Newtonian fluid, $\int_0^R \tau_{xx}|_{x=0}2\pi r dr = 2\mu\frac{\partial}{\partial x}\left(\int_0^{R_i} u2\pi r dr\right) = 0$ since $u(0, R) = 0$ and $\int_0^{R_i} u2\pi r dr = \pi R^2 U_b$ is constant in x.

Beyond the nozzle exit at $x = 0$, one has the stress boundary conditions at the free surface denoted by $R_i(x)$:

$$p(x, R_i(x)) = p_{atm} + \mathbf{n}\cdot\tau\cdot\mathbf{n} + \gamma\kappa, \tag{4.7a}$$

$$\mathbf{t}\cdot\tau\cdot\mathbf{n} = 0, \tag{4.7b}$$

where $\mathbf{n}$ is the outward unit normal vector at the interface, $\mathbf{t}$ is the unit tangent vector along the interface, γ is the surface tension coefficient and κ is the curvature of the free surface given by:

$$\kappa = \frac{1}{R_i R_i'}\frac{d}{dx}\left(\frac{R_i}{\sqrt{1 + R_i'^2}}\right) \qquad \left(R_i'(x) \equiv \frac{dR_i}{dx}\right). \tag{4.8}$$

The integral momentum balance for the region downstream of the nozzle can be obtained by integrating Eq. (4.1b) over the region ($x \in [0, L_P]$). Using the interface conditions given by Eqs. (4.7a) and (4.7b), the following result is obtained:

$$\dot{M}_P - \dot{M}_0 = \rho g V_c + \int_0^R p 2\pi r\, dr|_{x=0} - \int_0^{\chi R} p 2\pi r\, dr|_{x=L_P} + \underbrace{\int_0^{L_P} \gamma \kappa R_i' 2\pi R_i\, dx}_{F_{cap}}$$

$$+ \int_0^{L_P} p_{atm} R_i' 2\pi R_i\, dx + \underbrace{\int_0^{L_P} \left[(\mathbf{n} \cdot \boldsymbol{\tau} \cdot \mathbf{n} - \tau_{xx})_i \cdot R_i' + (\tau_{xr})_i \right] 2\pi R_i\, dx}_{F_{visc}} \quad (4.9)$$

where $V_c = \int_0^{L_P} \pi R_i(x)^2\, dx$ is the volume of the contraction region. Note that we again used that $\int_0^R \tau_{xx}|_{x=0} 2\pi r\, dr = 0$ for a Newtonian fluid. Thus the *direct* contribution from streamwise viscous stresses to the jet contraction ratio is equal to zero, contrary to explanations in literature that attribute viscous effects on the jet contraction ratio to this term [4]. However, viscous stresses do affect the flow upstream of the nozzle exit plane and the pressure distribution within the nozzle exit plane. This *indirect* effect constitutes the viscous contribution to the jet contraction ratio. The 4th and 5th terms of the integral momentum balance of the contraction region given in Eq. (4.9) represent the capillary forces, F_{cap}, and viscous forces acting on the free surface, F_{visc}, respectively.

When Eq. (4.8) is plugged into Eq. (4.9), we obtain the following expression for the capillary force F_{cap}:

$$F_{cap} = \int_0^{L_P} \gamma \kappa R_i' 2\pi R_i\, dx = 2\pi R \gamma \left[\chi - \cos\varphi \right] \quad (4.10)$$

To determine the viscous force exerted by the free surface, one has to use the normal and tangential vectors of the free surface $R_i(x)$ given by:

$$\mathbf{n} = \frac{1}{\left(1 + R_i'^2\right)^{1/2}} \begin{bmatrix} 1 \\ 0 \\ -R_i' \end{bmatrix}, \qquad \mathbf{t} = \frac{1}{\left(1 + R_i'^2\right)^{1/2}} \begin{bmatrix} R_i' \\ 0 \\ 1 \end{bmatrix} \quad (4.11)$$

Using these expressions, we obtain the following relations valid at the free surface $R_i(x)$:

$$\mathbf{n} \cdot \boldsymbol{\tau} \cdot \mathbf{n} = \frac{\tau_{rr} - \tau_{xx} R_i'^2}{1 - R_i'^2}, \quad (4.12a)$$

$$\mathbf{t} \cdot \boldsymbol{\tau} \cdot \mathbf{n} = \frac{\tau_{xr} - \tau_{xx} R_i' + \left(\tau_{rr} - \tau_{xr} R_i'\right) R_i'}{1 + R_i'^2} = 0. \quad (4.12b)$$

Solving (4.12b) for the shear component, τ_{xr}, yields:

$$\tau_{xr} = (\tau_{xx} - \tau_{rr}) \frac{R_i'}{1 - R_i'^2}. \quad (4.13)$$

Combining the expressions given in (4.12a) and (4.13) to derive F_{visc}, reveals that the viscous force contribution by the free surface is actually zero.

With $F_{visc} = 0$, the summation of the integral momentum balances given by Eq. (4.6) and Eq. (4.9) is given by:

$$
\dot{M}_P \quad - \quad \dot{M}_{UD} = \rho g \left[V_c + \pi R^2 L_{UD} \right] + \left[p|_{x=-L_{UD}} - p_{atm} \right] \pi R^2
$$

$$
+ \quad \int_{-L_{UD}}^{0} \tau_{xr}|_{r=R} 2\pi R \, dx + \gamma \pi R \left[\chi - 2\cos\varphi \right] \tag{4.14}
$$

The expression is nondimensionalized using R as the length scale, U_b as the velocity scale (thus R/U_b as time scale), pressure is normalized by ρU_b^2 and the viscous shear stress by $\mu U_b / R$. Plugging the expressions for the momentum fluxes $\dot{M}_{UD}$ and $\dot{M}_P$, given respectively by (4.4b) and (4.5b), into (4.14) and dividing both sides by $\rho \pi R^2 U_b^2$, one obtains:

$$
\frac{1}{\chi^2} - \frac{4}{3} \quad = \quad \frac{1}{Fr^2} \left[\frac{V_c}{\pi R^3} + \tilde{L}_{UD} \right] + \left[\tilde{p}|_{\tilde{x}=-\tilde{L}_{UD}} - \tilde{p}_{atm} \right]
$$

$$
+ \quad \frac{4}{Re} \int_{-\tilde{L}_{UD}}^{0} \tilde{\tau}_{xr}|_{\tilde{r}=1} d\tilde{x} + \frac{1}{We} \left[\chi - 2\cos\varphi \right], \tag{4.15}
$$

where $Re = \rho U_b 2R/\mu$ is the Reynolds number, $We = \rho U_b^2 R/\gamma$ is the Weber number and $Fr = U_b/\sqrt{gR}$ is the Froude number. When gravity and surface tension effects are negligible, the first and last term at the right-hand side vanish. When in addition the Reynolds number is high, Poiseuille flow can be assumed everywhere in the nozzle up to the nozzle exit plane and the second and third term at the right-hand side cancel out. This case is the inertia-dominated regime mentioned before, for which $\chi = \sqrt{3}/2$. For lower Reynolds numbers, when viscous effects cannot be neglected, the flow immediately upstream of the nozzle exit will deviate from perfect Poiseuille flow and the second and third term will not cancel out anymore. In the remainder of our present study, we will neglect gravity and focus on the viscous and surface contributions to the jet contraction ratio.

Equation (4.15) can be rearranged into a polynomial form in χ as follows:

$$
A\chi^3 + B\chi^2 + C\chi + D = 0. \tag{4.16a}
$$

In the limit of $Fr \to \infty$, the coefficients read:

$$
A = \frac{1}{We}, \qquad B = \tilde{K} - \frac{2\cos\varphi}{We} + \frac{4}{3} \qquad C = 0, \qquad D = -1, \tag{4.16b}
$$

$$
\tilde{K} = \tilde{p}|_{\tilde{x}=-\tilde{L}_{UD}} - \tilde{p}_{atm} + \frac{4}{Re} \int_{-\tilde{L}_{UD}}^{0} \tilde{\tau}_{xr}|_{\tilde{r}=1} d\tilde{x}.
$$

where $\tilde{K}$ constitutes the viscous contribution from the flow upstream of the nozzle exit to the jet contraction ratio. A similar derivation of the integral momentum balance was provided before by Joseph [8], albeit expressed in a different form. He proposed the following correlation for $\tilde{K}$:

$$\tilde{K} = -\frac{K_1}{Re^{2/3}}, \tag{4.17}$$

with K_1 a constant. When gravity and surface tension effects are negligible, the following expression for the jet contraction ratio can then be derived from Eqs. (4.16a) and (4.16b):

$$\chi = \frac{\frac{1}{2}\sqrt{3}}{\sqrt{1 - \frac{3}{4}\frac{K_1}{Re^{2/3}}}}, \tag{4.18}$$

where $K_1 = 1.97$ was selected by Joseph [8] to fit the point $\chi(Re = 14.4) = 1$.

4.3. NUMERICAL METHOD AND COMPUTATIONAL SETUP

To evaluate the contributions of the different terms at the right-hand side of Eq. (4.15) for the jet contraction ratio, we made use of the open source codes OpenFOAM and the rheoTool extension to simulate this problem. The solver rheoInterFoam uses the Volume-of-Fluid method with non-Newtonian properties for both phases. In this study, both phases are assumed to be Newtonian with the density and the viscosity of the ambient gas being sufficiently small to ensure negligible dynamical effect. Namely the density and viscosity ratios are taken as $\rho_a/\rho = 5e-3$ and $\eta_a/\eta = 1e-7$, respectively. The computational domain and the boundary conditions are detailed in Fig. 4.2. All coordinates given in Fig. 4.2 are normalized by the nozzle radius, R.
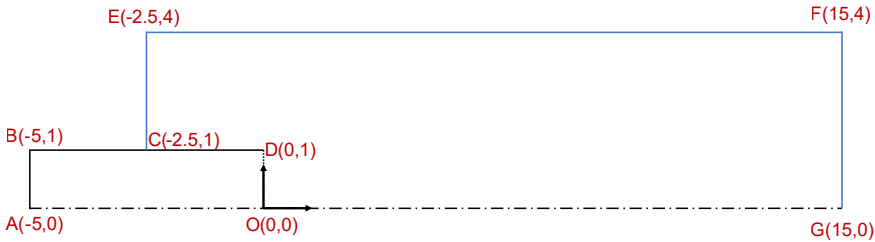

Figure 4.2: Computational setup

The incompressible Navier-Stokes equations were solved in cylindrical coordinates for the flow geometry shown in Fig. 4.2. The simulations were 2D, assuming axisymmetry of the flow in the azimuthal direction. The simulations were carried out in time-dependent fashion with a first-order implicit Euler scheme. The time step was dynamically adjusted to ensure numerical stability. A sufficiently fine computationally mesh of 116000 cells was used to resolve the flow. Mesh refinement was applied near the nozzle wall and around the nozzle exit plane, see Fig. 4.3. A free-slip boundary condition is used for the centerline. A no-slip condition is imposed at BD, the nozzle wall. A parabolic Poiseuille flow is imposed at AB, the upstream entrance of the nozzle. A convective outflow boundary condition is used at the downstream boundary of the domain. To ensure a pinned contact line at the nozzle exit, Dirichlet boundary condition is used at CD, the outer wall
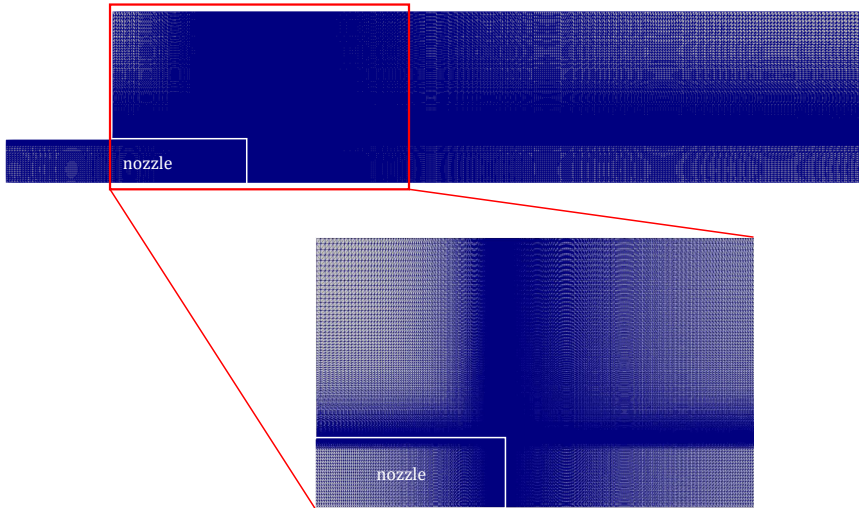
Figure 4.3: The mesh over the computational domain

of the nozzle, where the Volume-of-Fluid function is set to be zero such that ambient phase is enforced. *CE*, *EF* and *FG* are sufficiently far from the nozzle and have zero gradient boundary conditions for velocity, pressure and the Volume-of-Fluid function. The initial condition of the simulation is a Poiseuille profile for the velocity inside the nozzle and (initially) straight jet. The simulations were run until convergence was reached for the jet shape and velocity distribution.

We have conducted a total of 10 simulations. The dimensionless numbers of the simulations are listed in Table 4.1 and were taken after the experiments reported by Goren and Wronski [9]. This serves both to validate the simulations with the available experimental data for the jet shape and to use the simulation for an in-depth study of the flow dynamics.

4.4. RESULTS AND DISCUSSION

Figure 4.4 depicts the results for the normalised jet radius as function of the streamwise distance along the jet for all ten simulations. The comparison with the experimental data of Goren and Wronski [9] is generally good, in particular for the cases with Re = 4.2 and Re = 11.8. We speculate that the small deviations from the experimental data observed for the other cases might be related to uncertainty in the precise values of the governing dimensionless numbers. For instance, the slight overprediction of the jet thickness for Re = 7.2 suggests that the Reynolds number was slightly higher in the experiment.

Figure 4.4 shows that sufficiently far downstream, the jet expands for Re up to 14, while for Re of 14.8 and higher the jet contracts. This suggests a transition Reynolds number of $Re \approx 14.4$ for the jet contraction behavior. Interestingly, for Reynolds numbers in the

Table 4.1: Governing dimensionless numbers of the simulated cases, based on the experiments of Goren & Wronski [9]. Note that gravity effects have been neglected in their analysis, hence no Froude number is given.

Case #	$Re = \frac{\rho U_b 2R}{\mu}$	$We = \frac{\rho U_b^2 R}{\gamma}$	$Ca = \frac{\mu U_b}{\gamma}$
1	4.2	16.1	7.66
2	7.2	45.8	12.7
3	10.1	88.5	17.5
4	11.8	118.2	20
5	14	164.2	23.5
6	14.8	182	24.6
7	16.6	225.6	27.2
8	18	262.9	29.2
9	24	458.6	38.2
10	47.4	1733.8	73.2

range of 10.1 until 14, the jet first contracts towards a local minimum and then expands to a value higher than the initial radius far downstream. A similar behavior is observed for $Re = 14.8$ until 24, though the jet does not expand beyond the initial value in these cases. For the highest investigated Reynolds number, $Re = 47.4$, the jet gradually contracts. The jet contraction/expansion behavior for intermediate Reynolds number suggests competing influences of viscous stresses (responsible for jet expansion) and inertial flow effects (responsible for jet contraction).
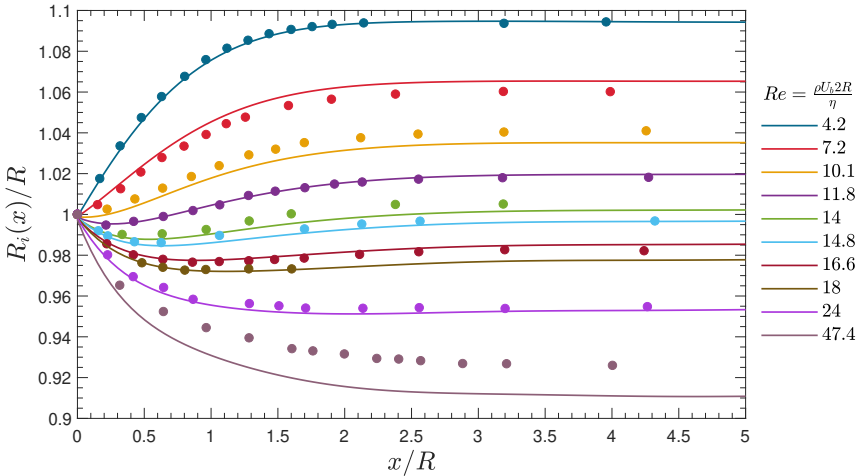

Figure 4.4: Numerical results for the jet radius normalised with the nozzle radius for the cases listed in Table 4.1. The dots are experimental data from Goren & Wronski [9].

Figure 4.5(a) presents results for the jet contraction ratio. This has been obtained from the simulations in two different ways: (1) by directly measuring the equilibrium radius far downstream from the obtained jet radius profiles, and (2) by computing χ from Eq. (4.16a) with the coefficient B calculated numerically from the expression given in Eq. (4.16b). The two methods give nearly the same value for the jet contraction ratio, which validates our derivation of the integral momentum balance from which χ was determined. Good agreement is obtained with the experimental data from Goren and Wronski [9]. The correlation for the jet contraction ratio proposed by Joseph [8], given by Eq. (4.18), provides a good fit to the data down to $Re \approx 12$, below which the jet contraction ratio levels off to a value somewhat above 1.1, while the correlation diverges towards infinity for $Re \to 0$.
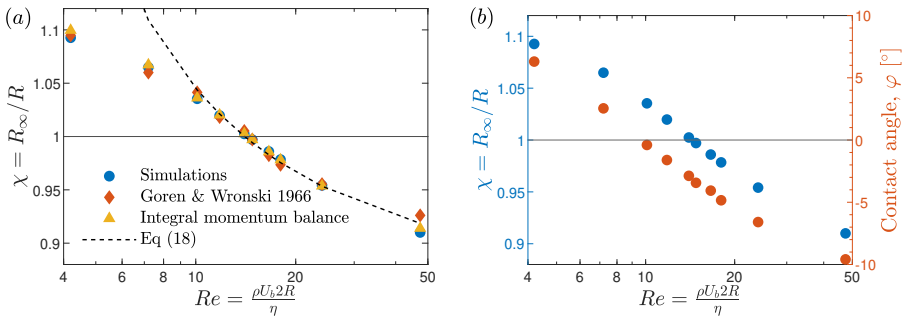

Figure 4.5: (a) Jet contraction ratio as function of Reynolds number. The data points show the results obtained from the simulations, the experiments of Goren and Wronski [9], and reconstructed from the integral momentum balance. (b) Simulation results for the final jet radius, $R_\infty/R = \chi$ and the contact angle φ (in degrees, see Fig. 4.1 for definition) as function of Reynolds number.

Figure 4.5(b) depicts the numerical results for the final jet radius far downstream and the contact angle at the nozzle (see Fig. 4.1 for definition), $R_\infty/R = \chi$ and φ, respectively, as function of the Reynolds number. One can observe the non-monotonic jet behaviour for the Reynolds numbers between 8 and 14. In this range, the resultant jet radius is still larger than the nozzle radius (i.e., $\chi > 1$) but the contact angle is negative, meaning the jets are initially contracting but eventually expanding to reach their final radii.

Figure 4.6 depicts the pressure, radial and axial velocity distribution across the jet for $Re = 4.2, 10.1, 24$, corresponding to an expanding, contracting/expanding and contracting jet, respectively. With increasing Reynolds number, axial pressure variations decrease in magnitude in units of ρU_b^2, as expected. Radial velocity perturbations are localized at the nozzle exit plane. Normalised with U_b, the radial velocity perturbations decrease in magnitude with increasing Reynolds number and spread out further downstream related to streamwise advection by the higher axial velocity. Finally, the axial velocity distribution shows an increasing downstream flow development length with increasing Reynolds number.

Fig. 4.7 depicts the centerline velocity as function of streamwise distance for each investigated Reynolds number. The velocity has been normalized with the bulk velocity
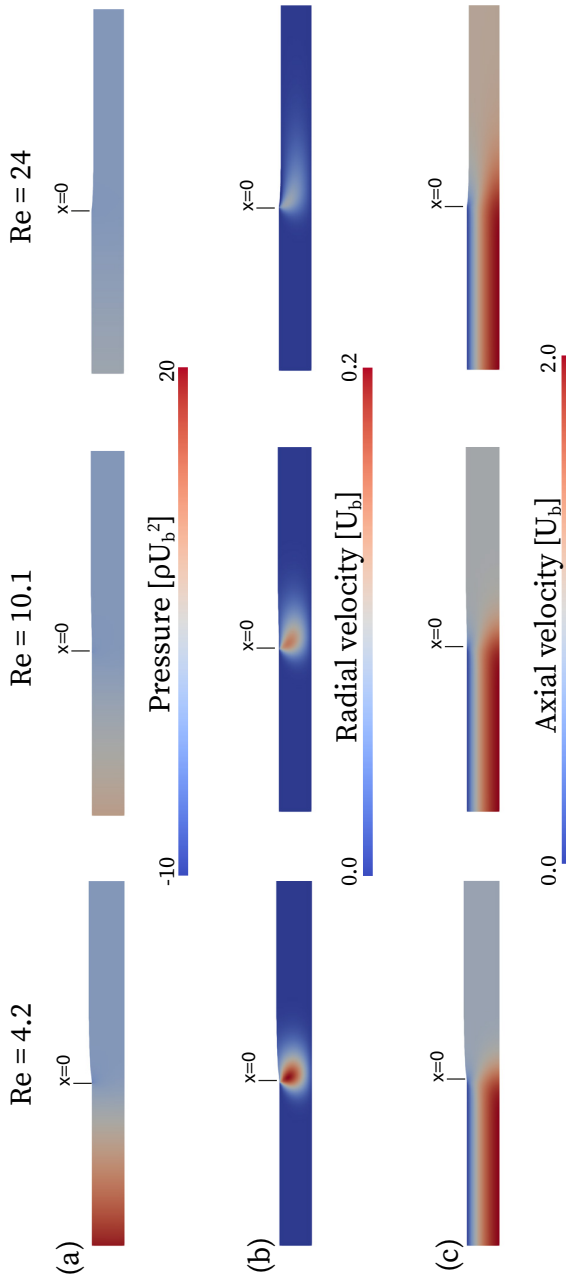
Figure 4.6: Color plots of (*a*) pressure in units of ρU_b^2 (*b,c*) radial and axial velocity, respectively, in units of U_b, for Reynolds numbers of 4.2, 10.1 and 24.
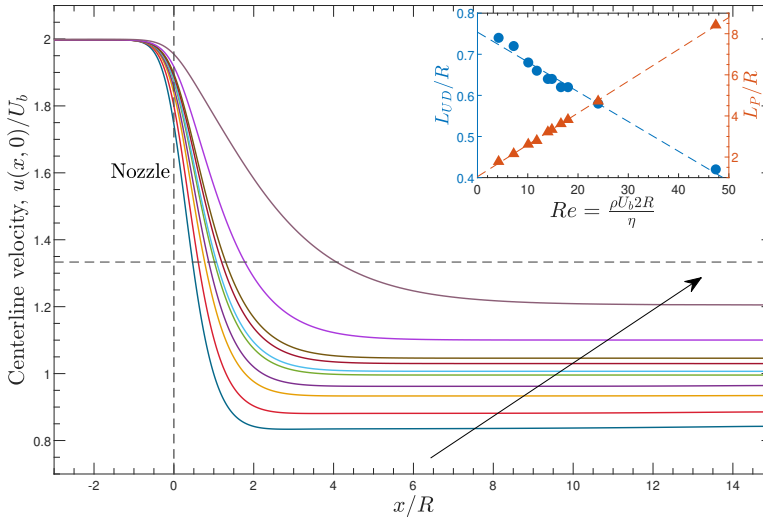
Figure 4.7: Centerline velocities at different Reynolds numbers. The inset shows the variation of the upstream diffusion length, L_{UD}, and the velocity relaxation length, L_P, as a function of Reynolds number.

upstream in the nozzle, U_b. At all Reynolds numbers the centerline velocity decreases monotonically from a distance on the order of one nozzle radius upstream of the nozzle exit to an equilibrium value sufficiently far downstream. At the highest Reynolds number, $Re = 47.4$, the equilibrium value is about 1.2, which is still significantly below the value of 4/3 (≈ 1.33) expected in the inertia-dominated regime.

The decrease in the streamwise centerline velocity in the nozzle exit plane implies the local presence of a compressional axial viscous stress, $\tau_{xx} = 2\mu\partial u/\partial x < 0$. Mass conservation dictates that this must be accompanied by a radially outward velocity gradient (as indeed observed from Fig. 4.6b) and hence the local presence of an extensional radial viscous stress at the centerline, $\tau_{rr} = 2\mu\partial v/\partial r > 0$. The reverse situation is encountered near the nozzle edge, where $\tau_{xx} > 0$ immediately downstream of the nozzle edge. In this case, mass conservation requires that $\partial(rv)/\partial r < 0$ immediately downstream of the nozzle edge. As observed from Fig. 3, for sufficiently low Reynolds number, the jet expands monotonically downstream, so $v > 0$ near the nozzle edge. Combined with $\partial(rv)/\partial r < 0$, this implies the local presence of a compressional radial viscous stress immediately downstream of the nozzle, $\tau_{rr} < 0$ (as indeed observed from Fig. 4.6b). From Eq. (4.12a) we thus find that for low Re, the normal viscous stress acting on the free surface is negative immediately downstream of the nozzle edge, $\mathbf{n} \cdot \tau \cdot \mathbf{n} < 0$. From Eq. (4.7a) and assuming that surface tension is negligible, we then find that the pressure must locally decrease to maintain equilibrium with the atmospheric pressure of the ambient gas. This can only be accomplished by expansion of the jet, which will reduce the local drop in the pressure and reduce the magnitude of the compressional normal viscous stress acting on the jet interface.

The above reasoning provides a conceptual explanation for the monotonic jet expan-

sion observed for low Re. The change from a no-slip to a free-slip condition for the flow leaving the nozzle, generates axial viscous stresses, which through mass conservation are responsible for a compressional radial stress at the jet interface, by which the interface is pushed outwards to maintain stress equilibrium with the ambient gas at atmospheric pressure. At higher Re, inertial effect come into play and the jet first undergoes a contraction when leaving the nozzle. The conceptual picture for the Stokes regime breaks down in this case as local flow acceleration (near the nozzle edge) and flow deceleration (near the centerline) will likely influence the pressure distribution inside the jet downstream of nozzle exit.

The compressional axial viscous stress near the centerline of the nozzle exit plane and the extensional axial viscous stress near the nozzle edge are responsible for a more blunted velocity profile immediately upstream of the exit plane with respect to parabolic Poiseuille flow. This will both affect the streamwise pressure gradient and the wall shear stress at the nozzle wall. To quantify the streamwise extent of the affected nozzle region, we define the "upstream diffusion length", L_{UD}, as the position $x = -L_{UD}$ where the centerline velocity is within 1% of the centerline velocity of homogeneous Poiseuille profile. Similarly, we also introduce the "downstream velocity relaxation length" as the position $x = L_P$ where the centerline velocity and the velocity at the interface become equal (i.e., plug flow). The numerical results for L_{UD}/R and L_P/R are shown in the inset of Fig. 4.7 as function of Re. Interestingly, over the investigate Re-range, the variation in the length scales is approximately linear in Re and given by, respectively:

$$L_{UD}/R \approx -7.2 \times 10^{-3} Re + 0.75 \tag{4.19a}$$

$$L_P/R \approx 0.15 Re + 1.05 \tag{4.19b}$$

While at the very low Reynolds numbers, the ratio L_{UD}/L_P is $O(1)$, the ratio quickly drops with increasing Re and will eventually approach zero for high Re in the inertia-dominated regime.

In the inset of Fig. 4.8 the normalised deviation of the centerline velocity at nozzle exit from Poiseuille flow, $(2U_b - u(0,0))/2U_b$, is shown as function of Re. Interestingly, the deviation of the centerline velocity from Poiseuille flow can be parameterized by $2U_b - u(0,0) \approx \alpha 2 U_b Re^{-2/3}$ with $\alpha \approx 0.36$. This motivated us to rescale the centerline velocity profiles of Fig. 4.7 according to: $(u(x,0) - u(0,0))Re^{2/3}/2U_b$. The profiles of the normalised centerline deficit velocity are depicted in Fig. 4.8. Scaled in this manner the centerline velocity upstream and downstream of the nozzle till $x/R \approx 0.25$ shows a nearly perfect collapse for all investigated Re. The observed self-similarity indicates that the centerline velocity upstream of the nozzle exit can be written as:

$$u(x,0) = 2U_b \left[1 - Re^{-2/3} (\alpha - f(x/R)) \right], \tag{4.20}$$

where $f(x/R)$ is the self-similar profile depicted in Fig. 4.8 for $x/R < 0$. From this expression we can also derive the following expression for the axial viscous stress at the centerline:

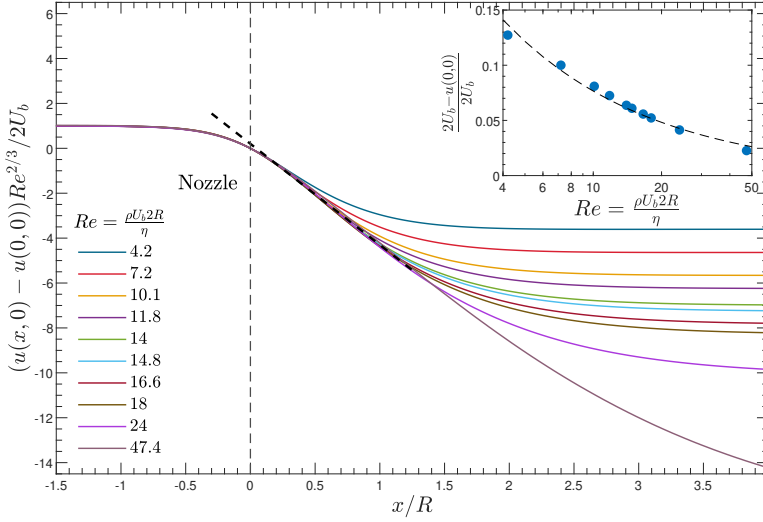$$\tau_{xx}(x,0) = \frac{4\mu U_b}{R} Re^{-2/3} f'(x/R), \tag{4.21}$$

Figure 4.8: Normalised centerline deficit velocity with respect to the centerline velocity at nozzle exit, $(u(x,0) - u(0,0))Re^{2/3}/2U_b$, shown as function of streamwise distance and Re. (inset) Deviation of centerline velocity at nozzle exit from Poiseuille flow, as function of Re.

where $f' < 0$ is the derivative of f with respect to x/R and $O(-1)$.

From the simulation data we can directly evaluate $\tilde{K}$ in Eq. (4.16b), i.e., the contribution from viscous effects to the jet contraction ratio. To further analyse this, we write $\tilde{K}$ as:

$$\tilde{K} = P_{exc} + T_{exc} \tag{4.22}$$

Here P_{exc} is referred to as the integral excess pressure and T_{exc} as the integral excess stress, defined as, respectively:

$$P_{exc} = \int_0^1 \left(\tilde{p}|_{x=-\tilde{L}_{UD}} - \tilde{p}_{atm} - \Delta\tilde{p}^H \right) 2\tilde{r} \, d\tilde{r} \tag{4.23a}$$

$$T_{exc} = \frac{4}{Re} \int_{-\tilde{L}_{UD}}^0 \left(\tilde{\tau}_{xr}|_{\tilde{r}=1} - \tilde{\tau}_{xr}^H|_{\tilde{r}=1} \right) d\tilde{x} \tag{4.23b}$$

where $\Delta\tilde{p}^H = (16/Re)\tilde{L}_{UD}$ is the non-dimensional pressure drop over the nozzle in case of homogeneous Poiseuille flow inside the nozzle, and $\tilde{\tau}_{xr}^H = -4$ is the corresponding non-dimensional wall shear stress. Note that $\int_0^1 \Delta\tilde{p}^H 2\tilde{r} d\tilde{r} = -\frac{4}{Re}\int_{-\tilde{L}_{UD}}^0 \left(\tilde{\tau}_{xr}^H|_{\tilde{r}=1} \right) d\tilde{x}$ is the force balance between the driving pressure gradient and the wall shear stress for homogeneous Poiseuille flow. When axial viscous stresses are significant in the region directly upstream of the nozzle exit plane, the flow will not be homogeneous anymore. The axial viscous stresses will partially decouple the pressure gradient from the wall shear stress and this suggests a less strong pressure drop than for homogeneous Poiseuille flow, thus a negative integral excess pressure is expected. Similarly, the extensional axial

stress near the nozzle wall will cause an increase in the magnitude of the wall shear stress with respect to homogeneous Poiseuille flow, thus also a negative integral excess stress is expected.
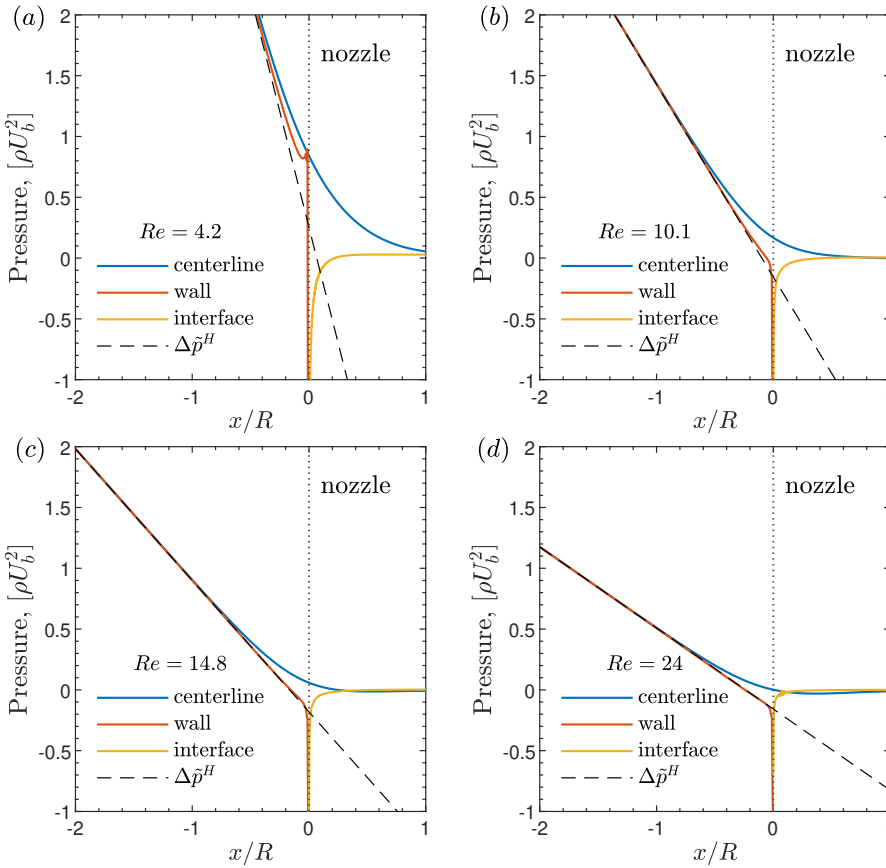

Figure 4.9: Pressure distributions close to the nozzle exit for (*a*) *Re* = 4.2, (*b*) *Re* = 10.1, (*c*) *Re* = 14.8 and (*d*) *Re* = 24. The dashed line denotes the homogenous pressure drop expected from the Poiseuille profile.

Figure 4.9 show the pressure variation along the centerline, the wall and at the free surface of the jet. While upstream inside the nozzle, the pressure profile follows the homogenous Poiseuille profile, the centerline and the wall pressure distributions deviate from that closer to the nozzle exit. One can thus also note the radial pressure gradient that arises at the nozzle exit plane, which is an adjustment of the flow to the sudden change from no-slip to free-slip condition from the nozzle wall to the jet interface.

The contributions from the integral excess pressure and integral excess stress to the viscous term $\tilde{K}$ in the polynomial equation for χ are shown in Figure 4.10(*a*) as a function of the Reynolds number. As proposed by Joseph [8] and shown in Eq. (4.17), $\tilde{K}$ scales with $Re^{-2/3}$ for $Re > 10$. Note that for $Re < 10$ the Weber number also goes down (see Ta-

ble 4.1), making the surface tension influence bigger on the flow. This is highlighted in Figure 4.10(*b*) where the contraction ratio is computed from the integral momentum balance given in Eq.(4.16) with and without the surface tension terms. One can note that the largest deviation occurs in the lower Reynolds numbers (hence lower Weber numbers) where capillary effects are more significant. This is also consistent with the relation given in Eq. (4.18), and depicted in Fig. 4.5(*a*), which agrees well with the computed and observed contraction ratio above $Re > 10$. We observe from Fig. 4.10(*a*) that the integral excess pressure is the dominant contribution to $\tilde{K}$ for $Re \gtrsim 10$, while the integral excess stress is the dominant contribution for $Re \lesssim 10$. Finally, the sign change in the integral excess pressure at low Reynolds
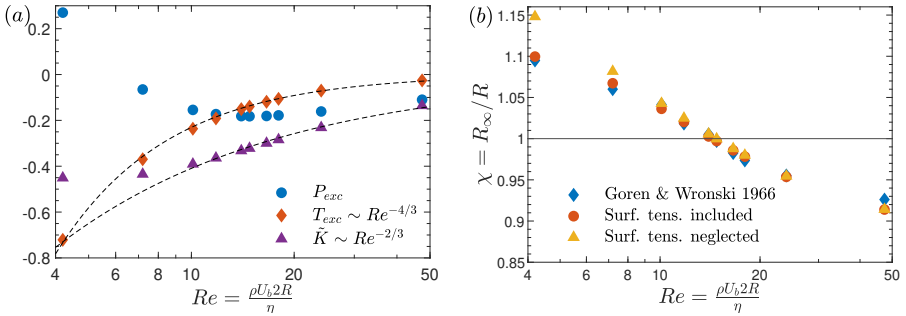

Figure 4.10: (*a*) $\tilde{K}$, P_{exc} and T_{exc} as a function of Reynolds number (*b*) The contraction ratio computed from integral momentum balance with and without the surface tension terms, compared against the results of Goren & Wronski [9]

4.5. CONCLUSION

We presented simulations of a laminar axisymmetric jet of a Newtonian liquid issued from a long circular nozzle into a gaseous environment. After the experiments of Goren & Wronski [9], ten cases have been selected with different Reynolds numbers. Our numerical results for the spatially varying jet radius are in good agreement with the experiments. Non-monotonic behavior is observed for the jet radius as function of streamwise distance for $Re \approx 10 - 14$, where the jet first contracts directly after nozzle exit but then expands towards a final diameter beyond the initial jet radius. Whereas the jet contracts towards a smaller equilibrium radius for $Re \gtrsim 14$, a monotonic expansion is found for $Re \lesssim 10$. Our results suggest that the expansion of the jet for small Re originates from a compressional radial viscous stress at the jet interface immediately downstream of nozzle exit.

Self-similar behavior is found for the axial centerline velocity, which holds not only within the nozzle but even outside the nozzle up to $x/R \approx 0.25$ for the present range of Re investigated. The self-similar solution implies that the associated compressional axial stress at the centerline scales with $Re^{-2/3}$ when normalized with $\mu U_b/R$. The stress reduces to zero in the upstream direction at a distance of $\approx 0.75R$ from the nozzle exit plane. This thus indicates the extent of the region within the nozzle that is affected by

the sudden change from a no-slip to a free-slip flow boundary condition at the nozzle exit.

We derived a polynomial equation for the jet contraction ratio χ using integral mass and momentum balances. The coefficients of the equation have been evaluated from the numerical simulation data. The jet contraction ratio computed from this equation is in very good agreement with the actual contraction ratio directly obtained from the simulations as well as the experimental data of Goren & Wronski [9]. From this equation we also found that surface tension has a non-negligible influence on the jet expansion for $Re \lesssim 10$, and is responsible for a less strong expansion compared to the sole effect of viscosity. At $Re = 4.2$ the increase in the equilibrium jet radius, relative to the initial jet radius, drops from approximately 15% to about 10%.

The normalized viscous contribution to the polynomial equation for the jet contraction ratio, scales with $Re^{-2/3}$ for $Re \gtrsim 10$, in agreement with the scaling originally proposed by Joseph [8]. The decomposition of the viscous contribution into an integral excess pressure and an integral excess stress shows that both are negative (except at $Re = 4.2$). While the excess viscous stress is dominant over the excess pressure for $Re \lesssim 14$, the opposite holds for $Re \gtrsim 14$. The deviation of the simulation data from Joseph' correlation for the viscous contribution is, at least partially, attributed to a surface tension effect and the direct influence thereof on the pressure inside the jet, which was neglected by Joseph.

A logical extension of the present work would be to investigate if a self-similar solution exists for the entire flow field within the nozzle. The self-similar solution found for the axial centerline velocity suggests that this is indeed possible. The $Re^{-4/3}$ scaling observed for the integral excess stress in Fig. 4.10a further hints in this direction. From the self-similar solution for the flow field in the nozzle, a correlation may be derived for the viscous contribution to the jet contraction ratio for $Re \lesssim 10$ for which the correlation of Joseph breaks down. It is also recommended to further explore the influence of the Weber (or Capillary) number as we found that surface tension has a non-negligible on the lower Re range in the experiments of Goren & Wronski [9].

The findings of the present study have significant implications for the breakup of thin liquid jets in prilling applications. In studies of jet breakup it is often implicitly assumed that the flow within the base jet is uniform and that the jet radius is constant and equal to the radius of the nozzle from which the jet is issued. The present work shows that the upstream flow conditions and nozzle geometry matter. For a long nozzle with a parabolic velocity profile sufficiently far upstream, the jet significantly contracts at the Reynolds numbers typical for prilling applications. Since a jet breaks up at a length scale proportional to the base jet radius, this thus has consequences for the optimal perturbation frequency for jet breakup and the resultant droplet and prill size distributions. For practical applications, it is therefore highly recommended to study upstream flow and nozzle geometry effects on the base jet flow.

4

REFERENCES

[1] U. S. SAUTER and H. W. BUGGISCH. "Stability of initially slow viscous jets driven by gravity". In: *Journal of Fluid Mechanics* 533 (2005), pp. 237–257. DOI: 10.1017/S002211200500412X.

[2] H. Giesekus. "Verschiedene phänomene in strömungen viskoelastischer flüssigkeiten durch düsen". In: *Rheologica Acta* 8 (1969), pp. 411–421.

[3] D. B. Harmon. "Drop sizes from low speed jets". In: *Journal of the Franklin Institute* 259.6 (1955), pp. 519–522. ISSN: 0016-0032. DOI: https://doi.org/10.1016/0016-0032(55)90098-3. URL: https://www.sciencedirect.com/science/article/pii/0016003255900983.

[4] S. Middleman and J. Gavis. "Expansion and contraction of capillary jets of Newtonian liquids". In: *The Physics of Fluids* 4.3 (1961), pp. 355–359.

[5] J. Batchelor, J. Berry, and F. Horsfall. "Die swell in elastic and viscous fluids". In: *Polymer* 14.7 (1973), pp. 297–299.

[6] Y. E. Kamis, S. Prakash, W.-P. Breugem, and H. B. Eral. "Controlling the breakup of spiralling jets: results from experiments, nonlinear simulations and linear stability analysis". In: *Journal of Fluid Mechanics* 956 (2023), A24.

[7] J. Eggers and E. Villermaux. "Physics of liquid jets". In: *Reports on Progress in Physics* 71.3 (2008), p. 036601.

[8] D. D. Joseph. "Slow motion and viscometric motion; stability and bifurcation of the rest state of a simple fluid". In: *Archive for Rational Mechanics and Analysis* 56.2 (1974), pp. 99–157.

[9] S. L. Goren and S. Wronski. "The shape of low-speed capillary jets of Newtonian liquids". In: *Journal of Fluid Mechanics* 25.1 (1966), pp. 185–198.

5

APPLICATION TO INDUSTRIAL PRILLING PROCESSES

The prilling process involves strongly coupled multiphysics phenomena, including thin jets of a molten substance emitted from a perforated rotating bucket (from here on named "priller"), the breakup of the jets into drops, and prill formation by rapid cooling and crystallization of the drops as they fall down the prilling tower. In chapter 1, we identified four main research questions that were motivated by the process of prilling, where the first three research questions were addressed in chapters 2,3 and 4, respectively. We developed theoretical and computational tools for studying the dynamics of isothermal spiralling and nonisothermal straight jets in a computationally cheap manner, from which we gain detailed insight in , respectively, the influence of rotation and thermal perturbations on jet breakup. In chapter 2, an experimental setup to study the dynamics of spiralling jets was presented and control the breakup of spiralling jets using perturbations was studied by means of experiments and simulations. The spiralling jet simulation based on the nonlinear slender jet framework, isolates the jet dynamics from all the flow history upstream the nozzle, and assumes a given nozzle exit velocity and a velocity perturbation with a given amplitude at a single dominant frequency or with a white noise spectrum. The success of the slender jet framework in reproducing the dynamics observed in the experiments detailed in chapter 2, encourages the thought of using this modelling approach for predictions of the process output (prill size distribution) in an industrial prilling process. In this chapter we will discuss the first steps of using the existing model for some industrial scale case studies and discuss the limitations of the existing modelling approach along with recommendations for improvement.

5.1. SIMULATION TOOLS DEVELOPED WITHIN THE THESIS

In chapters 2 & 3, an in-house simulation tool based on the slender jet approximation is presented and utilized. In chapter 2, this model was extended with a preliminary routine for estimating the base flow trajectory of the spiral jet. The background of this model is briefly repeated here for convenience.

The centerline trajectory is represented by the Cartesian coordinates, $X(s)$, $Y(s)$, and $Z(s)$, with s the arc length with respect to nozzle exit. X, Y, Z and s are all normalized with the rotating arm, L, of the nozzle. The local jet velocity is denoted by $U(s)$ and normalized with the base jet velocity at nozzle exit, U_0. The local jet radius is denoted by R and is normalized with the based jet radius at nozzle exit, R_0. Assuming that radial (cross-stream) variations are much weaker than axial variations in the base flow, $R_0/L \ll 1$, the following equations can be derived for the base jet:

$$\frac{d}{ds}\left(UR^2\right) = 0, \tag{5.1}$$

$$U\frac{dU}{ds} = -\frac{1}{We}\frac{d}{ds}\left(\frac{1}{R}\right) + \frac{3}{R^2 Re}\frac{d}{ds}\left(R^2\frac{dU}{ds}\right) \underbrace{-\frac{Z'}{Fr^2}}_{f_{gravity}} + \underbrace{\frac{XX' + YY'}{Rb^2}}_{f_{centrifugal}}, \tag{5.2}$$

$$\left(U^2 - \frac{1}{RWe} - \frac{3}{Re}\frac{dU}{ds}\right)\left(X''^2 + Y''^2 + Z''^2\right) = \frac{XX'' + YY''}{Rb^2}$$
$$- \frac{2U\left(X'Y'' - Y'X''\right)}{Rb} - \frac{Z''}{Fr^2}, \tag{5.3}$$

$$0 = \frac{X\left(Y'Z'' - Z'Y''\right) + Y\left(Z'X'' - X'Z''\right)}{Rb^2} - \frac{X'Y'' - Y'X''}{Fr^2} + \frac{2UZ''}{Rb}, \tag{5.4}$$

$$X'^2 + Y'^2 + Z'^2 = 1, \tag{5.5}$$

where $Re = \frac{\rho U_0 R_0}{\eta}$, $We = \frac{\rho U_0^2 R_0}{\gamma}$, $Rb = \frac{U_0}{\Omega L}$ and $Fr = \frac{U}{\sqrt{gL}}$ are the Reynolds, Weber, Rossby and Froude number respectively. In the inviscid limit ($Re \gg 1$) Equation (5.2) can be integrated as:

$$U^2 + \frac{2U^{1/2}}{We\sqrt{C_1}} + \frac{2}{Fr^2}Z - \frac{1}{Rb^2}\left(X^2 + Y^2\right) + C_2 = 0, \tag{5.6}$$

where we used $UR^2 = C_1$ from Eq. (5.1), and C_1 and C_2 are integration constants. Note that viscous resistances to bending and twisting are also neglected in this case. We define $X(0) = 1$, $Y(0) = 0$, $Z(0) = 0$, $X'(0) = 1$, $Y'(0) = 0$ and finally $Z'(0)$ follows from Eq. (5.5). By definition, also $U(0) = R(0) = 1$ and hence $C_1 = 1$. Substituting all the prescribed boundary conditions in Eq. (5.6) yields $C_2 = 1/Rb^2 - 2/We - 1$.

The system of equations (5.1), (5.3)-(5.6), also known as the "string" equations, describe the steady state trajectory and the base flow (flow without the perturbations) of the spiralling jet. This set of equations is solved using a fourth-order Runge-Kutta method. Figures 5.1(a) and (b) show, respectively, the computed baseline trajectory and

the base jet velocity and radius for $We = 18.2$, $Rb = 0.95$ and $Fr = 2.16$. The base jet trajectory is in excellent agreement with the experiments, so it enables the quantification of the projections of the body forces along the trajectory, namely, the centrifugal force, $f_{centrifugal}(s)$, and gravity force, $f_{gravity}(s)$, whose expressions are given at the right hand side of (5.2). Figure 5.1(c) depicts the computed forces from the base flow calculations. It is apparent that with the parameters in our experiment, the gravity force is about an order of magnitude smaller than the centrifugal force, which suggests that the torsion along the arc length and distance travelled by the jet in the vertical Z direction are negligibly small in this case, allowing to study the dynamics from 2D projections onto the XY-plane.
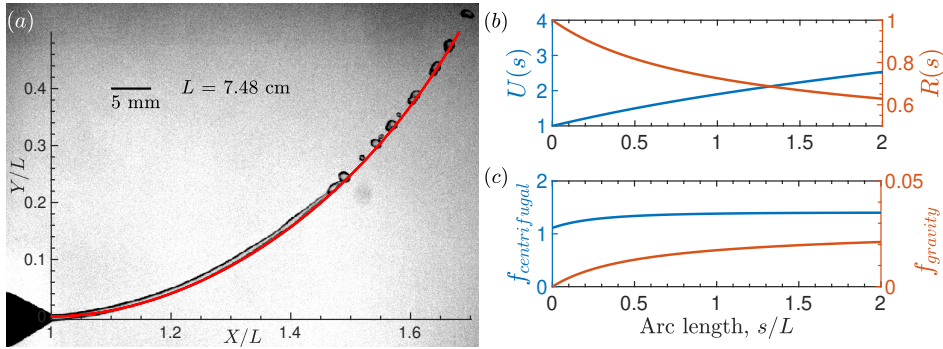

Figure 5.1: Results from the base flow calculation for $We = 18.2$, $Rb = 0.95$ and $Fr = 2.16$. (a) Comparison of calculated jet trajectory (red line) with a snapshot from an unperturbed jet experiment with $L = 7.48$ cm rotating arm at the nozzle exit and $R_0 = 400\,\mu$m. (b) The variation of the base state velocity, $U(s)$, and jet radius, $R(s)$, along the jet. (c) The variation of the body forces per unit mass (and normalised with U_0^2/L) acting along the jet due to rotation $f_{centrifugal} = (XX' + YY')/Rb^2$ and gravity $f_{gravity} = -Z'/Fr^2$.

The calculated base flow trajectory and jet velocity and radius, are used as input for the non-linear slender-jet model to simulate the streamwise evolution of a prescribed velocity perturbation at nozzle exit and the related breakup of the spiralling jet into main and satellite drops. The slender-jet approximation is a well-established and validated approach to study jet instabilities, given that the jets are sufficiently "slender", i.e., radial (cross-stream) variations are much weaker than axial variations in the perturbation flow. This drops down to the requirement that $\epsilon = R_0/L \ll 1$, consistent with the assumption used for deriving the string equations for the base jet. One can find details and benchmarks of this approach in [1–4]. The novelty of our approach in using this framework for spiralling jets, is as follows. Once the longitudinal projections of the centrifugal and the gravity forces are accounted for, one can approximate the nonlinear dynamics of the jet along the flow direction with an error of $O(\epsilon)$, provided that the full free surface curvature is accounted for [5]. In other words, the 3D spiralling trajectory of the jet can be represented as a quasi-straight jet with locally varying body forces. This also amounts to the implicit assumption that that the wavenumber of the perturbations k (scales with

R_0^{-1}) is much larger than the curvature κ and the torsion τ of the base jet trajectory (both scale with L^{-1}) which is valid in the limit $\epsilon \to 0$.

The resulting set of 1D unsteady equations is as follows:

$$\frac{\partial A}{\partial t} + \frac{\partial}{\partial s}(uA) = 0, \tag{5.7a}$$

$$\frac{\partial (uA)}{\partial t} + \frac{\partial}{\partial s}\left(u^2 A\right) = \frac{\partial}{\partial s}\left[A\left(\frac{K}{We} + \frac{3\epsilon}{Re}\frac{\partial u}{\partial s}\right)\right] + A\left[\epsilon\left(f_{centrifugal} + f_{gravity}\right)\right], \tag{5.7b}$$

$$K = \frac{2}{\sqrt{4A + A_s^2}} + \frac{4AA_{ss} - 2A_s^2}{\left(4A + A_s^2\right)^{3/2}}, \tag{5.7c}$$

where $A = R^2$ is the normalized local jet cross-sectional area. Note that the full expression for the curvature is used (i.e., both radii of curvature instead of only the leading order one in the expansion). This is key to the success of the slender jet framework [6, 7].

Note the inclusion of the ϵ parameter in front of the centrifugal and gravity force in (5.7b) as they have been taken from (5.2) and hence are normalised with L instead of R_0. Equations $(5.7)(a) - (c)$ form a closed system of equations for the jet cross-sectional area $A(s, t)$ and jet velocity $u(s, t)$. The initial conditions are implemented as $A(s, 0) = R(s)^2$ and $u(s, 0) = U(s)$ from the base flow computations.

Mechanical vibrations are naturally present in industrial applications of spiralling jets such as in prilling, where the typical size of the rotating perforated bucket is on the order of 50 cm. Even in small-scale laboratory experiments, one can never get fully rid of such vibrations, and they might have a significant effect on the jet breakup. The time series of such noisy perturbations are rather difficult to quantify, however, a good proxy is to represent the vibrations by white noise and to characterize the noise strength in terms of the natural (actuation-free) jet breakup length or breakup time [8].

To simulate the natural breakup in the slender-jet framework, we add Gaussian white noise to the nozzle velocity as follows:

$$u(0, t) = 1 + \underbrace{\varepsilon_v \cos(\omega t)}_{\text{perturbation}} + \underbrace{W(\Delta t)}_{\text{white noise}}. \tag{5.8}$$

The white noise is generated using standard random number generators in Matlab and its standard deviation scales as $S\Delta t$ where S is a strength parameter and Δt is the computational timestep. This ensures that the forcing due to the white noise, related to the velocity change over a time step Δt, is uncorrelated with the timestep [4]. The strength parameter S is then calibrated using the observed experimental natural (i.e., $\varepsilon_v = 0$) breakup length. In our study we used $S = 300$ in all simulations and the nondimensional timestep Δt is adjusted dynamically considering the stability restrictions based on the effects of advection, diffusion and surface tension [9, 10].

A regularized capillary pressure is implemented to carry the simulations beyond the pinchoff point [11]. A finite difference scheme on a staggered grid is used for solving the system given in Eqs. $5.7(a) - (c)$. The time integration is done explicitly by using a three-step Runge-Kutta scheme with an adaptive time stepping. Except for velocities, a central differencing scheme is used for evaluating the variables at their half step neighbors. For

advection terms, a higher-order total variation diminishing (TVD) van Leer scheme is used. More details of the numerical method and validation can be found in [4].

The comparison of the simulation and experiments for the parameters listed in table 2.1 is shown in Figure 5.2. Results for jet breakup and drop projected area onto the XY-plane in the presence of only background noise, are presented in Table 5.1. Overall the experiments and numerical simulations are in good agreement.

	Simulation	Experiment
Breakup length, L_b/R_0	98.0 ± 6.0	95.4 ± 7.8
Drop projected area, A_p/R_0^2	6.7 ± 3.8	8.3 ± 5.4

Table 5.1: Mean and standard deviation of the breakup properties of natural (actuation-free) breakup cases.
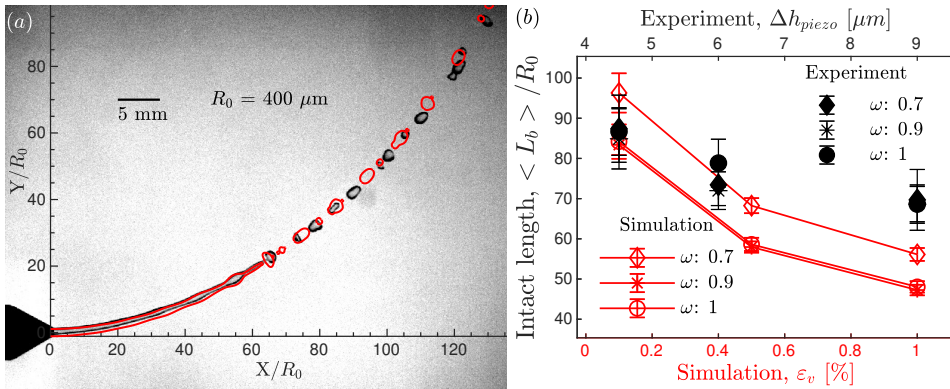

Figure 5.2: (*a*) Comparison of the jet interfaces obtained from simulation (shown in red) and from experiment at a perturbation frequency $\omega = 0.7$. The piezoplate displacement is $6\,\mu m$ and the velocity amplitude in the simulation is 0.5% (*b*) Mean and standard deviation of the jet intact length as function of piezoplate displacement in the experiments and velocity perturbation amplitude in the simulations.

5.2. KNOWLEDGE UTILIZATION AT INDUSTRIAL SCALE

We have demonstrated that the above mentioned approach is able to predict the dynamics of a single spiralling jet at laboratory scale and laboratory conditions. To apply our modelling framework to industrial prilling processes, one needs to look back at the priller, which is the heart of the prilling process. A priller can be considered as a collection of around 10^4 nozzles. A typical priller contains a slanted wall such that the jets emitted from the bottom reach less far than the jets emitted from the top in order to optimally exploit the space of the prilling tower. However, an important implication

of this is that in the steady state operation, a distribution of physical parameters exists along the wall of the priller. The working material will have a given density, viscosity and surface tension (temperature dependency and non-Newtonian effects are neglected for convenience). So the main causes of variations among the jets, are the varying geometric parameters along the priller, namely the variation in the rotating arm along the priller, and the nozzle radius distribution along the priller. The combination of these two factors is responsible for a variation of nozzle exit velocity along the priller. Fig. 5.3 shows a sketch of a typical priller and the potential distribution of these parameters along the priller wall. Associated with this is also a variation of the nondimensional numbers that governing the dynamics of a spiralling jet:

$$We(z) = \frac{\rho U_0^2(z) R_0(z)}{\gamma} \quad Rb(z) = \frac{U_0(z)}{\Omega L(z)} \quad Fr(z) = \frac{U_0(z)}{\sqrt{g L(z)}} \tag{5.9}$$
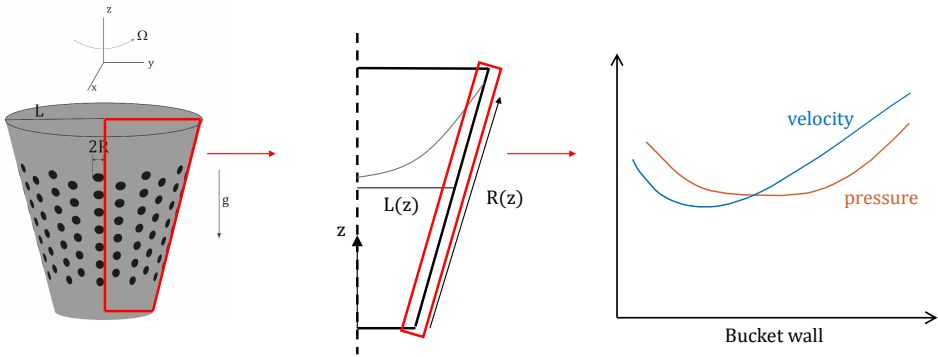

Figure 5.3: Sketch of a typical industrial priller, with an increase in the rotating arm and hole size from bottom to top.

An estimation the total yield from a prilling process requires to integrate the yield from the individual jets over the height of the priller. Figure 5.4(a) illustrates the distribution of the liquid pressure directly upstream of the priller holes and the corresponding outward velocity distribution. Using Eq. (5.9), this was used to compute the variation in the governing non-dimensional numbers, which is depicted in Fig. 5.4(b). While the variation in Rb and Fr is relatively small, We varies by almost a factor two over the priller height. This implies a significant change in the jetting and breakup dynamics, which need to be considered for an accurate estimation of the total yield from the priller. Figure 5.5 illustrates the base jet trajectories across the height of the priller, computed from the variation in governing dimensionless numbers. This can now be used as input for the slender-jet model to calculate the breakup of the jets and subsequent drop formation. To limit the computational load, this is done only for a limited number of heights, but sufficient to capture the variation in the jet breakup dynamics.

Here, the implicit assumption is that the dynamics of the jets at the same height are identical and that the jets do not influence each other. So the spiralling jet simulation
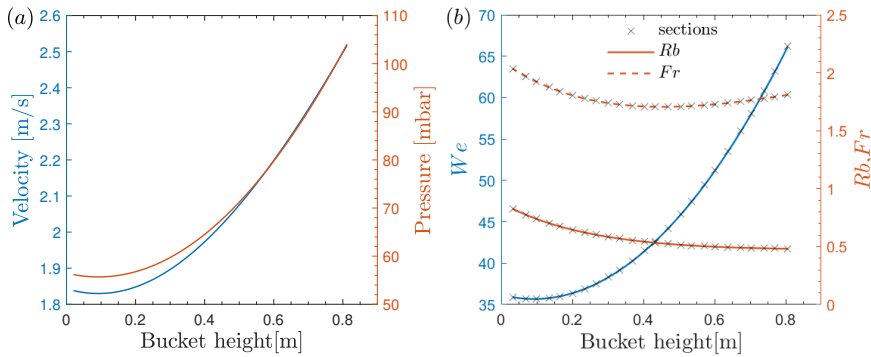
Figure 5.4: Variation in flow conditions at the exit holes of prilling bucket as function of height along the priller. (*a*) Outward velocity and pressure at the priller holes. (*b*) Variation in governing non-dimensional numbers, defined by Eq. (5.9), as function of height. The × symbols mark the sampled heights in the simulations to obtain an estimate of the total yield from the priller.
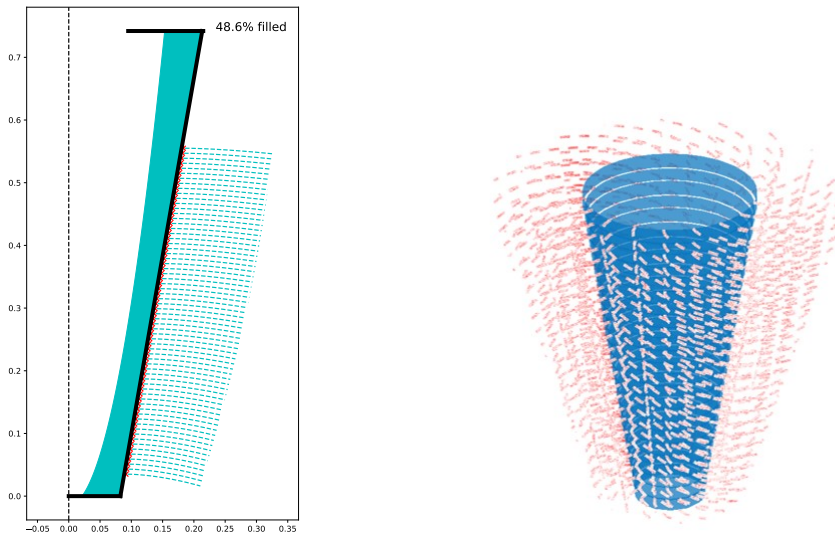

Figure 5.5: Side and 3D view of the expected trajectories of the jets emerging from the priller. The red region in the side view shows the vortex inside the priller formed by the melt.

framework explained in Chapter 2 and briefly revisited in §5.1 of this chapter, is simply a subroutine or a building block for a holistic approach of simulating the jet dynamics and resulting prill size distribution from a priller. Figure 5.6 illustrates the breakup of spiralling jets from a number of bucket holes at a given bucket height and time. Note that the thermal effects and solidification/crystallization have not been taken into account

in these simulations. Instead, an estimate of the solidification time is made following the design procedure given in [12] and jet arc length is determined using the jet velocity and solidification time estimate. After running the simulations for all (or some) of
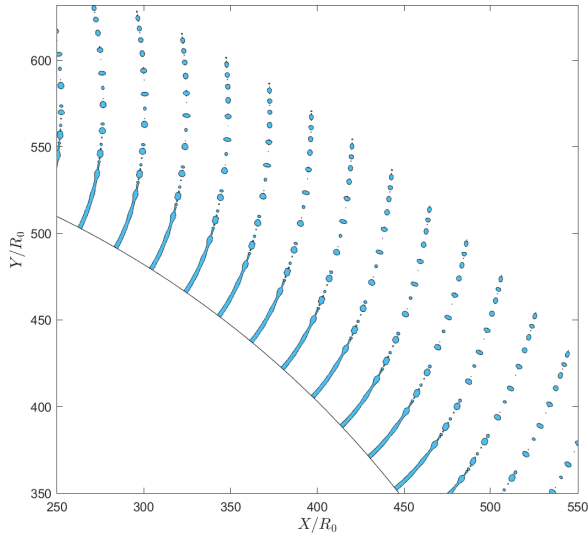

Figure 5.6: Top view of a transverse cross section of a priller with multiple jets

the cross-sectional rings of the priller, one can analyze the jet intact length and the drop size distributions to get an estimate of the yield. Figure 5.7 shows a typical outcome of the results of modelling a priller under a perturbation given by Eq.5.8 with $\omega = 0.8$ and $\varepsilon_v = 0.1$ using the slender-jet framework. One of the objectives of controlling prill production is to eliminate the formation of dust as much as possible. How dust is defined, may change depending on the working material, but one can analyze the model results to estimate what percentage of the yield would be classified as dust, and change the operation and/or perturbation parameters accordingly to achieve the desired levels.

5.3. Limitations and recommendations

The above explained approach for using the developed slender-jet model to estimate the yield of a large scale prilling process with a priller that contains around $O(10^4)$ nozzles, relies on several assumptions, which need to be validated, otherwise an extension to the existing model is necessary. The numerical model contains no information about the upstream history of the flow at the nozzle, it takes a uniform plug flow as flow condition at the nozzle exit with the addition of a sinusoidal perturbation and Gaussian white noise (see Eq.(5.8)). In the case of a priller, however, the flow inside the priller is far from being uniform. Typically, the prillers contain additional interior walls and structures related to dealing with melts, and the flow inside the priller is sloshing and turbulent. The axial hole length is not sufficiently long such that these upstream fluctuations are damped by viscosity and for the flow inside the nozzle to reach a fully developed profile. To connect
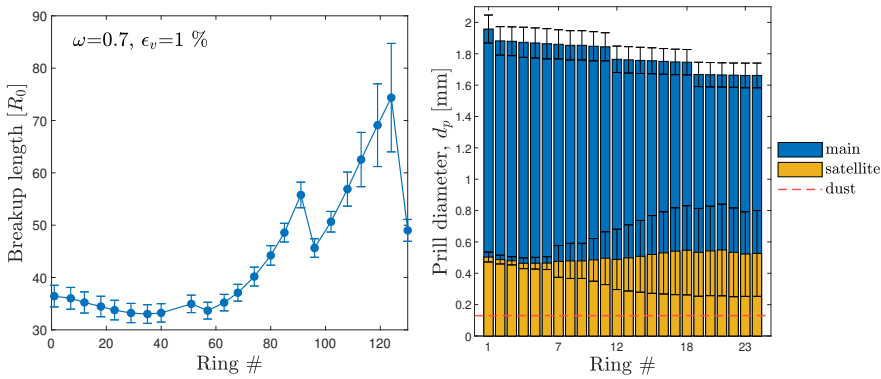
Figure 5.7: Jet intact lengths and drop/prill size distributions obtained from different cross sections at the priller.

the upstream part to the numerical tool developed here, one needs to carefully assess the unsteady pressure and velocity profile near the nozzles in the priller, either by means of measurements or detailed CFD. Incorporating such effects in our model will most likely increase the fidelity of the approach described here.

Another assumption that is embedded in our approach, is that the priller is represented as an independent collection of nozzles, so this approach can be used independently for the nozzles and then can be superposed. That means the nozzles and jets do not interact with each other. This is hardly true, as clogging is a major issue in prilling and it affects the performance of the priller, so the jets are indeed coupled through the flow inside the priller. In addition, the jets can be influenced by the strong cooling air flow inside the prilling tower and can be aerodynamically interacting with each other. In the lab scale experiments with a single jet, we validated that the air drag has negligible influence, but this needs to be further validated for the industrial scale with the presence of thousands of jets. If necessary, the model needs to be extended to account for aerodynamic forces acting on the jets.

5

REFERENCES

[1] J. Eggers. "Universal pinching of 3D axisymmetric free-surface flow". In: *Phys. Rev. Lett.* 71.21 (1993), p. 3458.

[2] J. Eggers and T. F. Dupont. "Drop formation in a one-dimensional approximation of the Navier–Stokes equation". In: *Journal of Fluid Mechanics* 262 (1994), pp. 205–221.

[3] D. S. Pillai, P. Narayanan, S. Pushpavanam, T. Sundararajan, A. Jasmin Sudha, and P. Chellapandi. "A nonlinear analysis of the effect of heat transfer on capillary jet instability". In: *Physics of Fluids* 24.12 (2012), p. 124106.

[4] Y. E. Kamis, H. B. Eral, and W.-P. Breugem. "Active control of jet breakup and droplet formation using temperature modulation". In: *Physical Review Fluids* 6.10 (2021), p. 103903.

[5] Y. Li, G. M. Sisoev, and Y. D. Shikhmurzaev. "On the breakup of spiralling liquid jets". In: *Journal of Fluid Mechanics* 862 (2019), pp. 364–384.

[6] V. Entov and A. Yarin. "Influence of elastic stresses on the capillary breakup of jets of dilute polymer solutions". In: *Fluid Dynamics* 19.1 (1984), pp. 21–29.

[7] B. Ambravaneswaran, E. D. Wilkes, and O. A. Basaran. "Drop formation from a capillary tube: Comparison of one-dimensional and two-dimensional analyses and occurrence of satellite drops". In: *Physics of Fluids* 14.8 (2002), pp. 2606–2621.

[8] W. T. Pimbley and H. C. Lee. "Satellite droplet formation in a liquid jet". In: *IBM Journal of Research and Development* 21.1 (1977), pp. 21–30.

[9] P. Wesseling. *Principles of computational fluid dynamics*. Springer Science & Business Media, 2009.

[10] J. U. Brackbill, D. B. Kothe, and C. Zemach. "A continuum method for modeling surface tension". In: *Journal of Computational Physics* 100.2 (1992), pp. 335–354.

[11] T. Driessen and R. Jeurissen. "A regularised one-dimensional drop formation and coalescence model using a total variation diminishing (TVD) scheme on a single Eulerian grid". In: *International Journal of Computational Fluid dynamics* 25.6 (2011), pp. 333–343.

[12] C. M. Van't Land. *Industrial Crystallization of Melts*. CRC Press, 2004.

6

CONCLUSIONS & RECOMMENDATIONS

The research questions formulated in Chapter 1 have been addressed in several chapters in this thesis. In this chapter we will revisit these research questions and summarize the main findings of this thesis in an effort to answer them.

- **What physical mechanism dictates the breakup of a jet and formation of drops in the presence of jet rotation (i.e., a spiralling jet)? How can the breakup of spiralling jets be modelled? What is the effect of the frequency and amplitude of mechanical excitation of the jet on breakup? How can the size distribution of the drops be controlled?**

  In Chapter 2, the operating window of these Rayleigh-Plateau modes for spiralling jets were investigated. We show that spiralling jets can be modeled as "quasi-straight jets" with a locally varying pulling force, similar to jets falling under gravity. The model is validated with in-house experiments. This approximation holds when the cross-sectional scale of the jet (approximately the jet radius) is significantly smaller than the longitudinal scale at which the base flow changes. The locally varying body forces are the longitudinal components of the centrifugal and gravity forces along the jet. In our studied nondimensional parameter set, these longitudinal projections can be simplified as a constant effective gravity, allowing the base flow solution to be treated as a freely falling jet through the definition of an effective Bond number. The stretching of the wavelength results in a decrease in the inertiocapillary time scale along the jet, caused by the thinning effect of the effective gravity (i.e., the longitudinal projections of the centrifugal and gravity forces). We also derived self-similar solutions for convective linear stability, providing a straightforward approximation for the jet breakup length. Despite the simplified nature of our approach and the necessary assumptions, these are valid and applicable in various processes, such as the prilling of fertilizers, where the working liquids, like molten urea, exhibit low viscosities.

- **Can thermal excitation be used to force breakup of a straight jet? What is the effect of the frequency and amplitude of thermal excitation of the jet on breakup?**

Controlling the jet breakup and droplet formation requires a well-defined perturbation on the jet conditions to invoke a Rayleigh-Plateau instability mode. Creating this perturbation is usually done either by piezo actuation systems where the inlet boundary conditions are perturbed with a certain frequency and amplitude, or by acoustic means where the entire jet is perturbed and the fastest growing Rayleigh-Plateau instability is invoked. In Chapter 3, we used numerical simulations to illustrate that adjusting the inlet temperature of straight jets serves as a means to regulate the breakup and formation of droplets. The modulation of temperature induces local perturbations in both thermally-induced capillary and Marangoni stresses. To gain a deeper understanding, we propose breaking down the surface tension forces into contributions from curvature-gradient and surface tension gradient forces. The ratio of the surface-tension-gradient force to the imposed random perturbation force at the nozzle exit is quantified by the thermal modulation strength number, denoted as $\mathcal{M}$. This number is influenced by the amplitude and frequency of thermal modulation, the sensitivity of surface tension to temperature variations, the Weber number, and the noise amplitude in the nozzle exit velocity. Higher values of the thermal modulation strength number enhance control, resulting in shorter intact lengths and more uniform droplet streams. As the modulation strength increases, the role of thermal modulation shifts from being solely a trigger for the exponential growth of curvature-gradient forces to a scenario where both curvature-gradient and surface tension gradient forces dominate until pinch-off. Consequently, the thermal modulation strength number proves to be a valuable criterion for designing thermal modulation to achieve controlled jet breakup, especially in determining the minimum required thermal modulation strength for generating a uniform droplet stream. Future extensions of this work could include studying thermal modulation in the presence of non-negligible axial heat conduction and/or cooling to the ambient environment.

- **What physical mechanism is responsible for rapid jet contraction of a jet at nozzle exit? More specifically, what is the influence of viscous and capillary (surface tension) effects on jet contraction and on the transition from jet expansion at low jet Reynolds number to jet contraction at higher Reynolds numbers?** These questions have been addressed in Chapter 4, where we presented simulation results for a laminar, axisymmetric jet of a Newtonian liquid issued from a long circular nozzle into a gaseous environment. We showed that the jet contracts for Reynolds numbers, $Re = \frac{\rho U_b 2R}{\eta}$, smaller than about 14.4, while the jet expands beyond this threshold value. The numerical results are in good agreement with experimental data from Goren & Wronski [1]. A polynomial equation was derived for the jet contraction ratio, $\chi = R_\infty / R$, with coefficients that could be evaluated from the simulation data. The solution for χ obtained from this equation is in good agreement with the experimental data. From this equation it was also found that surface tension effects on the jet contraction ratio cannot be neglected for $Re \lesssim 10$ in the experiments of Goren & Wronski [1]. For small Reynolds number, we found that the expansion of the jet is caused by a compressional radial viscous stress at the jet interface immediately downstream of the nozzle exit. For large Reynolds

number, when viscous and surface tension effects are negligible, our polynomial equation recovers the classical result of Harmon [2] for the jet contraction ratio based on conservation of the integral mass and momentum fluxes along the jet.

- **How can the results obtained for a single spiralling jet be used to predict the prill size distribution in an industrial prilling process?**

  Finally in Chapter 5, we discussed the first steps towards using the studied modelling approach which is validated with lab scale experiments as a tool in an industrial scale prilling process. The main differences between a lab scale rotating orifice and a prilling bucket is highlighted and a case study with a typical prilling bucket is presented. One needs to pay special attention to the limitations of the approach for an industrial scale modelling of the process. One limitation is that the slender jet approach takes an "ideal case" as initial and boundary condition which is not the actual case when one considers one of the many spiralling jets emerging form the perforated bucket. The flow carries significant history from inside the bucket to the jet, which is not captured in the slender jet framework. Another limitation is the neglected jet-jet interactions with the slender jet approach on a single jet. These interactions can be aerodynamic in nature, where one jet may lead to wake region behind it, and the capillary instability of the succeeding jet may be influenced by the existence of this wake region.

What has been covered in this thesis is only a fraction of the open questions and unaddressed challenges in this problem. The prilling process is a coupled multi-scale and multiphysics problem and controlling it is a challenging exercise. So there is more to be done both from fundamental and applied research perspectives. From a fundamental point of view, the natural breakup of liquid jets still needs further research. Jet breakup is extremely sensitive to initial and boundary conditions (e.g. at the nozzle). The predictions of jet breakup length and size of the droplets rely on linear and nonlinear stability analyses where the base state is a stable cylindrical column and there is a perturbation of known frequency and amplitude. In most practical cases, however, the initial condition of the jet is not a liquid column and the liquid already carries disturbances from upstream the nozzle. In this thesis, these unknown effects are mimicked by adding white noise to the jet velocity - where the intensity of the noise is a free parameter and is tuned using experimental results. There is still a lack of a comprehensive theory to predict the jet breakup length and drop size distribution without having a known frequency and amplitude.

From applied research point of view, different perturbation mechanisms are remaining to be further explored, especially for large scale processes such as prilling. For a large scale process of jet breakup where the perturbing components are large and have high inertia, eliminating the necessity of large moving parts to actuate the jet breakup is an important and promising concept. In Chapter 3, thermal excitation for a non-isothermal jet is studied theoretically and numerically. In industrial processes, this can be achieved by Joule heating or lasers. Thus a natural follow up of this work is to design a proof-of-concept and study ways to make it a robust mechanism.

6

ACKNOWLEDGEMENTS

"When the Hurly-Burly's done
When the battle's lost and won"
Sitting down to write the acknowledgements is a good opportunity to reflect on the great journey of conducting PhD, which reminded me of the lines above from one of my favourite pieces of literature, Macbeth. Surely, any completed PhD is a battle won, but within that there are many small defeats and victories. And surely, I had my fair share of the Hurly-Burly as well. The entire COVID-19 pandemic took place within my PhD journey, which had benefited me to some extend where I could focus on my work but let to times where it made me (along with everybody around) feel lost. I would at this point like to thank the P&E department for giving me a 3 month extension for my PhD to help deal with the adverse impact of the pandemic on the project.

I would like to express my deepest gratitudes to my supervisors **Wim-Paul Breugem** and **Burak Eral**. They gave me the opportunity and space to own the project and run it, while always being there to steer me in the right direction when I lose focus of the end goal. I learned so much from both. I learned how to approach a problem meticulously from first principles, and use proper mathematical tools from Wim-Paul, and I learned how to take one step back to see the big picture when necessary and allocate the focus on the right things from Burak. I feel lucky to work with Wim-Paul and Burak – and without your guidance it would be impossible to develop this research.

My dear collaborators (and now colleagues) from Kreber, **Toon** and **Marco**. It was always inspiring to have an industry perspective on my work and our discussions always sparked new ideas in me. I know that we will carry this work far beyond this thesis together, along with trips to De Kuip 'hand in hand, kameraden'.

Caroline, as much as your administrative support – I will never forget your genuine friendship. You have always been an amazing presence, and I will miss stopping by your office to exchange life experiences (and keeping you from your work).

I also had the opportunity to supervise very bright and enthusiastic master students. **Suriya**, you were the first Master student in my project and we started working together in my 4th month where I was barely getting a grip of everything. I really appreciate your enthusiasm, skills, hard-work and contribution to the project. We badged it with a great publication together too, and I wish you the very best in your bright career. **Emma, Mels and Sander**, I really enjoyed working with all of you individually and I thank you for your enthusiasm and for the fruitful discussions we had.

During my time of PhD, I developed relationships with some people that go way beyond being lab mates and become long-lasting friendships. **Tariq, Guillermo, Florian, Udhav** and **Bob** – we have shared so many memories climbing, chilling together talking everything about everything. Your presence made the lockdown days way more enjoyable. I am so grateful to have you as my friends and I am always inspired by your per-

spectives. **Wouter**, we started our PhD journey around the same time and we bonded naturally with all the conference and school trips being roommates. **Ankur** and **Wout**, you were my first office mates and I am very thankful to your positive, welcoming presence and support.

Edwin, Jasper, Jan, Koen, John, Lina, Jesse, Lyke, Junaid, Haoyu, Luuk, Gem, Mike, Soren, Willian, Amitosh, Arnoud, Ellert, Daniel, Jerry and **Christian** – I will miss the long (sometimes too long) conversations around the coffee table every day, covering everything from science, politics to Dutch TV and F1. Always a broadening experience to exchange views with all the unique individuals that you are.

I would like to forward special thanks to some of the professors in and outside of our department, who gave me new perspectives on my work and made this thesis more complete. **Lorenzo, Mathieu, Willem** – thank you for your interest in my work and giving me inspiration. Also special thanks to **Bavand Keshavarz** – you have always been very helpful, and I learned so much from your knowledge and experience in rheology.

My friends outside the lab, who have made my experience in Netherlands so beautiful. **Casper**, we had, and we will share many deep conversations along with many parties together. Burgwal has always been a great place to meet great people and it was the place my first live gig as DJ too! You are a lifelong friend and here is to many more experiences together. Likewise; **Tomas, Hannah, Nicco, Fernando, Simone, Weronika, Elise, Satyajith and Pierre-Yves**. We shared not only climbing but many other good memories and I am excited for the new ones to come.

And finally, **Clémence**, or better known as Clem. Our paths crossed in the final stint of this PhD journey - and so wonderful that it did! I cannot end this dissertation without acknowledging your beautiful presence and positivity in my life. You are an amazing partner, friend and human being - someone I deeply love, respect and look up to. End of this PhD is an end of a chapter in my life, and I am looking forward to the new ones with you in it.

Yavuz Emre Kamis
Rotterdam, February 2025

CURRICULUM VITÆ

Yavuz Emre KAMIS

26-07-1991   Born in Istanbul, Turkey.

2005–2010   High School
American Robert College, Istanbul, Turkey

2010–2014   Bachelor in Mechanical Engineering
Boğaziçi University, Istanbul, Turkey

2014–2018   Master in Mechanical Engineering
Boğaziçi University, Istanbul, Turkey
Thesis: Stability of the non-isothermal Taylor-Couette flow of
a ferrofluid under external magnetic field
Promotor: Prof. dr. K. Atalık

2019–2023   Ph.D. researcher
Delft University of Technology, Delft, The Netherlands
Thesis: Breakup and droplet fromation of thin liquid jets in
prilling applications
Promotors: Dr. Ir. W. P. Breugem & Dr. Ir. H. B. Eral

2023–Present RD&I Engineer
Kreber BV, Vlaardingen, The Netherlands

Scientific Contributions

Publications

1. Y. E. Kamis, H. B. Eral, and W.-P. Breugem. "Active control of jet breakup and droplet formation using temperature modulation". In: *Physical Review Fluids* 6.10 (2021), p. 103903

2. Y. E. Kamis, S. Prakash, W.-P. Breugem, and H. B. Eral. "Controlling the breakup of spiralling jets: results from experiments, nonlinear simulations and linear stability analysis". In: *Journal of Fluid Mechanics* 956 (2023), A24

3. Y. E. Kamış and K. Atalık. "Thermomagnetic effects on the stability of Taylor-Couette flow of a ferrofluid in the presence of azimuthal magnetic field". In: *Journal of Magnetism and Magnetic Materials* 454 (2018), pp. 196–206 *(not related to this thesis)*

Oral presentations at conferences

1. 14th European Congress of Chemical Engineering, 17-21 September 2023, Berlin

2. J.M. Burgers' Symposium, 31 May-1 June 2023, Lunteren

3. APS Division of Fluid Dynamics, 20-22 November 2022, Indianapolis, IN

4. Annual European Rheology Conference, 13-14 April 2021 (online)